



INTERREG-V OCEAN INDIEN 2014-2020

Projet de Recherche

RENOVRISK-CYCLONES ET CHANGEMENT CLIMATIQUE

Axe-1 OT-1 OS-01a - Action I-3 TF



Livrable 11

Rapport de synthèse sur l'analyse statistique de la modification du comportement des cyclones (trajectoire, intensité, structure) et des anomalies de précipitations à l'échelle régionale pour différents scénarii du GIEC

Olivier BOUSQUET, UMR 8105 LACy

Mars 2021

Ce livrable est associé à la sous-action 3.1 intitulée :

Évolution de l'activité cyclonique à l'échelle régionale

L'impact du changement climatique sur la modification du comportement des cyclones (trajectoire, intensité, structure) a été étudié au moyen de simulations numériques réalisées avec le modèle ARPEGE-Climat et certains modèles mis en œuvre lors des exercices d'intercomparaison CMIP5 et CMIP6 du GIEC.

Ces travaux ont fait l'objet d'une publication dédiée dans la revue *Journal of Climate* et d'une autre dans la revue *Atmosphère* (pages 19-23) qui sont reproduites ci-après.

Projected Changes in the Southern Indian Ocean Cyclone Activity Assessed from High-Resolution Experiments and CMIP5 Models

JULIEN CATTIAUX AND FABRICE CHAUVIN

Centre National de Recherches Météorologiques, Université de Toulouse, CNRS, Météo-France, Toulouse, France

OLIVIER BOUSQUET, SYLVIE MALARDEL, AND CHIA-LUN TSAI

Laboratoire de l'Atmosphère et des Cyclones, Université de la Réunion, CNRS, Météo-France, Saint-Denis, France

(Manuscript received 2 August 2019, in final form 7 March 2020)

ABSTRACT

The evolution of tropical cyclone activity under climate change remains a crucial scientific issue. Physical theory of cyclogenesis is limited, observational datasets suffer from heterogeneities in space and time, and state-of-the-art climate models used for future projections are still too coarse (~100 km of resolution) to simulate realistic systems. Two approaches can nevertheless be considered: 1) perform dedicated high-resolution (typically <50 km) experiments in which tropical cyclones can be tracked and 2) assess cyclone activity from existing low-resolution multimodel climate projections using large-scale indices as proxies. Here we explore these two approaches with a particular focus on the southern Indian Ocean. We first compute high-resolution experiments using the rotated-stretched configuration of our climate model (CNRM-CM6-1), which is able to simulate realistic tropical cyclones. In a 2-K warmer world, the model projects a 20% decrease in the frequency of tropical cyclones, together with an increase in their maximum lifetime intensity, a slight poleward shift of their trajectories, and a substantial delay (about 1 month) in the cyclone season onset. Large-scale indices applied to these high-resolution experiments fail to capture the overall decrease in cyclone frequency, but are able to partially represent projected changes in the spatiotemporal distribution of cyclone activity. Last, we apply large-scale indices to multimodel CMIP5 projections and find that the seasonal redistribution of cyclone activity is consistent across models.

1. Introduction

Understanding how climate change may influence tropical cyclone (TC) activity remains a challenging scientific issue (Knutson et al. 2010; Walsh et al. 2016). As TCs cause local devastating impacts and play a crucial role in maintaining regional water resources, this question also receives particular public attention.

Detecting potential trends in observational data is limited by the quality of historical records and the difficulty to disentangle the climate change signal from the noise of internal variability. A few studies have analyzed the International Best Track Archive for Climate Stewardship (IBTrACS) database, which compiles the best track datasets from diverse centers (Knapp et al. 2010). Various trends have been reported, such as an increase and a poleward shift in the TC lifetime

maximum intensity (Kossin et al. 2013; Holland and Bruyère 2014) or a slowdown of the translation speed (Kossin 2018), but it remains unclear whether these trends result from data heterogeneities (e.g., introduction of new satellites), natural variability, or anthropogenic forcings. Therefore, so far, most assessments regarding the evolution of TCs in a warmer world have been made from theoretical and/or modeling studies.

There is a theoretical expectation that a warmer climate would undergo stronger TCs, in line with higher sea surface temperatures (SST) and increased potential intensity (Emanuel 1988). However, no such robust conclusion exists for changes in TC frequency due to the lack of a generally accepted theory for cyclogenesis, even if progress has been made on identifying the environmental conditions favoring cyclone activity (e.g., Held and Zhao 2011; Peng et al. 2012; Sugi et al. 2012).

Modeling studies addressing the evolution of TCs under climate change face an implacable issue: grid resolution must be high enough to simulate realistic

Corresponding author: Julien Cattiaux, julien.cattiaux@meteo.fr

DOI: 10.1175/JCLI-D-19-0591.1

© 2020 American Meteorological Society. For information regarding reuse of this content and general copyright information, consult the [AMS Copyright Policy](#) (www.ametsoc.org/PUBSReuseLicenses).

TCs and experiments must be long enough—or enroll enough ensemble members—to isolate climate change from natural variability. The current generation of global models used for future climate projections—i.e., participants of the phase 5 of the Coupled Model Intercomparison Project (CMIP5)—have a horizontal grid spacing of about 100 km or greater (Taylor et al. 2011), which is too coarse to simulate realistic TCs (Camargo 2013); interestingly, the upcoming generation (CMIP6) will include a few models with higher resolutions (typically 50 km or higher). So far two approaches have thus been traditionally considered for studying TCs: (i) perform additional dedicated experiments at a higher resolution, or (ii) use the existing multimodel low-resolution climate projections to assess how large-scale environmental conditions favorable to cyclone activity may evolve in a warmer climate.

The first approach has been undertaken by a growing, but still limited, number of modeling centers that can afford the computer cost of high-resolution climate projections. Most of the performed experiments project a future reduction in the overall frequency of TCs, but an increase in the frequency of the strongest TCs (Walsh et al. 2016, and references therein). Also commonly reported are projected increases in associated phenomena, such as rainfall amounts and storm surges (Knutson et al. 2015; Woodruff et al. 2013).

The second approach consists of determining statistical relationships between cyclone activity and large-scale environmental factors, including dynamical (e.g., vertical and horizontal wind shear, low-tropospheric vorticity) and thermodynamical (e.g., midtropospheric humidity, sea surface temperature) variables. Combinations of these variables allow us to build cyclogenesis indices (CGIs), that have been shown to represent both the seasonal and geographical distribution of cyclone activity fairly well (Menkes et al. 2012). (Previous authors have used the abbreviation “GPIs” as the generic term for these indices, but since “GPI” is also an abbreviation used for one specific index used in this paper, here we use “CGIs.”) Using CGIs to quantify potential changes in the cyclone activity is, however, questionable, as it assumes that statistical relationships established for present-day climatological features remain valid in a climate change context. In particular, it has been shown that CGIs fail to capture the decrease in TC frequency when applied to high-resolution climate projections (Camargo et al. 2014; Wehner et al. 2015; Chauvin et al. 2020), which may explain why attempts to apply CGIs to CMIP5 future projections have mostly remained inconclusive so far (Camargo 2013). However, the

ability of CGIs to capture other potential changes in the cyclone activity (e.g., changes in the spatiotemporal distribution) has not been documented so far. In addition, since CGIs can be broken down into dynamical and thermal components, they can provide useful insights for the physical understanding of the projected changes in TC tracks.

Here we apply and compare both high-resolution and CGIs approaches to assess projected changes in cyclone activity and explore whether the two approaches can be reconciled on some aspects. We use the same methodology as in Chauvin et al. (2020) but we focus over the SIO basin, which has been seldom studied so far. Among the eight IBTrACS basins, it ranks third in terms of overall number of reported TCs (after the western and eastern Pacific basins). Even if less highly populated regions are exposed to TC hazards than in other basins, SIO TCs can still have dramatic impacts in Western Australia and southeastern Africa, including Madagascar and the Mascarene Islands (La Réunion, Mauritius, and Rodrigues), as recently illustrated by the devastating cyclone Idai.¹ In the western part of the SIO, the death toll associated with TCs averages to 20 fatalities per year over the last 19 years with 9 seasons above 100 fatalities according to the European Commission Joint Research Centre.² Long-term climate trend analysis in the SIO basin is particularly challenging due to the introduction of the *Meteosat-5* geostationary satellite into the region in 1998, which causes a temporal heterogeneity in observational and reanalysis products (Kuleshov et al. 2010; Kossin et al. 2013). Evidences for an observed increase in the number of severe TC days have nevertheless been reported in the western part of the SIO (Kuleshov et al. 2010; Malan et al. 2013). High-resolution climate projections suggest that SIO TCs follow the global behavior: a decrease in the overall frequency and an increase in the intensity (e.g., Murakami et al. 2012; Walsh et al. 2016).

The paper is structured as follows. Observations, reanalyses, high-resolution experiments, and CMIP5 models used in this study are presented in section 2. Methodologies including the tracking algorithm applied to high-resolution data and the cyclogenesis indices applied to lower-resolution data are detailed in section 3. Section 4 contains our main findings while discussion and conclusions are provided in sections 5 and 6.

¹ <https://public.wmo.int/en/media/news/tropical-cyclone-idai-hits-mozambique>.

² Emergency Reporting 23: <http://www.gdacs.org/Public/download.aspx?type=DC&id=161>.

TABLE 1. Observations, reanalyses, and CNRM-CM experiments used in this study. Time periods correspond to Southern Hemisphere convention for cyclone seasons (i.e., 1980 is July 1979–June 1980).

Abbreviation	Name	Details	Resolution (km)	Time period	TC tracks
IBTr	IBTrACS	TC track observations	—	1980–2016	×
ERA1	ERA-Interim	Reanalysis	80	1980–2016	
ERA5	ERA-5	Reanalysis	30	1980–2016	×
T127	CNRM-CM5	Historical simulation	155	1976–2005	
T359	CNRM-CM6-HR	AMIP simulation	55	1980–2010	×
SIO-P	CNRM-CM6-HR r.-s.	Experiment forced by historical SST	10–50	1971–2014	×
SIO-F	CNRM-CM6-HR r.-s.	Experiment forced by RCP8.5 SST	10–50	2051–94	×

2. Data

a. Observations and reanalyses

Observations and reanalyses used in this study are summarized in Table 1. Observational TC data are taken from the IBTrACS, version 4, dataset released in April 2019 that provides best track characteristics (e.g., position, sea level pressure, maximum sustained winds) on a 3-hourly basis (<https://www.ncdc.noaa.gov/ibtracs/>, Knapp et al. 2010). For consistency with model and reanalysis data used in this study, we restrict IBTrACS data to the period July 1979–June 2016 (i.e., cyclone seasons 1980–2016) and the hours 0000, 0600, 1200, and 1800 UTC. We only use information provided by the World Meteorological Organization (WMO) Regional Specialized Meteorological Centres (RSMCs): Météo-France La Réunion and the Australian Bureau of Meteorology (BoM) for the SIO basin. We only consider systems that are indicated as “TS” (tropical storms) in the metadata and that reach the official *moderate tropical storm* (category 1) stage according to Météo-France (BoM) classifications (i.e., 10-min sustained winds above 18 m s^{-1}) at least once in their lifetime. (Note that we use the terminology of the local RSMCs in this paper, not the Saffir–Simpson scale.)

ERA-5 data (30-km resolution, Hersbach et al. 2018) are used for both TC tracking and computing CGIs. ERA-Interim data (80-km resolution, Dee et al. 2011) are also used for computing CGIs, which allows for a fair comparison with CMIP5 models as they do not simulate realistic TCs (contrarily to ERA-5). Both datasets are downloaded from the European Centre for Medium-Range Weather Forecasts (<https://www.ecmwf.int/en/forecasts/datasets/browse-reanalysis-datasets>), on a regular $0.5^\circ \times 0.5^\circ$ longitude–latitude grid and at a 6-hourly frequency over the period July 1979–June 2016 (i.e., cyclone seasons 1980–2016).

b. High-resolution experiments

We use the same experimental setup as in Chauvin et al. (2020), which consists in performing atmosphere-only

present-day and future experiments with the Centre National de Recherches Météorologiques Coupled Global Climate Model (CNRM-CM) in its rotated-stretched configuration. The atmospheric component of CNRM-CM (ARPEGE) has indeed the particularity to enable a deformation of its horizontal grid: the pole can be placed over a location of interest (here, the SIO), and a stretching factor can be applied to progressively increase (decrease) the resolution around the pole (the antipode). The advantage of this configuration is that it provides high-resolution simulations over the area of interest, while preserving the consistency of the large-scale dynamics between global and regional scales. This technique has been extensively validated as it is routinely utilized by Météo-France for operational numerical weather prediction over Europe and has also been used in numerous studies of TCs over the North Atlantic basin (e.g., Chauvin et al. 2006; Daloz et al. 2012; Chauvin et al. 2020).

In the present study, the stretching is applied to a T359 grid (720×360 points), the pole is located at 12.5°S , 55°E , and the stretching factor is 3.5, resulting in a 14–50-km effective resolution within the SIO domain (defined as $0^\circ\text{--}30^\circ\text{S}$, $30^\circ\text{--}120^\circ\text{E}$; see Fig. 1a). The choice of the exact grid pole location was made in order to have the highest-resolution increase in the area under the responsibility of the Météo-France RSMC on La Réunion Island. The model is run with a 15-min time step. We use the same version of ARPEGE as in Chauvin et al. (2020) (i.e., a version close to the one participating to CMIP6 through CNRM-CM6-1 and CNRM-ESM2 models). A comprehensive description of this version, including details on convection, microphysics, and turbulence parameterizations, can be found in Voldoire et al. (2019), together with an evaluation of the CNRM-CM6-1 model.

Similarly to Chauvin et al. (2020), two experiments are conducted with the rotated-stretched configuration: a present-day simulation over the period 1971–2014 (named SIO-P), using historical SST and radiative forcings, and a future simulation over the period 2051–94

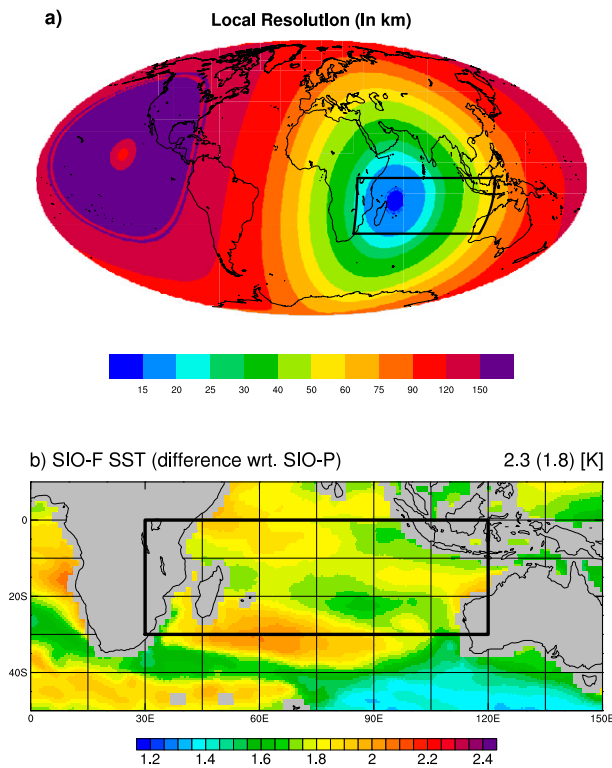


FIG. 1. (a) Effective grid resolution (km) of the rotated–stretched experiments. (b) Mean difference between prescribed SST (K) of SIO-F and SIO-P experiments.

(named SIO-F), using future SST and radiative forcings corresponding to the 8.5 W m^{-2} radiative concentration pathway (RCP8.5). Prescribed SST are taken from a member of CNRM-CM5 historical 1 RCP8.5 simulations (namely, the run r1i1p1; Voldoire et al. 2013), and are bias corrected over the present-day period with respect to the HadISST dataset (Rayner et al. 2003). Further methodological details, including the treatment of sea ice,

are provided in Chauvin et al. (2020). The time-averaged SST difference between the two experiments is a generalized warming ranging from 1.6 to 2 K over the SIO domain with a field average of 1.8 K (Fig. 1b); CNRM-CM5 is close to the CMIP5 multimodel mean on this aspect (not shown). To assess the potential benefits of the rotated–stretched configuration in simulating cyclones, a third experiment with a uniform T359 grid (denoted T359) is conducted over 1980–2010 using prescribed SST from HadISST.

c. CMIP5 simulations

We use monthly outputs of atmospheric temperature (ta), wind (ua, va), specific humidity (hus), convective precipitation (prc), sea level pressure (psl), and sea surface temperature (ts) from the historical + RCP8.5 simulations of 14 CMIP5 models (Table 2). This ensemble includes the CNRM-CM5 simulation from which SST are taken to perform the high-resolution experiments, which will be denoted T127 in the following. All fields are interpolated from the native model grid onto a common $2.5^\circ \times 2.5^\circ$ longitude–latitude grid prior to any diagnostic computation. This is also the case for ERA-5 and ERA-Interim data when they are compared with CMIP5 data.

3. Methods

a. Tracking algorithm

As in Daloz et al. (2012) and Chauvin et al. (2020), we use the algorithm introduced and detailed in Chauvin et al. (2006) to track TCs in ERA-5 and SIO-P, SIO-F, and T359 experiments. The tracker is applied to 6-hourly outputs, and in this paper all the data are first interpolated onto a common $0.5^\circ \times 0.5^\circ$ longitude–latitude

TABLE 2. CMIP5 models used in this study.

Abbreviation	Name	Country	Lon \times lat	Resolution (km)
BCC	BCC-CSM1.1	China	$2.8^\circ \times 2.8^\circ$	310
CCCMA	CanESM2	Canada	$2.8^\circ \times 2.8^\circ$	310
CNRM	CNRM-CM5	France	$1.4^\circ \times 1.4^\circ$	155
CSIRO	CSIRO-Mk3.6.0	Australia	$1.9^\circ \times 1.9^\circ$	210
GFDL	GFDL-ESM2M	United States	$2.0^\circ \times 2.5^\circ$	250
GISS	GISS-E2-R	United States	$2.0^\circ \times 2.5^\circ$	250
INM	INM-CM4	Russia	$1.5^\circ \times 2.0^\circ$	195
IPSL	IPSL-CM5A-LR	France	$1.9^\circ \times 3.8^\circ$	300
MIROC	MIROC-ESM	Japan	$2.8^\circ \times 2.8^\circ$	310
MOHC	HadGEM2-ES	United Kingdom	$1.3^\circ \times 1.9^\circ$	180
MPIM	MPI-ESM-LR	Germany	$1.9^\circ \times 1.9^\circ$	210
MRI	MRI-CGCM3	China	$1.1^\circ \times 1.1^\circ$	120
NCAR	CCSM4	United States	$0.9^\circ \times 1.3^\circ$	120
NCC	NorESM1	Norway	$1.1^\circ \times 1.1^\circ$	120

grid (i.e., the effective grid of the T359 experiment and the resolution chosen for the download of ERA-5 data) in order to allow for a fair comparison. The tracking algorithm involves three steps:

- 1) At each time step, grid points potentially concerned by a TC are identified, based on the main criteria that depict TCs: sea level pressure is a local minimum (low pressure system), 850-hPa vorticity exceeds a threshold (strong vortex), 10-m wind speed exceeds a threshold (strong winds), mean 700–300-hPa temperature local anomaly exceeds a threshold (warm core), tangential wind speed is higher at 850 hPa than at 300 hPa (stronger winds at low levels due to the thermal wind relationship), temperature local anomaly is higher at 300 hPa than at 850 hPa (warmer core at high levels). (Thresholds are discussed below.) Note that there is no latitude criterion, so that the detection can potentially occur outside the tropics.
- 2) TC points identified in step 1 are connected across consecutive time steps to build TC tracks. The association procedure is described in detail in Chauvin et al. (2006).
- 3) Tracks are completed before and after the TC stage in order to include cyclogenesis and cyclolysis. This is done by relaxing all criteria except vorticity and rerunning the algorithm backward (forward) from the first (last) point of the previously identified TC track. This step also ensures that a system reaching the TC stage twice (or more) in its lifetime is counted as a unique system.

The algorithm is highly sensitive to the thresholds used in step 1 that primarily depend on the data resolution. Here, the thresholds have been calibrated by repeating the tracking procedure on ERA-5 over 2011–16 with various combinations of thresholds and comparing the resulting tracks to IBTrACS. The retained values are $20 \times 10^{-5} \text{ s}^{-1}$ for vorticity, 13 m s^{-1} for wind speed, and 1 K for local temperature anomaly. With these values, the algorithm detects most of IBTrACS trajectories in ERA-5, with a limited number of false or missed tracks (see example of cyclone season 2015 in Fig. 2 and further details in section 4). Note that a perfect correspondence between IBTrACS and ERA5 tracks was not expected due to (i) IBTrACS specificities, (ii) potential model errors, and (iii) potential impacts of data assimilation on TCs.

We distinguish three stages in the tracks resulting from the algorithm: the development stage [from the system initiation (or cyclogenesis) to its intensification into a TC], the TC stage (encompassing all TC points with possible temporary interruptions), and the cyclolysis stage (from the last TC point to the end of the track). For consistency, we also distinguish these three stages in

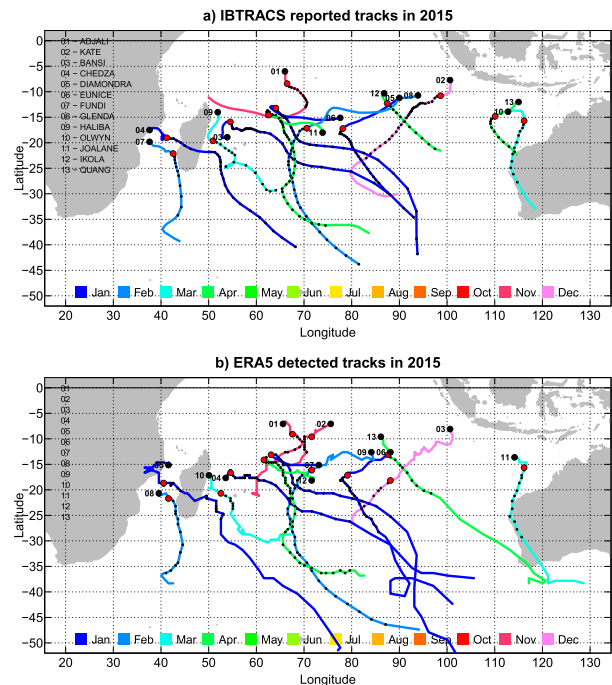


FIG. 2. (a) TC tracks reported in IBTrACS for the 2015 season. (b) TC tracks resulting from the tracking algorithm applied to ERA5 for the 2015 season. Dots along trajectories indicate TC points, with thick black dots for the first point of the system (genesis point) and thick red dots for the first point of the TC stage (intensification point). Track colors indicate the month of the track starting point (genesis).

IBTrACS, but on the basis of the 18 m s^{-1} wind speed threshold: development stage from the track start to the first exceedance, then TC stage until the last exceedance, then cyclolysis stage.

b. Cyclogenesis indices (CGIs)

The link between cyclone activity and large-scale environmental conditions is assessed using CGIs from the existing literature. We use the three indices evaluated on seasonal and interannual time scales by Menkes et al. (2012), and used separately by Royer and Chauvin (2009), Camargo (2013), and Chauvin et al. (2020) in a climate change perspective:

- the CYGP index introduced by Royer et al. (1998), after Gray (1975);
- the GPI index introduced by Emanuel and Nolan (2004);
- the TCS index introduced by Tippet et al. (2011) (hereafter referred as TIPP in order to avoid confusion with the TCs acronym used for “tropical cyclones”).

All indices are computed at the gridpoint scale and on a monthly basis (i.e., calculated with monthly mean climate data). They are constructed as multiplicative functions of dynamical and thermal variables that result

from empirical fits between observed cyclone activity and reanalyzed large-scale variables. Dynamical variables are the same for the three indices used in this paper (low-level vorticity and vertical wind shear) while thermal variables differ. More precisely, the indices are as follows:

$$\text{CYGP} = \beta_{\text{CYGP}} \times \underbrace{|f| \left(\frac{\zeta_r}{|f|} + 5 \right) (V_{\text{shear}} + 3)^{-1}}_{\text{Dynamical}} \times \underbrace{\max(P_c^* - 3, 0)}_{\text{Thermal}}, \quad (1)$$

$$\text{GPI} = \beta_{\text{GPI}} \times \underbrace{|10^5 \zeta|^3 (1 + 0.1V_{\text{shear}})^{-2}}_{\text{Dynamical}} \times \underbrace{\left(\frac{H}{50} \right)^3 \left(\frac{V_{\text{pot}}}{70} \right)^3}_{\text{Thermal}}, \quad (2)$$

$$\text{TIPP} = \beta_{\text{TIPP}} \times \underbrace{\cos(\varphi) \exp(1.03\zeta - 0.15V_{\text{shear}})}_{\text{Dynamical}} \times \underbrace{\exp(0.05H + 0.56\text{SST}_{\text{loc}})}_{\text{Thermal}}, \quad (3)$$

where f is the Coriolis parameter, φ is the latitude, ζ (ζ_r) is the absolute (relative) vorticity at 850 hPa, $V_{\text{shear}} = \Delta V/\Delta p$ is the vertical wind shear between 850 and 200 hPa, P_c^* is the convective precipitation, H is the relative humidity at 600 hPa, $\text{SST}_{\text{loc}} = \text{SST} - \text{SST}^{(20\text{S}-20\text{N})}$ is the local SST anomaly relative to the tropics (20°S–20°N), and V_{pot} is the TC potential intensity introduced by Emanuel (1988) that we calculate using the `pmin_2013.f` routine distributed by K. Emanuel.³ For the three indices, the β coefficient is a scaling factor that allows to interpret global maps of CGIs as densities of TCs; here we systematically tune these scaling factors so that the global sum of CGIs equals 84 (TCs per year over the globe) over the present-day period, and we keep the same β for computing indices over future periods. More details about the computation of these three indices can be found in the appendix of Menkes et al. (2012).

It is important to note that in this paper, we use the exact same equations for all reanalysis or model data on which we compute CGIs. In particular the numerical constants that are present in the above equations are the ones used by Menkes et al. (2012), and they correspond to the ones originally introduced by the respective authors. Camargo et al. (2014) suggest that CGIs perform better in capturing climate-related changes in cyclone

activity when they are refitted for the model of interest (including the selection of predictors). Here we consider that such a model-dependent computation of CGIs is outside the scope of our study, and that using the exact same definition for CGIs allows for a fair comparison between models. Last, for the sake of simplicity, results are mainly shown for the average of the three indices (hereafter the aggregate CGI), and behaviors of individual indices are only mentioned in the text when they substantially differ from the mean. Considering the average of CGIs also tends to emphasize signals that are common—thus robust—across individual indices.

As CGIs are written as multiplicative functions, differences between time averages over two periods of time (typically present-day vs future) can be broken down into individual contributions of dynamical versus thermal components. Indeed, for each calendar month, if x_i (y_i) denotes the dynamical (thermal) component of the CGI for year i , and x'_i and y'_i denotes their anomalies relative to their time averages \bar{x} and \bar{y} , the time-averaged CGI over either the present-day (P) or the future (F) period is

$$\overline{\text{CGI}} = \overline{x_i y_i} = (\overline{x + x'_i})(\overline{y + y'_i}) = \bar{x} \bar{y} + \overline{x'_i y'_i}. \quad (4)$$

Thus, the $F - P$ difference (denoted Δ) in time-averaged CGI is

$$\Delta \overline{\text{CGI}} = \overline{\text{CGI}}^F - \overline{\text{CGI}}^P = \overline{x^F y^F} - \overline{x^P y^P} + \underbrace{\overline{x'_i y'_i{}^F} - \overline{x'_i y'_i{}^P}}_{\varepsilon}, \quad (5)$$

with ε the residual term resulting from dependencies between monthly anomalies of x_i and y_i . Finally, since $\overline{x^F} = \bar{x}^P + \Delta \bar{x}$ and $\overline{y^F} = \bar{y}^P + \Delta \bar{y}$, one can write

$$\Delta \overline{\text{CGI}} = \underbrace{\overline{y^P \Delta x}}_{\text{Dynamical}} + \underbrace{\overline{x^P \Delta y}}_{\text{Thermal}} + \underbrace{\Delta \bar{x} \Delta \bar{y} + \varepsilon}_{\text{Residual}}, \quad (6)$$

where $\overline{y^P \Delta x}$ is the contribution of dynamical changes only, and $\overline{x^P \Delta y}$ is the contribution of thermal changes only. In the following, the last two terms $\Delta \bar{x} \Delta \bar{y}$ and ε are grouped into a single residual term, which is systematically shown in the figures but not commented in the text. The decomposition is performed for each calendar month separately and then averaged over the season or the year.

4. Results

a. Analysis of high-resolution experiments

1) REALISM OF SIMULATED TCs

To assess the realism of TCs simulated by the different model configurations, we first analyze the statistical

³ <ftp://texmex.mit.edu/pub/emanuel/TCMAX/>.

distribution of the annual minimum of sea level pressure in the SIO basin (Fig. 3a). Observed values are taken from IBTrACS assuming that annual minima of sea level pressure systematically occur within TCs. Over 1980–2016 the median is found to be 915 hPa; this means that such a low pressure is reached by at least one system over the SIO basin every 2 years on average. ECMWF reanalyses are unable to simulate pressures lower than 950 hPa, although a notable improvement is seen in ERA-5 relative to ERA-Interim (likely due to the increase in resolution). Uniform CNRM-CM configurations (T127 and T359) also fail to simulate extremely low pressures, although one outlying system reaches 905 hPa in the T359 experiment. The CNRM-CM5 (CNRM-CM6-1) model nevertheless simulates lower pressures than ERA-Interim (ERA-5) while it has a slightly coarser resolution; one reason could be that in reanalyses, data assimilation tends to spatially smooth low pressure systems when centers of action are slightly shifted between assimilated observations and forecast background. The added value of the rotated-stretched configuration in the present-day climate (SIO-P) is evident from Fig. 3a: this experiment is able to simulate lower pressures than observed (e.g., below 900 hPa), even if the median of the annual minimum pressure distribution remains slightly higher than observed (~930 hPa).

Once the tracking is done, the realism of resulting TCs is evaluated from the statistical relationship between the minimum sea level pressure and the maximum wind speed along the track (Fig. 3b). Both variables are indeed strongly correlated, as evidenced in TC observations (IBTrACS) and shown by Atkinson and Holliday (1977). Such a relationship is well captured by present-day model experiments (T359, SIO-P), although the model exhibits stronger winds than IBTrACS for a given pressure especially in the rotated-stretched configuration. The uniform experiment (T359) nevertheless struggles to simulate strong TCs (only two systems with pressure below 930 hPa and wind speed above 50 m s^{-1}) while the rotated-stretched experiment (SIO-P) can generate stronger TCs than the most intense TC recorded in IBTrACS. This result was also found by Chauvin et al. (2020) over the North Atlantic basin. Despite its fine resolution, ERA-5 fails to reproduce the strength of observed TCs. Note that a fair comparison between winds of IBTrACS, ERA-5, and ARPEGE experiments is, however, difficult since one compares wind output at a given time step and grid point (model) with 10-min sustained winds at the local cyclone scale (IBTrACS).

Finally, a first evaluation of the projected changes in TC characteristics can be assessed from these diagnostics: here we find no clear difference in the pressure–wind relationship between the SIO-P and the SIO-F

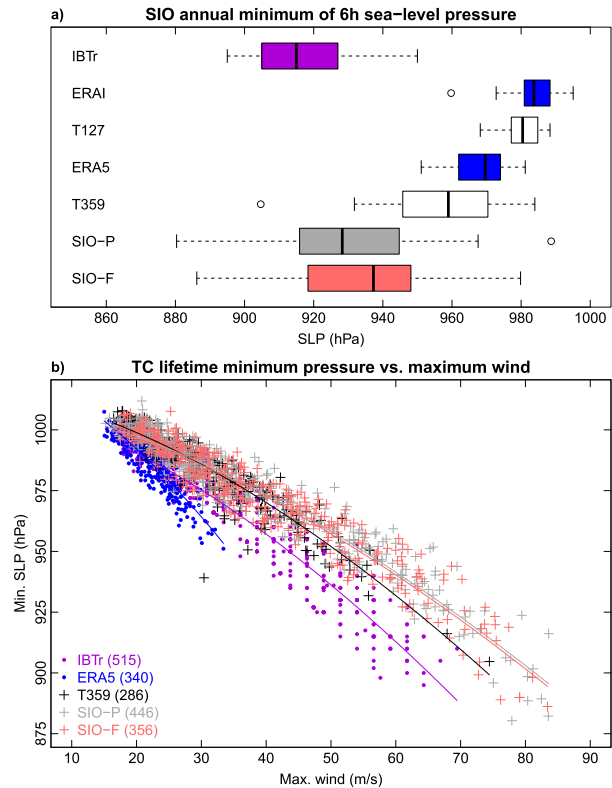


FIG. 3. (a) Distribution of the annual minimum of 6-h SLP (hPa) across the SIO domain (0° – 30° S, 30° – 120° E) for IBTrACS (1980–2016, violet), ERAI and ERA5 (1980–2016, blue), T127 (1976–2005) and T359 (1981–2010) uniform experiments (white), and SIO-P (1971–2014, gray) and SIO-F (2051–94, red) rotated-stretched experiments. In all boxplots used in this paper, the box represents the first and third quartiles, the band inside is the median, the whiskers expand to the largest values still within the 1.5 interquartile range from the box, and the small circles indicate outliers. (b) Lifetime minimum SLP (p) as function of lifetime maximum wind (V) for all TCs reported in IBTrACS and detected in ERA5, T359, SIO-P, and SIO-F [periods and colors are as in (a)]. Fits are added following Atkinson and Holliday (1977) (i.e., assuming $p = a + bV^{1/0.644}$ with a and b the coefficients to be fitted).

experiments (Fig. 3b), and although the SIO-F distribution of the annual minimum of sea level pressure seems slightly shifted toward higher pressures than SIO-P (Fig. 3a), the difference between the two samples is not statistically significant (p value of about 0.5). Changes in TC characteristics are thus more carefully scrutinized in the following.

2) ANALYSIS OF TC FREQUENCY

On average, 13.9 TCs per year are reported in the SIO domain by IBTrACS (Fig. 4a). As the average number of TC days per system is found to be 5.2 days, it leads to an annual number of TC days of 73 days (Fig. 4b). The tracking algorithm has been calibrated on ERA-5 over 2011–16 (section 3); on average over these years, it

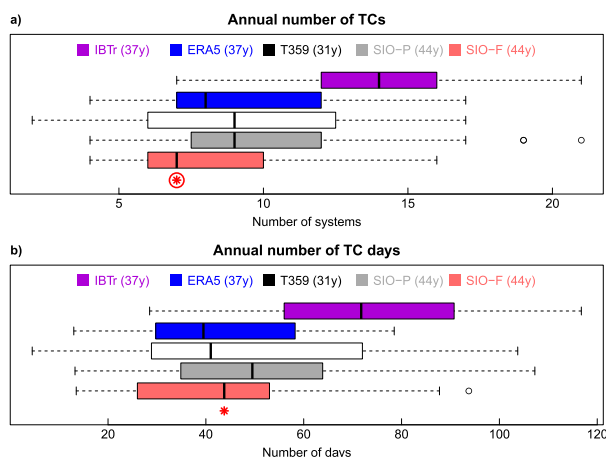


FIG. 4. (a) Distribution of the annual number of TCs in the SIO domain for IBTrACS (violet), ERA5 (blue), T359 (white), SIO-P (gray), and SIO-F (red). (b) As in (a), but for the annual number of TC days. Red (circled) asterisks indicate differences between SIO-P and SIO-F averages that are significant at the 90% (95%) level following a t test.

detects 11 TCs and 54 TC days per year (vs 12.5 TCs and 63 TC days per year in IBTrACS). Over the whole time period 1980–2016, the tracking algorithm applied to ERA-5 more substantially underestimates the observed number of both TCs (9 vs 13.9 yr^{-1}) and TC days (42 vs $73 \text{ TC days yr}^{-1}$). This inconsistency is the strongest at the beginning of the time period and progressively decreases with time (not shown), which questions the temporal homogeneity of IBTrACS and/or ERA-5 over the SIO. However, a more detailed evaluation is left for future studies.

T359 and SIO-P experiments simulate a similar amount of TCs (9.2 and 10.1 on average, distribution in Fig. 4a) and TC days (51 vs 52 on average, distribution in Fig. 4b). This suggests that the uniform 50-km resolution of the T359 experiment is potentially sufficient to generate a realistic number of TCs, albeit with weaker intensity than in the rotated-stretched configuration (see previous section and Fig. 3). The SIO-F experiment produces about 20% less TCs than the SIO-P experiment (8.1 yr^{-1} on average), which is qualitatively consistent with the broadly reported future decrease in TC frequency (e.g., Walsh et al. 2016) and quantitatively agrees with results of Murakami et al. (2012). This 20% decrease in the frequency is significant at the 95% level; as it is associated with a slight increase in TC duration (5.5 vs 5.1 TC days per system), the decrease in the annual number of TC days is less statistically significant (90% level, 44 vs 52 days). (This increase in TC duration is further detailed below with the TC intensity.)

In the SIO, TCs preferably develop close to the center of the basin (10° – 15°S , 60° – 80°E), the Mozambique

channel, and close to the Australian shore (Fig. 5a). This spatial pattern is well captured by ERA-5, confirming that the tracking algorithm applied to the reanalysis is able to detect part of the TCs reported in IBTrACS (Fig. 5b, spatial correlation of 0.90 with Fig. 5a). T359 and SIO-P experiments tend to simulate too little (much) TC intensification in the center (south) of the basin (Figs. 5c,d, spatial correlations of 0.62 and 0.51 with Fig. 5a). This might reflect a systematic bias of the CNRM-CM6-1 model since a similar behavior was reported by Chauvin et al. (2020) over the North Atlantic basin; future studies will investigate the origins of this geographical bias. The rotated-stretched configuration (SIO-P) results in an enhanced number of TCs in the SIO relative to the uniform configuration; symmetrically, less systems are simulated in other basins. A few systems have their intensification point outside the tropics (even south of 30°S) in the model; these can be either systems that have developed in the tropics and reached the TC stage after an extratropical transition, or systems that have developed outside the tropics but still meet the criteria to be detected as TC by the tracking algorithm. We have decided not to filter these systems out; in particular the use of a fixed latitude criterion would have been questionable in a climate change context. A small number of such extratropical systems is also detected in ERA-5 by the tracking algorithm.

In agreement with Fig. 4, SIO-F simulates globally fewer TCs than SIO-P, especially northeast of the Mascarene Islands (Fig. 5e). Although the signal is noisy due to the limited number of systems (446 in SIO-P vs 356 in SIO-F), more TC intensification is observed south of the Mozambique and west of Australia. Similar conclusions arise from analyzing densities of full TC tracks that are smoother due to the greater number of points included (Figs. 5f–j). In particular, the SIO-F versus SIO-P difference reveals a general northwest–southeast dipole (with the exception of the Mozambique channel), consistent with a poleward shift of TC tracks superimposed with a general decrease in the number of TCs.

3) ANALYSIS OF TC INTENSITY

Consistent with Fig. 3b, TCs simulated by the uniform T359 experiment are weaker than reported in IBTrACS, as illustrated by both the lifetime minimum pressure (983 vs 962 hPa on average, Fig. 6a) and maximum wind speed (31 vs 36 m s^{-1} on average, Fig. 6b). This bias is partly corrected in the rotated-stretched configuration (SIO-P, 975 hPa and 37 m s^{-1} on average). TC intensity is significantly increased in the SIO-F experiment (971 hPa and 39 m s^{-1} on average), which is again in line with the existing literature (e.g., Walsh et al. 2016). Interestingly, most of this increase in intensity arises

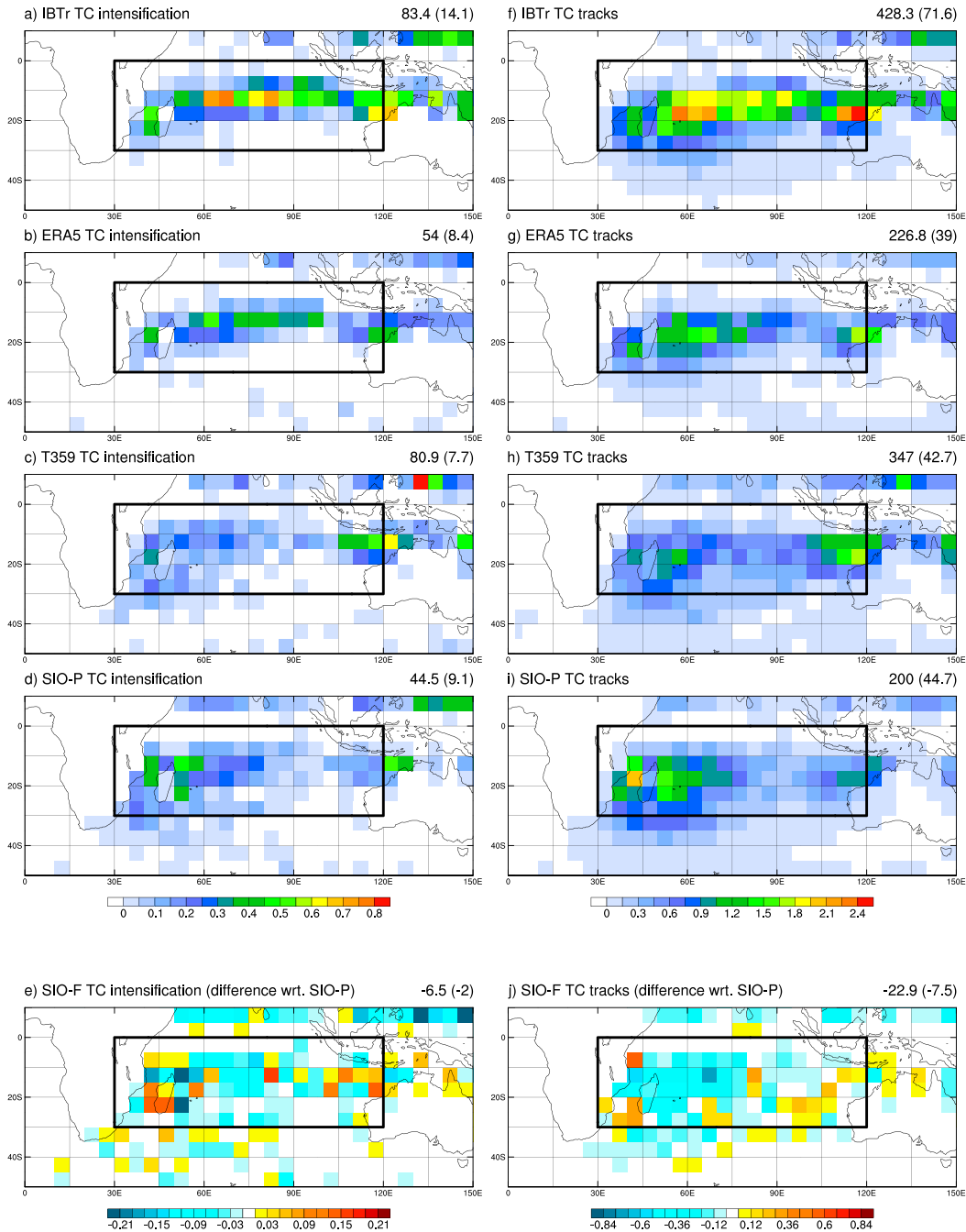


FIG. 5. (a)–(e) Frequency of TC intensification points (i.e., first TC point for each trajectory) (in number of points per year and per 5° × 5° grid box) for (a) IBTrACS, (b) ERA5, (c) T359, (d) SIO-P, and (e) SIO-F represented as a difference relative to (d). (f)–(j) As in (a)–(e), but for TC tracks (i.e., all TC points for each trajectory). Sums over the globe and for the SIO domain (in parentheses) are indicated in the top-right corner of each panel.

from the core of the distribution: TCs with an intensity below the median of the present-day distribution occur less frequently in the future experiment (40% of TCs in SIO-F vs 50% in SIO-P by definition), while TCs with an intensity between the 60th and 80th percentiles of the present-day distribution are more frequent (30% vs

20% by definition). (Values are similar for both minimum pressure and maximum wind.) Extremely intense TCs also contribute to the intensity increase: about 6%–7% of the future TCs exceeds the 95th percentile of the present-day intensity distribution (low pressure or high winds), so that even if the overall number of TCs

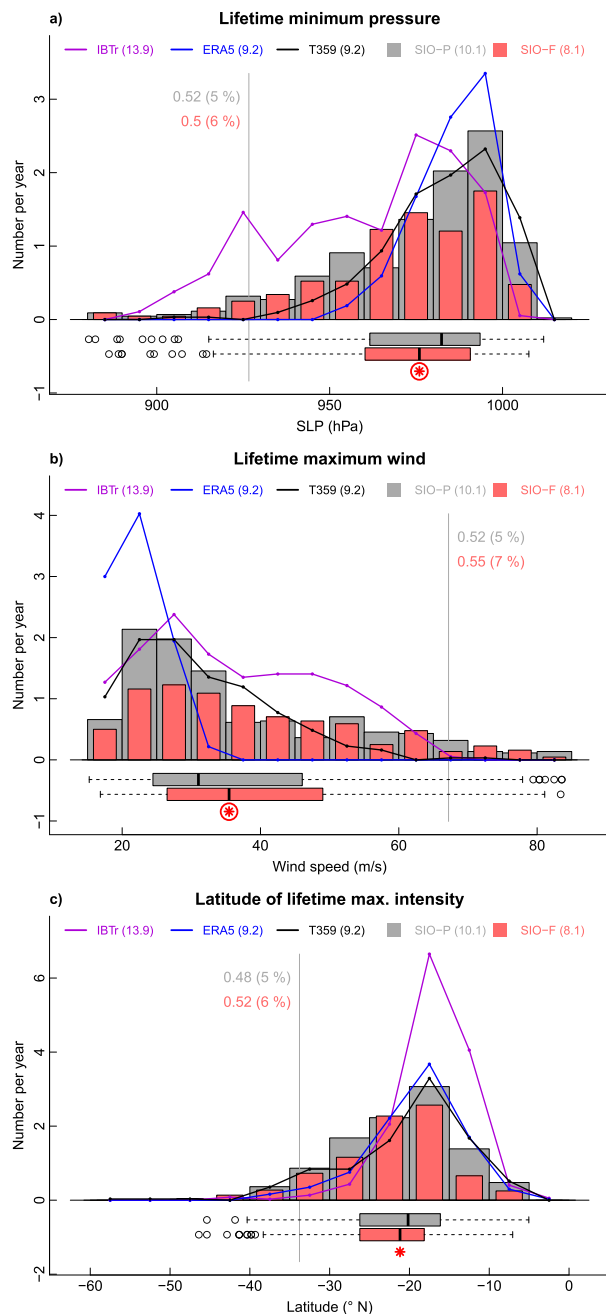


FIG. 6. (a) Frequency histogram (in number of systems per year) of the TC lifetime minimum pressure (hPa) for IBTrACS (violet line), ERA5 (blue line), T359 (black line), SIO-P (gray bars), and SIO-F (red bars). (b) As in (a), but for the lifetime maximum wind (m s^{-1}). (c) As in (a), but for the latitude of the lifetime minimum pressure ($^{\circ}\text{N}$). For SIO-P and SIO-F, probability distributions are also represented (boxplots). Red (circled) asterisks indicate differences between SIO-P and SIO-F averages that are significant at the 90% (95%) level following a *t* test.

decreases by 20% (Fig. 4), the number of extremely intense TCs remains constant (about 0.5 yr^{-1} with this definition). Similar results are obtained from the accumulated cyclone energy (not shown).

The increase in TC intensity in the rotated-stretched experiments is associated with a 90% level significant poleward shift of the lifetime maximum intensity (Fig. 6c). Although this is qualitatively consistent with the literature (e.g., Kossin et al. 2013), here we find a relatively weak shift of about 1°S in 80 years (22.3°S for SIO-F vs 21.3°S for SIO-P on average). This shift is related to a poleward extension of the tracks: while latitudes of genesis and intensification do not change significantly, the latitude of cyclolysis is shifted by 1.4°S on average (26.9° vs 25.5°S). Model biases in the spatial density of tracks (Fig. 5) are reflected in the distribution of the latitude of maximum lifetime intensity: too many (few) tracks at high (low) latitudes. Part of the discrepancy between model experiments and IBTrACS could arise from the tracking algorithm, since the ERA-5 distribution shows a similar poleward displacement.

Last, the increase in TC intensity is also related to a slightly longer TC stage (5.7 vs 5.4 days on average) that incorporates more TC days (5.5 vs 5.1 on average). Over the whole system lifetime, this increase is compensated by decreases in the duration of both development (1.9 vs 2.1 days) and cyclolysis (2.4 vs 2.5 days) stages; however, only the shorter development stage is statistically significant at the 95% level (not shown). (The terminology of the different stages is defined in section 3a.)

4) ANALYSIS OF SEASONAL CYCLE

An interesting feature revealed by the rotated-stretched experiments is that the cyclone season is found to be shorter under future climate conditions (Fig. 7). In the SIO-P experiment, the first (last) TC of the season—July to June—starts on average on 12 November (28 April), so that the cyclone season—defined here as the difference between these two dates—lasts on average 172 days. These values are very close to the uniform T359 experiment (12 November to 21 April, 165 days) and to the IBTrACS observations (7 November to 28 April, 177 days). In the SIO-F experiment, the season begins on average 32 days later (14 December), ends 9 days earlier (19 April), and thus lasts 41 days less than in SIO-P. The later onset and the shorter duration of the season are significant at the 95% level. These changes result from a strong decrease in the number of TCs occurring in the austral winter: in SIO-P, 17 TCs (3.8% on the total number) are detected during the months of June–September and 16 (3.6%) in October, versus 2 (0.6%) and 3 (0.8%), respectively, in SIO-F. Note that such wintertime systems are realistic: 9 systems are recorded over 1980–2016 in IBTrACS in

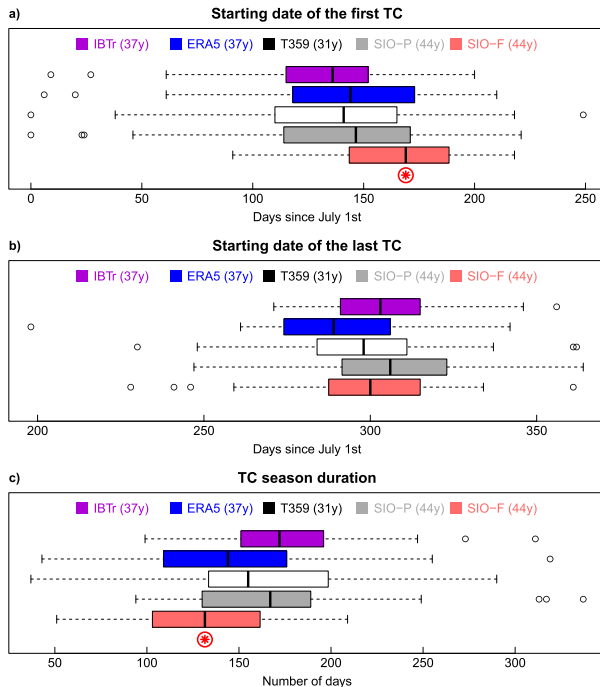


FIG. 7. As in Fig. 4, but for (a) the date of the first TC intensification within the season, (b) the date of the last TC intensification within the season, and (c) the TC season duration measured as the difference between (b) and (a).

June–September and 11 in October (i.e., 1.7% and 2.1% of the total number), with 6 systems reaching at least the *severe tropical storm* (category 2) stage (winds above 25 m s^{-1}), including one *tropical cyclone* (category 3) system (33 m s^{-1} ; Oscar in October 1983) and two *intense tropical cyclone* (category 4) systems (47 m s^{-1} ; Bellamine in October 1996 and Anais in October 2012) according to Météo-France (BoM) classifications (again, we use the terminology of the local RSMCs in this paper, not the Saffir–Simpson scale.). As a consequence of the winter decrease, the relative fraction of TCs occurring during the austral summer increases, especially during the months of February, March, and April (57% of TCs in SIO-F vs 51% in SIO-P). Further elements about this seasonal redistribution of TCs are discussed later.

b. Analysis of cyclogenesis indices

1) CGIs IN HIGH-RESOLUTION EXPERIMENTS

Previous studies have shown that CGIs can capture the geographical distribution of cyclone activity fairly well (e.g., Menkes et al. 2012). This is verified here over the SIO basin by comparing the aggregate index (average of CGIs, see section 3) computed on the ERA-5 data (Fig. 8a) with observed TC track densities (Figs. 5a,f). CGIs are indeed able to represent both the fraction of

global cyclone activity that occurs within the SIO basin (12.5 out of 84 TCs yr^{-1} on average, similar to IBTrACS values) and its spatial distribution within the basin with a local maximum around 10°S , 75°E (spatial correlation of 0.73 between Figs. 5a and 8a when remapped onto the same $5^{\circ} \times 5^{\circ}$ grid). The agreement between indices and actual track densities is less clear for the SIO-P experiment: CGIs suggest that cyclone activity should preferably occur within a latitudinally narrow area expanding from Madagascar to Indonesia similarly to ERA-5 (Fig. 8b) whereas TC tracks were detected more uniformly in the western part of the basin (Figs. 5d,i, spatial correlation of 0.54 between Figs. 5b and 8d). Possible reasons for this discrepancy can be that (i) the native resolution in SIO-P is nonuniform across the basin, (ii) CGIs were fitted on observations and reanalysis, so that coefficients used in their computation do not reflect the model characteristics, and (iii) the model (and the tracking algorithm) seem to have difficulties to simulate (detect) TCs at low latitudes, as reported in section 4a and Fig. 5.

CGIs fail to capture the 20% decrease in TC frequency between SIO-P and SIO-F that is observed in Figs. 5e,j (Fig. 8c). They instead indicate an unchanged cyclone activity on average over the SIO basin (difference of $+0.4 \text{ TCs yr}^{-1}$). This result is consistent with results of Chauvin et al. (2020) over the North Atlantic basin and also agrees with Camargo et al. (2014), who compared CGIs and actual TC tracks in high-resolution experiments from another model. Within the basin, the spatial pattern of changes in CGIs mostly consists in a poleward shift of the cyclone activity area, which is qualitatively consistent with changes in densities of tracks (Figs. 5e,j, spatial correlation of 0.25 between Figs. 5e and 8c) and with the poleward displacement of the location of lifetime maximum intensity (Fig. 6c). CGIs also support an increased cyclone activity north of Madagascar and in the Mozambique channel, as seen in the TC tracks. In other words, CGIs miss the overall decrease in TC frequency but seem to capture part of the changes in the regional distribution of TC tracks.

Further, breaking down changes in CGIs into dynamical and thermal components indicates that both contribute almost equally to the poleward shift of the cyclone activity area (Figs. 8d–f). They differ the most in the western part of the basin, especially north of the Mascarene Islands, where dynamical variables support a decrease in cyclone activity—consistent with the decrease in the number of TC tracks (Fig. 5j)—which is almost entirely compensated by the thermal contribution. One could interpret such a decrease in the dynamical component as less favorable conditions for cyclogenesis (i.e., decreased TC frequency), while the

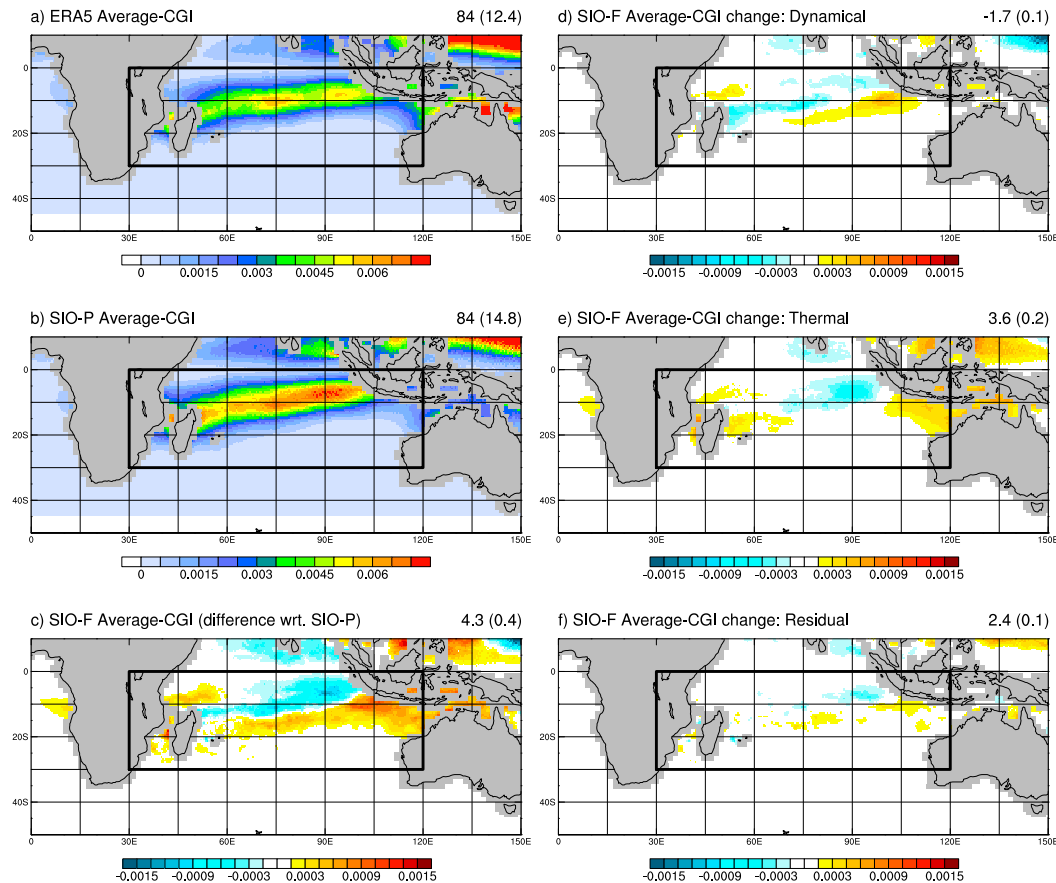


FIG. 8. (left) Annual mean of averaged CGIs (in number of TCs yr^{-1} and per $0.5^\circ \times 0.5^\circ$ grid box) for (a) ERA5, (b) SIO-P, and (c) SIO-F represented as a difference relative to (b). (right) Contributions of (d) dynamical components, (e) thermal components, and (f) residuals to (c). Sums over the globe and for the SIO domain (in parentheses) are indicated in the top-right corner of each panel.

increase in the thermal component could be indicative of more favorable conditions for intensification (i.e., increased TC intensity). However, this simple interpretation should be moderated by the fact that dynamical predictors can also be important for intensification (e.g., the vertical wind shear modulates the TC intensity), while thermal predictors can also be important for cyclogenesis (e.g., the midlevel relative humidity is relevant to spinning up the midlevel vortex in the early development). The CGI increase in the Mozambique channel solely arises from the thermal contribution, in line with a greater SST increase in this area compared to the rest of the basin (Fig. 1). The residual contribution is generally small but can be substantial especially in the eastern part of the basin.

Last, while results discussed above are based on the aggregate CGI, similar conclusions can be drawn from each index taken separately (not shown). In particular the spatial pattern of the SIO-F versus SIO-P difference (Fig. 8c) is common to all indices, albeit the spatial

average over the domain differs (+0.4, +1.3, and -0.6 TCs per year for CYGP, GPI, and TIPP, respectively). As all the three indices share the same dynamical variables, there is little interindex dispersion in the dynamical contribution presented in Fig. 8d. Discrepancies in the thermal contribution, that is strongly positive for the GPI and slightly negative for the TIPP, therefore explain most of the differences between indices, suggesting that some thermal variables are more relevant than others to capture climate-related changes in cyclone activity.

2) CGIS IN CMIP5 MODELS

Here we assess whether changes in CGIs obtained in high-resolution CNRM-CM6-1 experiments are representative of changes in CGIs obtained in low-resolution multimodel CMIP5 projections. In the following we indicate CMIP5 ensemble-mean values together with the 10th and 90th percentiles of CMIP5 distribution between parentheses—as the ensemble contains 14

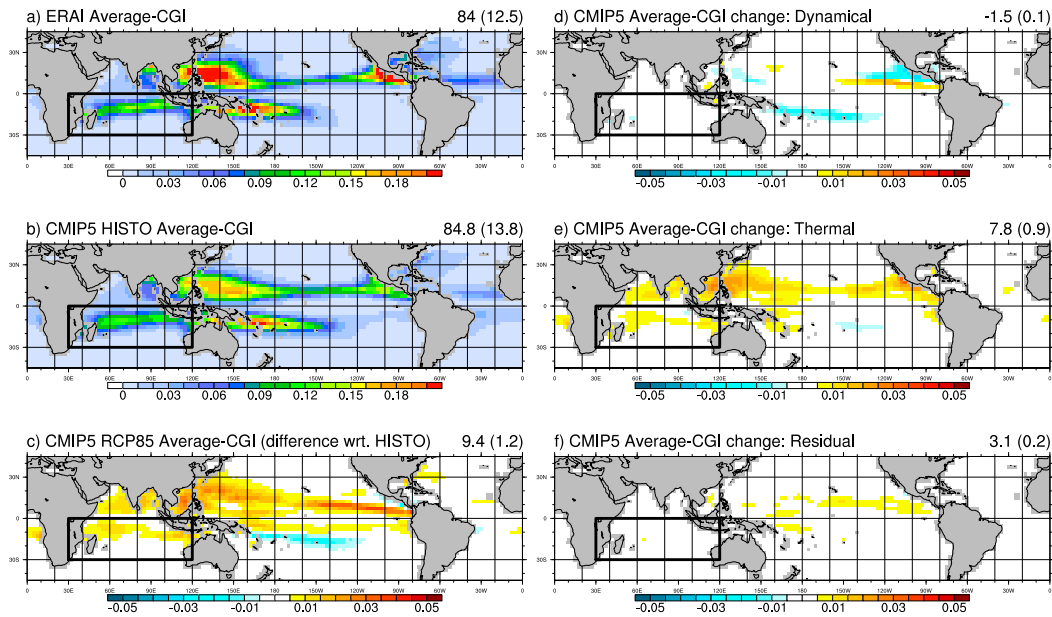


FIG. 9. (left) Annual mean of averaged CGIs (in number of TCs yr^{-1} and per $2.5^\circ \times 2.5^\circ$ grid box) for (a) ERAI, (b) CMIP5 ensemble mean historical simulations over 1976–2005, and (c) CMIP5 ensemble-mean RCP8.5 simulations over 2070–99 represented as a difference relative to (b). (right) Contributions of (d) dynamical components, (e) thermal components, and (f) residuals to (c). Sums over the globe and for the SIO domain (in parentheses) are indicated in the top-right corner of each panel.

models, this range excludes the two lowest and two highest values.

First, comparing ERA-Interim (80-km resolution, interpolated onto a 2.5° grid, Fig. 9a) with ERA-5 (30-km resolution, interpolated onto a 0.5° grid, Fig. 8a) shows that the resolution has little effect on the computation of CGIs; this was expected since these indices are designed to account for large-scale conditions. Both reanalyses indeed result in a similar fraction of cyclone activity in the SIO (about 15% of the global activity) and a similar spatial pattern within the basin. CMIP5 models have been shown to represent the geographical climatology of several CGIs fairly well (Camargo 2013), which is here confirmed by our aggregate CGI (Fig. 9b), although the ensemble averaging tends to smooth hotspots of cyclone activity due to intermodel dispersion in the exact location of local maxima. On average, about 16% [14%–20%] of the global cyclone activity occurs in the SIO, which is consistent with reanalyses. [A more detailed analysis of individual CMIP5 model biases can be found in Camargo (2013) and is considered to be beyond the scope of this paper.] Importantly, we have verified that our SIO-P high-resolution experiment lies within the range of CMIP5 models in terms of representation of present-day climatology of CGIs (not shown).

In future RCP8.5 projections, CMIP5 models simulate an overall increase in CGIs, slightly less pronounced

over the SIO (+9% [–8% to 20%]) than globally (+11% [–2% to 20%], Fig. 9c). Our results based on an aggregate CGI are consistent with the GPI analysis reported in Camargo (2013), although the GPI is the index that projects the strongest ensemble-mean increase: +16.3 (+2.8) TCs per year at global scale (in the SIO basin) versus +7.7 (+0.2) and +4.1 (+0.6) for the CYGP and the TIPP, respectively.

The global increase in CGIs projected by CMIP5 models (+11%, i.e., +9.4 TCs per year) arises from the thermal contribution (+7.8 TCs per year), while the dynamical component exhibits a small decrease (–1.5, Figs. 9d–f). The latter is robust across indices (–2, –1.2, and –1.3 for CYGP, GPI, and TIPP, respectively), while the former is the strongest for GPI (+14.7) and the lowest for TIPP (+3). This is consistent with CGIs applied to high-resolution experiments and supports the idea that changes in dynamical conditions could be related to changes in TC frequency (e.g., less favorable weather for cyclogenesis), while changes in thermal conditions could be related to changes in TC intensity (e.g., more available energy for intensification). This may be particularly the case for the GPI that includes the potential intensity introduced by Emanuel (1988) in its thermal component (Emanuel and Nolan 2004). Again, this interpretation should nevertheless be moderated because the relationship between dynamical versus thermal components and TC genesis versus intensification is not straightforward.

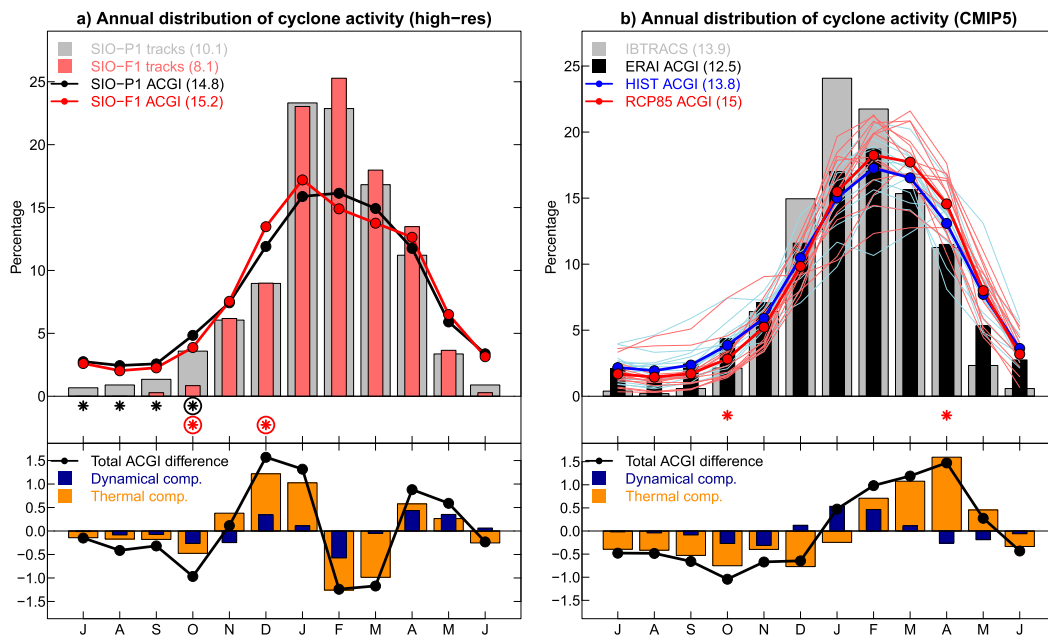


FIG. 10. (a) Annual distribution of SIO-P (gray bars) and SIO-F (red bars) TCs, and SIO-P (black line) and SIO-F (red line) aggregate CGI. Black (circled) asterisks indicate differences between bars that are significant at the 90% (95%) level; red (circled) asterisks indicate differences between lines that are significant at the 90% (95%) level. (b) Annual cycle of IBTrACS TCs (gray bars), and ERA-Interim (black bars), CMIP5 historical (blue lines), and RCP8.5 (red lines) averaged CGIs, with thick lines for ensemble means. Red (circled) asterisks indicate differences between ensemble means that are significant at the 90% (95%) level. All cycles are normalized and represented in percent per month. (bottom) Decomposition of the total aggregate CGI difference (black line) into dynamical (blue bars) and thermal (orange bars) components.

With a +0.4 TCs per year increase in the SIO (Fig. 8c), the SIO-F versus SIO-P difference is consistent with the range of CMIP5 projections. A fair comparison is, however, difficult since time periods used to evaluate changes differ. Interestingly, spatial patterns of CGI changes in the SIO are similar between high-resolution CNRM-CM6-1 experiments and the CNRM-CM5 experiment included in the CMIP5 ensemble (not shown). This is not completely surprising since SIO-P and SIO-F experiments use SST taken from this CNRM-CM5 simulation, but suggests that changes in large-scale environmental variables associated with cyclone activity are robust across the two versions of the atmospheric model and the two grid configurations. The poleward shift of cyclone activity suggested by CNRM-CM6-1 aggregate CGIs is, however, not representative of the CMIP5 ensemble that rather projects a reinforcement of cyclone activity close to the equator (Fig. 9c). This highlights that changes in the geographical distribution of cyclone activity captured by CGIs can be model dependent (e.g., Camargo 2013).

3) ANALYSIS OF CGIS' ANNUAL CYCLE

Globally, CGIs have been shown to represent the annual cycle of TC occurrence fairly well, although

with a weaker seasonal amplitude (Menkes et al. 2012). This is confirmed here by our high-resolution experiments: in the SIO-P experiment, 90% of the TC tracks occur from November to May while the aggregate CGI would indicate 78% (Fig. 10a). As discussed above (Fig. 7), we find a dramatic decrease in TC frequency during the austral winter in the SIO-F experiment, which translates into a significant decrease in the relative TC occurrence from June to October, counterbalanced by an increase—albeit not significant—from February to April. This redistribution is partly explained by CGIs, which also support a relative decrease of cyclone activity in winter (significant in October) and a relative increase in summer (significant in December). The fact that relative changes disagree between TC tracks and CGIs in February and March could be due to sampling uncertainty since they are not statistically significant.

Annual cycles of both TC occurrence and CGIs simulated by the SIO-P experiment are consistent with IBTrACS and ERA-Interim, respectively (Fig. 10b). In particular, 94% of IBTrACS TCs occur from November to May while the ERA-Interim aggregate CGI would indicate 82%. CMIP5 historical simulations are generally consistent with ERA-Interim in that aspect,

although they tend to underestimate (overestimate) the proportion of cyclone activity in early (late) summer: 49% (41%) from November to February (March to June) on average over the ensemble versus 54% (35%) in ERA-Interim. Projected changes in the RCP8.5 simulations are indicative of relative decrease of cyclone activity from June to December (significant in October) counterbalanced by a relative increase from January to May (significant in April). Such a seasonal redistribution of cyclone activity is fully consistent with results from our high-resolution experiments, suggesting that this feature of TC changes could be robust across models. Last, both dynamical and thermal components contribute to reshaping the annual cycle of CGIs, although monthly contributions differ: for instance, in CMIP5, the CGI relative increase in summer is mostly explained by the dynamical component in January, by the thermal component in March and April, and by both in February.

5. Discussion

In this paper we have tried to assess projected changes in the SIO cyclone activity from two complementary approaches: (i) high-resolution experiments with our in-home model (CNRM-CM6-1) that simulates realistic TCs and allows for a statistical analysis of TC characteristics and (ii) low-resolution multimodel climate projections in which cyclone activity can only be estimated from empirical indices built on large-scale environmental variables. Although we have shown that robust results emerge, both approaches used in this study suffer from clear limitations.

First, our high-resolution experiments are performed in an atmosphere-only framework (i.e., with prescribed SST), whereas the atmosphere strongly interacts with the near-surface ocean during TCs. Daloz et al. (2012) have shown that the ocean–atmosphere coupling can modify the simulation of TCs by the rotated-stretched configuration of the CNRM-CM model, the impact being sensitive to the coupling frequency. However, in their review paper, Walsh et al. (2016) assess that atmosphere–ocean coupling only has a limited effect on climate change experiments. In addition, using an atmosphere-only framework allows us to correct for potential biases in SST (as done in our experimental design).

Second, results obtained with the rotated-stretched configuration might be sensitive to the arbitrary choice of the grid pole location (Daloz et al. 2012). In the present study, the focus has been intentionally made on the western part of the SIO, in order to better assess potential changes in TCs over the area enclosing Mozambique, Madagascar, and the Mascarene Islands

[i.e., the region under the responsibility of Météo-France (local RSMC)]. In exchange, the resolution was not dramatically increased at the other side of the SIO (Australian shore) compared to the uniform T359 grid. We are nevertheless confident (from our expertise with the rotated-stretched configuration) that a small displacement of the grid pole would not have altered the results significantly. The fact that the uniform T359 experiment (50 km) simulates reasonable TCs gives us additional confidence that results of rotated-stretched experiments are robust across the whole SIO basin. Last, our results share some similarities with Chauvin et al. (2020), which suggests that the main conclusions could be robust among oceanic basins, although a more systematic analysis would be needed.

A third limitation of our experimental protocol is that it only includes one member per experiment, which could raise questions about our ability to disentangle climate change signal from the noise of internal variability. More ensemble members would probably have smoothed the changes in track densities presented in Fig. 5; we were nevertheless able to detect a few statistically significant changes at the basinwide scale, such as the decrease in the overall number of TCs or the reduction in the duration of the cyclone season. In their analysis of the North Atlantic basin, Chauvin et al. (2020) performed five members per experiment and concluded that although this provides robustness in results obtained at regional scale, one member of 50 years is sufficient for the large-scale signal to emerge.

A follow-up question is the sensitivity of our results to the unique model used to perform high-resolution experiments (CNRM-CM6-1). Here we have shown that (i) our results are quantitatively similar to other high-resolution modeling studies (e.g., Murakami et al. 2012) and that (ii) large-scale environmental changes simulated by CNRM-CM6-1 lie in the range of CMIP5 uncertainties. However, the issue of model dependency will not be properly tackled until multimodel ensembles of high-resolution climate projections exist, and the upcoming HighResMIP exercise (Haarsma et al. 2016) can be considered as a promising first step to that regard.

Last, statistical tools used to analyze both high-resolution experiments (TC tracking algorithm) and multiple low-resolution model datasets (computation of CGIs) can be questioned. The TC tracking algorithm uses several arbitrary thresholds (winds, vorticity, temperature) that clearly affect the number of systems detected; however, we have verified that our main findings remain unchanged when using slightly different thresholds (not shown). The computation of CGIs is also problematic as the choice of the predictors (environmental variables) and the fit of their coefficients are likely to be model

sensitive; using 3 indices and 14 models was a way to take this source of uncertainty into account, and building more sophisticated and possibly model-dependent CGIs is left for future work.

6. Conclusions

The aim of this study was to assess projected changes in the SIO tropical cyclone (TC) activity from both high-resolution CNRM-CM6-1 dedicated experiments and CMIP5 multimodel climate projections. Our main findings can be summarized as follows:

- the uniform T359 (50 km) configuration of the CNRM-CM6-1 model is able to simulate realistic TCs in terms of frequency and pressure–wind relationship, although with a weaker intensity than observed. The rotated-stretched configuration improves the realism of simulated TCs (especially in terms of intensity) over the area of interest.
- Rotated-stretched high-resolution experiments project a 20% decrease in the SIO TC frequency between 1965–2014 and 2045–94 in the RCP8.5 scenario. In the meantime, they indicate an increase in the maximum lifetime intensity, and a slight poleward extension of the TC tracks. As a consequence, the frequency of the strongest TCs is projected to remain nearly constant.
- Rotated-stretched high-resolution experiments project a substantial reduction of the cyclone season duration; in particular the first TC of the season is projected to occur 1 month later on average (mid-December vs mid-November). Although the raw number of TCs is projected to decrease for all individual months, cyclone activity is redistributed within the season, with a smaller (greater) relative proportion of cyclones occurring in early (late) summer. This result may be important for Regional Specialized Meteorological Centres and local administrations in charge of TC monitoring and alertness.
- Cyclogenesis indices (CGIs) applied to high-resolution experiments fail to capture the projected decrease in overall TC frequency. However, they are able to partially represent changes in the spatiotemporal distribution of cyclone activity, such as the poleward shift and the seasonal redistribution. This may not be surprising as CGIs are designed to represent not the total number of TCs but their spatiotemporal distribution.
- Changes in CGIs obtained from CNRM-CM6-1 lie in the range of CMIP5 projections. In particular the seasonal redistribution of cyclone activity is consistent across models.

Future work will involve further understanding of the decreasing TC frequency in CNRM-CM6-1 experiments: whether this results from less frequent initiations of

small-scale vortices or from less favorable conditions to intensification into TCs will be particularly scrutinized in the light of the work of [Duvel \(2015\)](#). Besides, the computation of CGIs in high-resolution experiments can be viewed as a first step into the physical understanding of changes in cyclone activity, and future analyses will further explore how they relate to changes in large-scale environmental features such as the Indian monsoon, the Madden–Julian oscillation, and/or the Hadley–Walker circulation. Impact studies may also be conducted to assess consequences of the projected changes in cyclone activity on associated phenomena such as rainfall or storm surges. Expanding the analysis to the new generation of climate models (CMIP6)—especially those with sufficiently high resolutions to simulate realistic TCs—will also be naturally considered for future work.

Finally, a promising perspective of this study is to pursue the efforts to reconcile results on TCs derived from high-resolution experiments with CGIs computed on low-resolution climate projections. In this paper we have shown that although CGIs miss the overall decrease in the number of TCs, they partially capture changes in their spatiotemporal distribution. Further, we have shown that the future increase in CGIs is mostly driven by their thermal component, while their dynamical component slightly decreases. The fact that these indices are empirically fitted on present-day cyclone activity features might give too much weight to the thermal component in a climate change context. Future research may therefore focus on the development of cyclogenesis indices that remain relevant for assessing climate change, taking advantage of high-resolution climate projections distributed within CMIP6 and possibly using more comprehensive statistical learning techniques.

Acknowledgments. This work has been partly supported by the ReNovRisk-C3 project within the Indian Ocean INTERREG-V Programme 2014–20. J.C. thanks all people at LACy and Météo-France La Réunion for their welcome and fruitful discussions, and Rémy Lee-Ah-Siem for technical support.

REFERENCES

- Atkinson, G., and C. Holliday, 1977: Tropical cyclone minimum sea level pressure/maximum sustained wind relationship for the western North Pacific. *Mon. Wea. Rev.*, **105**, 421–427, [https://doi.org/10.1175/1520-0493\(1977\)105<0421:TCMSLP>2.0.CO;2](https://doi.org/10.1175/1520-0493(1977)105<0421:TCMSLP>2.0.CO;2).
- Camargo, S., 2013: Global and regional aspects of tropical cyclone activity in the CMIP5 models. *J. Climate*, **26**, 9880–9902, <https://doi.org/10.1175/JCLI-D-12-00549.1>.

- , M. Tippet, A. Sobel, G. Vecchi, and M. Zhao, 2014: Testing the performance of tropical cyclone genesis indices in future climates using the HiRAM model. *J. Climate*, **27**, 9171–9196, <https://doi.org/10.1175/JCLI-D-13-00505.1>.
- Chauvin, F., J.-F. Royer, and M. Déqué, 2006: Response of hurricane-type vortices to global warming as simulated by ARPEGE-Climat at high resolution. *Climate Dyn.*, **27**, 377–399, <https://doi.org/10.1007/s00382-006-0135-7>.
- , R. Pilon, P. Palany, and A. BelMadani, 2020: Future changes in Atlantic hurricanes with the rotated-stretched ARPEGE-Climat at very high resolution. *Climate Dyn.*, **54**, 947–972, <https://doi.org/10.1007/s00382-019-05040-4>.
- Daloz, A. S., F. Chauvin, and F. Roux, 2012: Impact of the configuration of stretching and ocean–atmosphere coupling on tropical cyclone activity in the variable-resolution GCM ARPEGE. *Climate Dyn.*, **39**, 2343–2359, <https://doi.org/10.1007/s00382-012-1561-3>.
- Dee, D., and Coauthors, 2011: The ERA-Interim reanalysis: Configuration and performance of the data assimilation system. *Quart. J. Roy. Meteor. Soc.*, **137**, 553–597, <https://doi.org/10.1002/qj.828>.
- Duvel, J.-P., 2015: Initiation and intensification of tropical depressions over the southern Indian Ocean: Influence of the MJO. *Mon. Wea. Rev.*, **143**, 2170–2191, <https://doi.org/10.1175/MWR-D-14-00318.1>.
- Emanuel, K., 1988: The maximum intensity of hurricanes. *J. Atmos. Sci.*, **45**, 1143–1155, [https://doi.org/10.1175/1520-0469\(1988\)045<1143:TMIOH>2.0.CO;2](https://doi.org/10.1175/1520-0469(1988)045<1143:TMIOH>2.0.CO;2).
- , and D. Nolan, 2004: Tropical cyclone activity and the global climate system. Preprints, *26th Conf. on Hurricanes and Tropical Meteorology*, Miami, FL, Amer. Meteor. Soc., 240–241.
- Gray, W. M., 1975: Tropical cyclone genesis. Atmospheric Science Paper 234, Colorado State University, 121 pp.
- Haarsma, R., and Coauthors, 2016: High Resolution Model Intercomparison Project (HighResMIP v1.0) for CMIP6. *Geosci. Model Dev.*, **9**, 4185–4208, <https://doi.org/10.5194/gmd-9-4185-2016>.
- Held, I., and M. Zhao, 2011: The response of tropical cyclone statistics to an increase in CO₂ with fixed sea surface temperatures. *J. Climate*, **24**, 5353–5364, <https://doi.org/10.1175/JCLI-D-11-00050.1>.
- Hersbach, H., and Coauthors, 2018: Operational global reanalysis: Progress, future directions and synergies with NWP. ERA Rep. Series 27, 65 pp, <https://doi.org/10.21957/tkic6g3wm>.
- Holland, G., and C. Bruyère, 2014: Recent intense hurricane response to global climate change. *Climate Dyn.*, **42**, 617–627, <https://doi.org/10.1007/s00382-013-1713-0>.
- Knapp, K., M. Kruk, D. Levinson, H. Diamond, and C. Neumann, 2010: The International Best Track Archive for Climate Stewardship (IBTrACS). *Bull. Amer. Meteor. Soc.*, **91**, 363–376, <https://doi.org/10.1175/2009BAMS2755.1>.
- Knutson, T., and Coauthors, 2010: Tropical cyclones and climate change. *Nat. Geosci.*, **3**, 157–163, <https://doi.org/10.1038/ngeo779>.
- , J. Sirutis, M. Zhao, R. Tuleya, M. Bender, G. Vecchi, G. Villarini, and D. Chavas, 2015: Global projections of intense tropical cyclone activity for the late twenty-first century from dynamical downscaling of CMIP5/RCP4.5 scenarios. *J. Climate*, **28**, 7203–7224, <https://doi.org/10.1175/JCLI-D-15-0129.1>.
- Kossin, J., 2018: A global slowdown of tropical-cyclone translation speed. *Nature*, **558**, 104–107, <https://doi.org/10.1038/s41586-018-0158-3>.
- , T. Olander, and K. Knapp, 2013: Trend analysis with a new global record of tropical cyclone intensity. *J. Climate*, **26**, 9960–9976, <https://doi.org/10.1175/JCLI-D-13-00262.1>.
- Kuleshov, Y., R. Fawcett, L. Qi, B. Trewin, D. Jones, J. McBride, and H. Ramsay, 2010: Trends in tropical cyclones in the South Indian Ocean and the South Pacific Ocean. *J. Geophys. Res.*, **115**, D01101, <https://doi.org/10.1029/2009JD012372>.
- Malan, N., C. Reason, and B. Loveday, 2013: Variability in tropical cyclone heat potential over the Southwest Indian Ocean. *J. Geophys. Res. Oceans*, **118**, 6734–6746, <https://doi.org/10.1002/2013JC008958>.
- Menkes, C., M. Lengaigne, P. Marchesio, N. Jourdain, E. Vincent, J. Lefèvre, F. Chauvin, and J.-F. Royer, 2012: Comparison of tropical cyclogenesis indices on seasonal to interannual time-scales. *Climate Dyn.*, **38**, 301–321, <https://doi.org/10.1007/s00382-011-1126-x>.
- Murakami, H., and Coauthors, 2012: Future changes in tropical cyclone activity projected by the new high-resolution MRI-AGCM. *J. Climate*, **25**, 3237–3260, <https://doi.org/10.1175/JCLI-D-11-00415.1>.
- Peng, M., B. Fu, T. Li, and D. Stevens, 2012: Developing versus nondeveloping disturbances for tropical cyclone formation. Part I: North Atlantic. *Mon. Wea. Rev.*, **140**, 1047–1066, <https://doi.org/10.1175/2011MWR3617.1>.
- Rayner, N. A., D. Parker, E. Horton, C. Folland, L. Alexander, D. Rowell, E. Kent, and A. Kaplan, 2003: Global analyses of sea surface temperature, sea ice, and night marine air temperature since the late nineteenth century. *J. Geophys. Res.*, **108**, 4407, <https://doi.org/10.1029/2002JD002670>.
- Royer, J.-F., and F. Chauvin, 2009: Response of tropical cyclogenesis to global warming in an IPCC AR4 scenario. *Hurricanes and Climate Change*, J. Elsner and T. Jagger, Eds., Springer, 213–234, https://doi.org/10.1007/978-0-387-09410-6_12.
- , —, B. Timbal, P. Araspin, and D. Grimal, 1998: A GCM study of the impact of greenhouse gas increase on the frequency of occurrence of tropical cyclones. *Climatic Change*, **38**, 307–343, <https://doi.org/10.1023/A:1005386312622>.
- Sugi, M., H. Murakami, and J. Yoshimura, 2012: On the mechanism of tropical cyclone frequency changes due to global warming. *J. Meteor. Soc. Japan*, **90A**, 397–408, <https://doi.org/10.2151/JMSJ.2012-A24>.
- Taylor, K., R. Stouffer, and G. Meehl, 2011: An overview of CMIP5 and the experiment design. *Bull. Amer. Meteor. Soc.*, **93**, 485–498, <https://doi.org/10.1175/BAMS-D-11-00094.1>.
- Tippet, M., S. Camargo, and A. Sobel, 2011: A Poisson regression index for tropical cyclone genesis and the role of large-scale vorticity in genesis. *J. Climate*, **24**, 2335–2357, <https://doi.org/10.1175/2010JCLI3811.1>.
- Voldoire, A., and Coauthors, 2013: The CNRM-CM5.1 global climate model: Description and basic evaluation. *Climate Dyn.*, **40**, 2091–2121, <https://doi.org/10.1007/s00382-011-1259-y>.
- , and Coauthors, 2019: Evaluation of CMIP6 DECK experiments with CNRM-CM6-1. *J. Adv. Model. Earth Syst.*, **11**, 2177–2213, <https://doi.org/10.1029/2019MS001683>.
- Walsh, K., and Coauthors, 2016: Tropical cyclones and climate change. *Wiley Interdiscip. Rev.: Climate Change*, **7**, 65–89, <https://doi.org/10.1002/WCC.371>.
- Wehner, M., Prabhat, K. A. Reed, D. Stone, W. D. Collins, and J. Bacmeister, 2015: Resolution dependence of future tropical cyclone projections of CAM5.1 in the U.S. CLIVAR Hurricane working group idealized configurations. *J. Climate*, **28**, 3905–3925, <https://doi.org/10.1175/JCLI-D-14-00311.1>.
- Woodruff, J., J. Irish, and S. Camargo, 2013: Coastal flooding by tropical cyclones and sea-level rise. *Nature*, **504**, 44–52, <https://doi.org/10.1038/nature12855>.



Article

Impact of Tropical Cyclones on Inhabited Areas of the SWIO Basin at Present and Future Horizons. Part 2: Modeling Component of the Research Program RENOVRIK-CYCLONE

Christelle Barthe, Olivier Bousquet, Soline Bielli, Pierre Tulet, Joris Planezze, Marine Claeys, Chia-Lun Tsai, Callum Thompson, François Bonnardot, Fabrice Chauvin et al.

Special Issue

Tropical Cyclones in the Indian Ocean




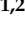

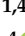
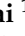

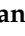
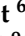


Edited by

Prof. Dr. Olivier Bousquet



Article

Impact of Tropical Cyclones on Inhabited Areas of the SWIO Basin at Present and Future Horizons. Part 2: Modeling Component of the Research Program RENOVRISK-CYCLONE

Christelle Barthe ^{1,2,*} , Olivier Bousquet ^{1,3} , Soline Bielli ¹ , Pierre Tulet ^{1,2} , Joris Pianezze ¹ , Marine Claeyes ^{1,4} , Chia-Lun Tsai ^{1,5} , Callum Thompson ¹ , François Bonnardot ⁶ , Fabrice Chauvin ⁴ , Julien Cattiaux ⁴ , Marie-Noëlle Bouin ^{4,7} , Vincent Amelie ⁸ , Guilhem Barruol ⁹ , Radiance Calmer ^{1,10} , Stéphane Ciccione ¹¹ , Emmanuel Cordier ¹² , Quoc-Phi Duong ¹ , Jonathan Durand ¹ , Frauke Fleischer-Dogley ¹³ , Romain Husson ¹⁴ , Edouard Lees ¹ , Sylvie Malardel ¹ , Nicolas Marquestaut ^{1,12} , Alberto Mavume ¹⁵ , Dominique Mékiès ¹ , Alexis Mouche ⁷ , Navalona Manitriniana Ravoson ¹⁶ , Bruno Razafindradingana ¹⁷ , Elisa Rindrahariasona ^{9,18} , Gregory Roberts ^{4,19} , Manvendra Singh ²⁰ , Lova Zakariasy ¹⁷ and Jonas Zucule ²¹



Citation: Barthe, C.; Bousquet, O.; Bielli, S.; Tulet, P.; Pianezze, J.; Claeyes, M.; Tsai, C.-L.; Thompson, C.; Bonnardot, F.; Chauvin, F.; et al. Impact of Tropical Cyclones on Inhabited Areas of the SWIO Basin at Present and Future Horizons. Part 2: Modeling Component of the Research Program RENOVRISK-CYCLONE. *Atmosphere* **2021**, *12*, 689. <https://doi.org/10.3390/atmos12060689>

Academic Editor: Corene Matyas

Received: 30 April 2021

Accepted: 26 May 2021

Published: 28 May 2021

Publisher's Note: MDPI stays neutral with regard to jurisdictional claims in published maps and institutional affiliations.



Copyright: © 2021 by the authors. Licensee MDPI, Basel, Switzerland. This article is an open access article distributed under the terms and conditions of the Creative Commons Attribution (CC BY) license (<https://creativecommons.org/licenses/by/4.0/>).

- 1 Laboratoire de l'Atmosphère et des Cyclones, Université de La Réunion, CNRS, Météo-France, 97400 Saint-Denis, France; olivier.bousquet@meteo.fr (O.B.); soline.bielli-bousquet@univ-reunion.fr (S.B.); pierre.tulet@aero.obs-mip.fr (P.T.); pianezze.joris@gmail.com (J.P.); marine.claeys@meteo.fr (M.C.); chialun@knu.ac.kr (C.-L.T.); callum-thompson@ucsb.edu (C.T.); radiance.calmer@colorado.edu (R.C.); quoc-phi.duong@meteo.fr (Q.-P.D.); durand.jonathan.2@uqam.ca (J.D.); edouard.lees@meteo.fr (E.L.); sylvie.malardel@meteo.fr (S.M.); nicolas.marquestaut@univ-reunion.fr (N.M.); dominique.mekies@meteo.fr (D.M.)
- 2 Laboratoire d'Aérodynamique, Université de Toulouse, UT3, CNRS, IRD, 31400 Toulouse, France
- 3 Institute for Coastal Marine Research, Nelson Mandela University, Port-Elizabeth 6031, South Africa
- 4 CNRM, Université de Toulouse, Météo-France, CNRS, 31057 Toulouse, France; fabrice.chauvin@meteo.fr (F.C.); julien.cattiaux@meteo.fr (J.C.); nbouin@ifremer.fr (M.-N.B.); greg.roberts@meteo.fr (G.R.)
- 5 Center for Atmospheric Remote Sensing (CARE), Department of Astronomy and Atmospheric Sciences, Kyungpook National University, Daegu 41566, Korea
- 6 Direction Interrégionale de Météo-France pour l'Océan Indien, 97400 Saint-Denis, France; francois.bonnardot@meteo.fr
- 7 Laboratoire d'Océanographie Physique et Spatiale, Université de Brest, CNRS, Ifremer, IRD, IUEM, 29280 Plouzané, France; Alexis.Mouche@ifremer.fr
- 8 Seychelles Meteorological Authority, Mahé 670311, Seychelles; v.amelie@meteo.gov.sc
- 9 Institut de Physique du Globe de Paris, Université de Paris, CNRS, 75005 Paris, France; barruol@ipgp.fr (G.B.); elisa.rindrahariasona@univ-reunion.fr (E.R.)
- 10 National Snow and Ice Data Center (NSIDC), Cooperative Institute for Research in Environmental Sciences, University of Colorado Boulder, Boulder, CO 80304, USA
- 11 Kelonia, Observatoire des Tortues Marines de La Réunion, 97436 Saint-Leu, France; stephane.ciccione@museesreunion.re
- 12 Observatoire des Sciences de l'Univers de La Réunion (UAR 3365 OSU-R), 97400 Saint-Denis, France; emmanuel.cordier@univ-reunion.fr
- 13 Seychelles Islands Foundation, Mahé 670311, Seychelles; ceo@sif.sc
- 14 Collecte Localisation Satellites (CLS), 29280 Brest, France; rhusson@cls.fr
- 15 Department of Physics, Faculty of Sciences, Eduardo Mondlane University, Maputo CP 257, Mozambique; alberto.mavume@uem.mz
- 16 Institut et Observatoire de Géophysique d'Antsiranana, Université d'Antsiranana, Antananarivo 101, Madagascar; ravossonaval3@gmail.com
- 17 Institut Supérieur de Technologie d'Antsiranana, Antsiranana 201, Madagascar; hbrazafindradingana@ist-antsiranana.mg (B.R.); lova.zakariasy@ist-antsiranana.mg (L.Z.)
- 18 Laboratoire GéoSciences Réunion (LGSR), Université de La Réunion, 97400 Saint-Denis, France
- 19 Scripps Institution of Oceanography, University of California, San Diego, CA 92093, USA
- 20 Mauritius Oceanography Institute, Albion 95410, Mauritius; msingh@moi.intnet.mu
- 21 Instituto Nacional de Meteorologia (INAM), Maputo CP 256, Mozambique; jnzucule@gmail.com
- * Correspondence: christelle.barthe@aero.obs-mip.fr

Abstract: The ReNovRisk-Cyclone program aimed at developing an observation network in the south-west Indian ocean (SWIO) in close synergy with the implementation of numerical tools to

model and analyze the impacts of tropical cyclones (TC) in the present and in a context of climate change. This paper addresses the modeling part of the program. First, a unique coupled system to simulate TCs in the SWIO is developed. The ocean–wave–atmosphere coupling is considered along with a coherent coupling between sea surface state, wind field, aerosol, microphysics, and radiation. This coupled system is illustrated through several simulations of TCs: the impact of air–sea flux parameterizations on the evolution of TC Fantala is examined, the full coupling developed during the program is illustrated on TC Idai, and the potential of novel observations like space-borne synthetic aperture radar and sea turtles to validate the atmosphere and ocean models is presented with TC Herold. Secondly, the evolution of cyclonic activity in the SWIO during the second half of the 21st century is assessed. It was addressed both using climate simulation and through the implementation of a pseudo global warming method in the high-resolution coupled modeling platform. Our results suggest that the Mascarene Archipelago should experience an increase of TC related hazards in the medium term.

Keywords: tropical cyclone; south-west Indian ocean; cloud-resolving model; ocean–wave–atmosphere coupling; climate modeling

1. Introduction

Due to the possible devastating combination of extreme winds, torrential precipitation, storm surge, and high waves, tropical cyclones (TC) are a major threat for impacted territories. This is particularly true in the South-West Indian Ocean (SWIO) that represents 10–12% of the global TC activity [1,2] and includes several countries with precarious economies and fragile infrastructures, making them highly vulnerable to cyclonic risks. Madagascar, which ranks among the poorest countries in the world, is regularly affected by TCs. Between 1999 and 2016, 34 systems directly hit Madagascar, 10 of which as a TC at the time of landfall [3]. In March 2004, TC Gafilo—the most intense TC ever observed in the SWIO at this date—made landfall in the north-east of Madagascar, leaving more than 200,000 victims, 400 deaths, and damages estimated at USD 250 million. In 2017, TC Enawo hit almost the same region of Madagascar at the peak of its intensity (maximum wind speed of 57 m s^{-1}). The associated storm surge, high winds and heavy rains led to 81 deaths, 300,000 victims, heavily damaged structures, and severe losses in rice fields (damages estimated at \sim USD 137 million). Mozambique is also frequently hit by tropical depressions with 16 direct hits between 1999 and 2016 [3]. In 2019, TC Idai made landfall in the region of Beira. Wind gusts and torrential rainfall devastated the crops, destroyed more than 29,500 houses, and damaged tens of thousands of others, leading to a major humanitarian crisis. More than 1000 people died and 2.6 million victims were reported. The damages were estimated at USD 2 billion in the impacted region (Mozambique, Malawi, Zimbabwe, Madagascar). Six weeks later, TC Kenneth, after devastating the Comoros archipelago, hit the north of Mozambique, in the region of Pemba, worsening the humanitarian, sanitary, and economic situation of the country. This high exposure to natural disaster adds to the dependence on agriculture and natural resources and leads to severe humanitarian crises, which are most of the time under-reported in the media.

Due to its relatively small size (\sim 60 km in diameter), La Réunion (21.1° S , 55.5° E) is not frequently directly hit by TCs but is regularly affected by systems passing at a few tens or hundreds of kilometers away. In 2002, the eye of TC Dina passed more than 65 km away from the north-west of the island. However, due to the strong winds, swell, and heavy rain, damages on the crops and infrastructures—in particular roads and electric networks—were estimated at several hundreds of thousands of euros. In 2007, TC Gamède passed at more than 200 km away from the island, but heavy rainfall (reinforced by the steep orography) and high swell (11.7 m recorded on the north-west shore) affected the island during several days. A rainfall rate of 4936 mm was recorded in 96 h at the Cratère Commerson rain gauge station [4]. Gamede was at the origin of damages estimated at

~100 millions of euros. Even if TCs do not directly hit inhabited regions, they can still have considerable economic and sanitary impact.

These few examples show the importance of an accurate forecasting of TC track, intensity, structure, and associated hazards several days in advance to prepare populations and infrastructures, evacuate the most exposed regions, and eventually prepare humanitarian aid. Despite undeniable improvements in TC forecasting, understanding and predicting rapid changes in track, intensity, and structure remain a challenge in particular near landfall [5]. This limitation can be attributed to a lack of observations over the oceans, to models limitations in terms of physical parameterizations and resolution, and to limited understanding of some physical processes involved in TC intensification. To advance in the numerical representation of TCs, it is important to develop coupled models and parameterizations to rely on coherent oceanic and atmospheric fields.

In the context of climate change, improving TC forecasting to protect goods and persons should go along with projections of TC risks on SWIO territories to anticipate and adapt for potential new risks. The impact of global warming on frequency, intensity, and precipitation rates of TCs is thoroughly documented in the literature (e.g., [6–12]). In a recent study, high-resolution experiments were used to estimate projected changes in cyclonic activity over the South Indian Ocean basin near the end of the century [13]. An interesting result of this study is related to an earlier onset (about 1 month) of the TC season, underlining the need to focus on what is occurring at the regional level.

The ReNovRisk program [14] aims at analyzing risks associated with TCs and their economical impact on the SWIO countries, to improve the resilience capability of those territories facing cyclonic hazards. ReNovRisk-Cyclone (RNR-CYC) is one of the four components of the global ReNovRisk program. It focuses on the meteorological and oceanic impact of TCs on the SWIO countries in the present and in the future. The four components of RNR-CYC and the observations implemented during this program are presented in the companion paper [15]. The objective of this paper is to present the modeling strategy of RNR-CYC in terms of forecasting and climate projection. The outline of the paper is as follows. Section 2 is dedicated to the presentation of the high-resolution modeling platform developed in the framework of this program to improve numerical forecasting of TCs. Several coupled simulations of TCs illustrate these developments in Section 3. Section 4 investigates potential changes in the frequency and intensity of TCs over the period 2015–2094 from high-resolution global climate simulation specifically made in the frame of RNR-CYC. Finally, conclusions and perspectives are given in Section 5.

2. Development of a Coupled System for TC Modeling

One of the main objectives of the RNR-CYC program is to develop and demonstrate the added value of a high-resolution (horizontal grid spacing less than 2.5 km) ocean–wave–atmosphere (OWA) modeling system for forecasting TCs and their impacts. This tool heralds the next generation of operational numerical weather prediction (NWP) systems to be used by Regional Specialized Meteorological Center (RSMC) La Réunion at mid-term.

Since an important source of energy for TCs is the heat and moisture extracted from the underlying upper ocean, the ocean–atmosphere coupling is increasingly considered as essential in numerical modeling of TCs (e.g., [16–19]). Coupled OWA models (e.g., [19–23]) have started being developed to deal with the significant role of oceanic waves in air–sea exchanges. Waves modify the wind stress which drives the turbulent fluxes, and the turbulent mixing induced by non-breaking waves is essential to improve the cooling effect underneath and then TC forecasting [24]. Moreover, breaking waves generate sea sprays [25] that can impact TC structure and intensity in several ways. These sea sprays can modify the heat and momentum air–sea fluxes [26–28] even if the quantification of the sea spray effect on heat and momentum fluxes is still debated [29]. Sea spray particles are also a source of cloud condensation nuclei [30–32], which can modify the microphysical structure and latent heat budget of the TC and consequently its structure and intensity [33]. Moreover, cloud-radiative processes in ice clouds are increasingly

recognized to play a major role in the development of TCs (e.g., [34,35]) due to their impact on the secondary circulation. Since convective precipitation and cloud microphysics remain one major cause of systematic errors in numerical models across time scales [36], aerosol–microphysics–radiation interactions must be carefully considered in numerical models to improve TC forecasting.

2.1. Ocean–Wave–Atmosphere Coupling

The coupled system presented herein (Figure 1) is based on a combination of state-of-the-art numerical models for the atmosphere and the surface, the waves, and the ocean.

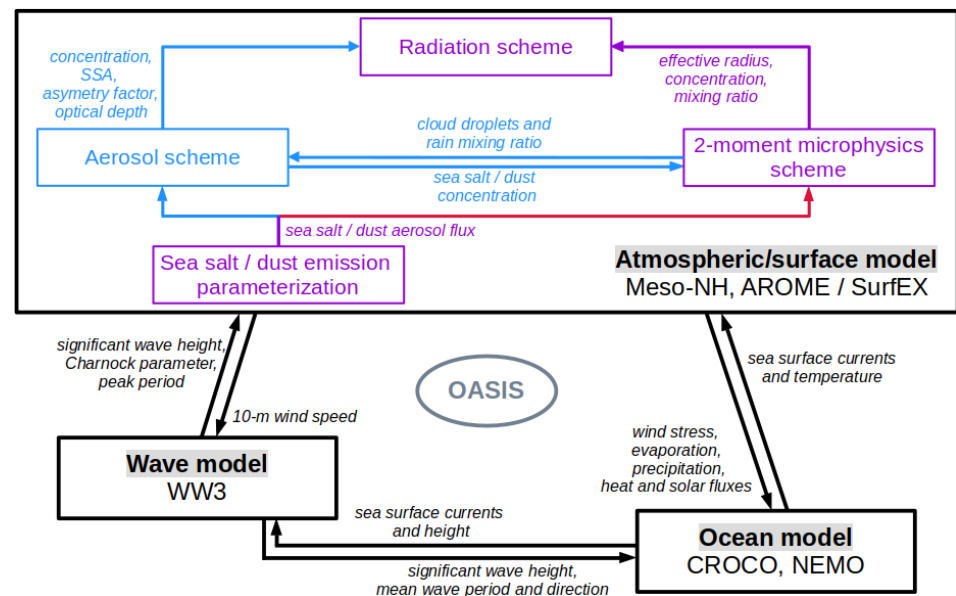


Figure 1. Schematic diagram of the coupling systems in TC numerical modeling. The OWA coupling is shown in black while the coupling inside the atmosphere/surface model is shown with blue, red, and purple colors. Fields exchanged among the atmospheric, wave, and oceanic models are shown in italic black; they are exchanged at intervals defined by the user (typically ~ 10 min). Fields exchanged among the atmospheric schemes are shown in italic blue and purple; they are exchanged at each time step. In the atmospheric/surface model, the purple color shows schemes, fields, and exchanges that are common to the AROME and Meso-NH models. The schemes, fields, and exchanges that are specific to the Meso-NH model are shown with blue color. The exchanges specific to the AROME model are shown with red color. Adapted from Tulet et al. [14].

2.1.1. Atmospheric Models

For the atmosphere, the Meso-NH research model (<http://mesonh.aero.obs-mip.fr/>, accessed on 27 May 2021) [37] or the AROME French operational model [38,39] can be used. Meso-NH is the non-hydrostatic mesoscale atmospheric model of the French research community. It incorporates a non-hydrostatic system of equations that enables dealing with a large range of scales (from synoptic to large eddy). It has a complete set of modules and parameterizations for the representation of clouds and precipitation, aerosol, and chemistry but also fires, volcanic eruptions, and atmospheric electricity [37]. Meso-NH is designed to perform both real case simulations and academic cases. It also has a complete set of observation operators to compare model output directly with observations (radar, lidar, GPS, satellites).

AROME is a kilometer-scale NWP model operational at Météo-France [38]. While the dynamic core comes from ALADIN [40], the main physical parameterizations mostly come from Meso-NH. Over the SWIO, AROME operates with a 2.5 km grid mesh over a 1600×900 points domain and 90 stretched vertical levels. In its operational version, it is coupled to a 1D ocean mixed layer model [41], and at initialization, an Analysis Incremental Update (IUA) scheme [42] is used to combine ECMWF large-scale analysis and AROME-OI

forecast in order to reduce spin up time [39]. In its research version, it can be equipped with a 3D-Var assimilation scheme and it has the capability to be coupled to a full 3D ocean. Herein, the AROME model is used in its research version, but the 3D-Var data assimilation scheme is not used. AROME is initialized and forced at the lateral boundaries by the ECMWF/IFS analysis.

2.1.2. Surface Model

Both Meso-NH and AROME are coupled to the SurfEx externalized surface model (<https://www.umr-cnrm.fr/surfex/>, accessed on 27 May 2021) [43] to represent surface-atmosphere interactions through different surface types. Four types of surface are considered: vegetation (Interactions between Soil, Biosphere and Atmosphere scheme) [44] and city (Town Energy Budget scheme) [45], lake (Freshwater Lake model) [46], and ocean. Ocean-atmosphere exchanges are represented by the classical turbulent surface fluxes parameterizations [47,48]. In these “bulk” parameterizations, the ocean is represented by sea surface temperature (SST) and surface currents. The recent development of the coupling between SurfEx and a 1D oceanic mixed boundary layer model [41,49] and especially with a 3D ocean model [50] has allowed for the improvement of the representation of the ocean in these parameterizations. Indeed, the ocean-atmosphere feedback is now considered via the evolution of SST and currents in agreement with atmospheric dynamics.

2.1.3. Ocean Models

For the ocean, either the CROCO (Coastal and Regional Ocean COmmunity model; <http://www.croco-ocean.org>, accessed on 27 May 2021) or the NEMO (Nucleus for European Modelling of the Ocean; <https://www.nemo-ocean.eu/>, accessed on 27 May 2021) [51] model can be used. CROCO is a new community oceanic modeling system built upon the dynamical core of ROMS_AGRIF [52,53] which has been used in massively parallel simulations (e.g., [54]). CROCO is able to resolve very fine scales (especially in the coastal area) and their interactions with larger scales. It includes a lot of capabilities such as non-hydrostatic kernel, OWA coupling, sediment transport, high-order numerical schemes for advection and mixing, a dedicated I/O server (XIOS), online diagnostics, and options for coastal configurations.

NEMO [51] is a modeling framework for oceanic research and forecasting whose development is supported by a European consortium (CMCC and INGV, Italy; CNRS and Mercator Océan, France; Met Office and NERC, UK). NEMO includes major ocean related components: ocean dynamics and thermodynamics (blue ocean), sea-ice dynamics and thermodynamics (white ocean), biochemical processes, and oceanic tracers transport (green ocean). It is intended to be a flexible tool for studying the ocean and its interactions with the other components of the Earth climate system over a wide range of space and time scales.

2.1.4. Wave Model

The wave evolution is modeled using the WaveWatch III (WW3) model (<http://polar.ncep.noaa.gov/waves/wavewatch/>, accessed on 27 May 2021) [55] that includes the latest scientific advances in the field of wind-wave modeling and dynamics. It solves the random phase spectral action density balance equation for wavenumber-direction spectra. Propagation of a wave spectrum can be solved using regular (rectilinear or curvilinear) and unstructured (triangular) grids, individually or combined into multi-grid mosaics. Physical processes considered in this model include parameterizations for wave growth due to the actions of wind, nonlinear resonant wave-wave interactions, scattering due to wave-bottom interactions, and dissipation due to whitecapping and bottom friction. All these processes and numerical aspects allow for the resolution of the sea state ranging from deep to shallow waters which is essential for storm surges applications, in global or coastal domains.

2.1.5. Ocean–Wave–Atmosphere Coupling

The coupling among the ocean, wave, and atmosphere models is realized through the OASIS coupler (<https://portal.enes.org/oasis>, accessed on 27 May 2021) [56]. The ocean model sends information about the sea surface temperature and currents to the atmospheric model and about the sea surface currents and height to the wave model. The atmospheric model sends its 10-m wind field to the wave model while the wind stress, evaporation, precipitation, heat, and solar fluxes are sent to the ocean model. Finally, the wave model sends the Charnock parameter, the peak period, and the significant wave height to the atmospheric model and the significant wave height, mean wave period, and direction to the ocean model. A detailed technical description of the OWA coupling can be found in Voltaire et al. [50] and Pianezze et al. [23], and additional details on the recent NEMO-WW3 coupling can be found in Couvelard et al. [57]. Several configurations of this coupled system are presented in Section 3.

2.2. Coherent Parameterizations for Tropical Cyclone Modeling

In the framework of this program, considerable attention has been paid to the development of the aerosol–microphysics–radiation interactions in tropical storms. The OWA coupled system described in Section 2.1 enables the use of variables from another compartment of the coupled system but coherently computed with respect to the two other compartments. For example, the OWA system enables the computation of sea salt aerosols emission in the SurfEx surface model using the wind field from the atmospheric model, the sea surface temperature and salinity from the ocean model, and the significant wave height from the wave model. If a wave model is not considered and coupled inline, the significant wave height must be interpolated from an external model (offline simulation of a wave model, interpolation from ECMWF analysis, or prescription of a constant value). However, it can lead to sea spray particles spatial distribution incoherent with the wind and wave fields [23].

In the SurfEx model, a sea salt aerosol emission parameterization [58] has been introduced. If the Meso-NH atmospheric model is used, these particles are implemented in the ORILAM aerosol scheme [59,60] and experience transport by advection, sedimentation and turbulence, and dry or wet deposition. These aerosols can serve as cloud condensation nuclei (CCN) thanks to the coupling between the ORILAM aerosol scheme and the LIMA 2-moment microphysics scheme [33,61]. The relatively high computational cost of the aerosol scheme prevents it from being implemented in an operational model such as AROME. Therefore, if the AROME atmospheric model is used, the sea salt aerosols emitted in the SurfEx model are directly coupled with the LIMA microphysics scheme. The direct implementation of sea salt aerosols into the 2-moment microphysics scheme does not allow for the consideration of a complex dimensional distribution, the atmospheric formation of new particles (nucleation), and the aging of aerosols (coagulation, gas-particles interactions), but their spatial distribution coherent with the wind and wave fields is preserved.

Additional developments related to ice microphysics are also going on. Several prognostic variables representing different ice crystal habits have been implemented in LIMA to better represent the diversity of ice crystal properties in clouds and cloud-radiation interactions. Two crystal habits are considered to represent the primary habits (columns and plates) formed between 0 and -20 °C. Two additional variables are necessary to represent the transition between primary habits [62] and the polycrystals generally encountered at temperatures below -20 °C [63]. Different coefficients of the mass-diameter and fall speed-diameter relationships and of the capacitance are attributed to each ice crystal variable, and microphysical processes are computed accordingly. In each grid mesh, the ice crystal effective radius is computed from the prevailing ice crystal habits in terms of number concentration and is passed to the radiation scheme (Figure 1). This enables a consistent treatment of the aerosol–microphysics–radiation interactions in clouds.

3. Some Examples of Coupled Ocean–Atmosphere Modeling of TCs in the SWIO

The coupled system described in Section 2 has been used to simulate several TCs that evolved in the SWIO with the aim to progress on the physical processes involved in TC development and intensification and to produce realistic wind, precipitation, and swell fields over the SWIO territories. The objective of this section is to illustrate the OWA coupled system and its modularity and the consistence of the models and physical parameterizations. Several observational data obtained in the framework of the RNR-CYC program [15] are used to validate the coupled model. The best-track database from RSMC La Réunion is used to evaluate the track and intensity of each modelled TC. In the SWIO, the maximum wind speed (V_{MAX}) used to classify the storm intensity is calculated over a 10-min period. When V_{MAX} is between 14 and 16 m s⁻¹, a storm is called a Tropical Depression (TD). Although it has not been given a name at this stage, it is registered in operational TC databases and starts to be tracked by RSMC La Réunion. A storm is given a name when it reaches the stage of Moderate Tropical Storm (MTS, $V_{MAX} \geq 17$ m s⁻¹), which is generally considered as the time corresponding to the completion of the cyclogenesis. Storms reaching MTS intensity, hereafter referred to as Cyclogenetic Storms (CS), are classified into four more categories according to their lifetime maximum intensity (LMI): Strong Tropical Storms (STS, $28 \leq V_{MAX} \leq 32$ m s⁻¹), Tropical Cyclones (TC, $33 \leq V_{MAX} \leq 45$ m s⁻¹), Intense Tropical Cyclones (ITC, $46 \leq V_{MAX} \leq 59$ m s⁻¹), and Very Intense Tropical Cyclones (VITC, $V_{MAX} > 60$ m s⁻¹).

3.1. Numerical Setup of the Simulations

In this section, we define the basic configuration of each model used in the coupled modeling platform. The model configuration for each simulation is summarized in Table 1.

Table 1. Summary of the models used in the coupled simulations. The domain size and horizontal grid spacing (Δx) used for each model and each TC is indicated. If two nested domains are used (as for Dumile), D1 and D2 represent the outer and inner domains, respectively. COARE, ECUME6, and WASP refer to the air–sea flux parameterizations of Fairall et al. [47], Belamari [48] and Sauvage et al. [64], respectively. For the microphysics, ICE3 and LIMA mean that the 1-moment microphysics ICE3 scheme [65] and the ORILAM-LIMA coupling [33] are used, respectively.

Tropical Cyclone	Domains		Atmosphere		Surface	Wave	Ocean	Duration
	nb of Points	Δx	Model	Microphysics	OA Flux			
Dumile (2013) [33]	D1: 450 × 450 D2: 400 × 584	8 km 2 km	Meso-NH	LIMA	COARE	-	-	51 h
Bejisa (2014) [23]	600 × 500	2 km	Meso-NH	ICE3	COARE	WW3	CROCO	42 h
Bejisa (2014) [66]	600 × 500	2 km	Meso-NH	ICE3	ECUME6	-	NEMO	42 h
Bejisa (2014) [67]	1000 × 800	3 km	Meso-NH	ICE3	COARE	-	CROCO	120 h
Fantala (2016)	1250 × 750	2 km	Meso-NH	ICE3	COARE	WW3	CROCO	240 h
Herold (2019)	1600 × 900	2.5 km	AROME	ICE3	ECUME6	-	NEMO	4 × 48 h
Idai (2019)	750 × 800	2 km	Meso-NH	LIMA	WASP	WW3	CROCO	96 h

For the Meso-NH atmospheric model, a single domain with 2 km horizontal grid spacing is used. Seventy vertical levels are specified with increased resolution in the lower levels. Several options for microphysics are available in Meso-NH. Herein, two parameterizations are used (see Table 1): the microphysics is described by the 1-moment bulk microphysics scheme called ICE3 [65] predicting the mixing ratio of cloud droplets, raindrops, pristine ice, snow/aggregates, and graupel or by the 2-moment microphysics scheme LIMA coupled to the ORILAM aerosol scheme as described in Section 2.2. The turbulence parameterization is based on a 1.5 order closure [68] with vertical turbulent flux computations and using the mixing length of Bougeault and Lacarrere [69]. A shallow convection scheme is used based on mass-flux computations [70]. The ECMWF radiative scheme [71] including the Rapid Radiative Transfer Model (RRTM) parameterization [72] is used. The initial and lateral boundary conditions are specified by the 6-hour ECMWF/IFS operational analysis (<https://www.ecmwf.int/>, accessed on 27 May 2021). If the ORILAM-LIMA coupling is used, aerosol analysis from CAMS (<https://atmosphere.copernicus.eu/>,

accessed on 27 May 2021) [73] are used as initial and boundary conditions of the aerosol and microphysics schemes in Meso-NH [33].

For the AROME atmospheric model, a single domain with 2.5 km horizontal grid spacing is used. Ninety vertical stretched levels are specified with the first level at 5 m and the top of the model at 10 hPa. The initial and lateral boundary conditions are taken from hourly ECMWF/IFS operational forecasts. The physical parameterizations used herein are the ones used in AROME-France as specified in Seity et al. [38], including the 1-moment microphysics scheme ICE3 [65] and the ECUME (Exchange Coefficients from Unified Multi-campaigns Estimates) parameterization for air–sea fluxes [48].

The SurfEx surface model has the same horizontal resolution and number of points as the atmospheric model (Meso-NH or AROME). It is initialized by the ECMWF/IFS operational analysis. The land–atmosphere interaction scheme ISBA [44] is used. Several parameterizations for sea surface exchanges are available in SurfEx [47,48,64,74,75]; the parameterization used in each simulation is indicated in Table 1.

The grid covered by WW3 is the same as that of the atmospheric model with a horizontal grid spacing of 2 km. The global time step is 100 s. The spectral discretization of WW3 is 24 for the direction and 32 for the frequency. For the present study, the third-order Ultimate Quickest scheme [76] with the Garden Sprinkler correction was used to avoid this numerical artifact due to the discrete directions of wave propagation. The wind–wave interaction source term of Ardhuin et al. [77] was used. This parameterization is built around a saturation-based dissipation, reducing the unrealistically large drag coefficients under high winds. Nonlinear wave–wave interactions were modeled using the Discrete Interaction Approximation (DIA) [78]. Additionally, depth-induced wave breaking [79] and bottom friction source terms [80] were used. In order to allow the downscaling from the global “Modélisation et Analyse pour la Recherche Côtière” analyses (MARC; <http://marc.ifremer.fr/>, accessed on 27 May 2021), a 7-day simulation with the wave model alone is performed before the fully coupled simulation.

The domain for the CROCO oceanic model is the same as the atmospheric and wave models with horizontal grid spacing of 2 km. The domain consists of 32 vertical levels with increased resolution near the surface. A “time-splitting” scheme is used with baroclinic and barotropic time steps of 100 s and 2 s, respectively. The advection scheme is third-order upstream biased [81]. Subgrid-scale vertical mixing is solved by the nonlocal K-profile parameterization scheme [82]. The model is initialized and forced at the lateral boundaries every day with global analyses ($1/12^\circ$) provided by Mercator Ocean (<https://www.mercator-ocean.fr/en/>, accessed on 27 May 2021).

The domain for the NEMO oceanic model is the same as for the atmospheric domain with horizontal grid spacing of $1/12^\circ$ (about 9 km) and 50 unevenly spaced vertical levels. A time step of 360 s is used for the dynamic. The vertical mixing is a turbulent kinetic energy closure scheme based on Gaspar et al. [49] and modified by Madec et al. [83]. The split-explicit free surface formulation follows the one proposed by Shchepetkin and McWilliams [52]. In the same way as CROCO, NEMO is initialized and forced at the lateral boundaries every day with the global analyses from Mercator Ocean global model PSY4 [84].

3.2. Modeling Studies of Tropical Cyclones Dumile (2013) and Bejisa (2014)

Several parts of the modeling platform have been independently evaluated in the last few years. These published studies are not detailed hereinafter but a short statement of the main findings is given in this section.

A first evaluation of the aerosol–microphysics coupling was performed through the simulation of TC Dumile (2013) [33] that impacted La Réunion in January 2013. The importance of explicitly taking into account sea salt aerosol emissions associated with high winds and waves in TCs was shown to be a critical point for simulating the track, intensity, and structure of long-lasting systems that need to generate their own CCN.

Several modeling studies of TC Bejisa that passed in the neighborhood of La Réunion in January 2014 have been performed with the modeling platform described in Section 2.

Using the Meso-NH/WW3/CROCO coupled system, Pianezze et al. [23] showed that on-line coupling with a wave model is important to obtain a spatiotemporal and size distribution of sea salt aerosol particles coherent with the wind and sea state fields. Bielli et al. [66] evaluated the sensitivity of Bejisa simulation to the degree of ocean–atmosphere coupling. They showed that using a 1D coupling (Meso-NH coupled to a 1D ocean mixed layer model) does not enable to reproduce the intensity and structure of surface ocean cooling compared to composite observations, while a 3D coupled model (Meso-NH coupled to the 3D NEMO model) does. Finally, an ocean–atmosphere configuration with km-scale grid spacing was implemented to investigate how the characteristics of a typical TC like Bejisa would evolve in the context of climate change [67]. The pseudo global warming method was used to construct future environments: perturbations computed from six Coupled Model Intercomparison Project 5 (CMIP5) climate models were added to historical analyses from ECMWF. This high resolution study complements the climate projections at the basin scale realized in the framework of RNR-CYC program and described in Section 4.

3.3. Tropical Cyclone Fantala (2016)

Fantala (2016) is the second most intense TC ever observed in the SWIO with 10-min sustained wind speed reaching 69 m s^{-1} on 17 April 2016 at 18 UTC. Fantala moved over and devastated the Farquhar group of Seychelles on 17 April with wind gusts estimated at 96 m s^{-1} . Fantala exhibits a very unusual track turning back twice during its 16 days lifecycle (Figure 2). This uncommon track makes Fantala a perfect candidate to evaluate the impact of air–sea flux parameterization on the storm development.

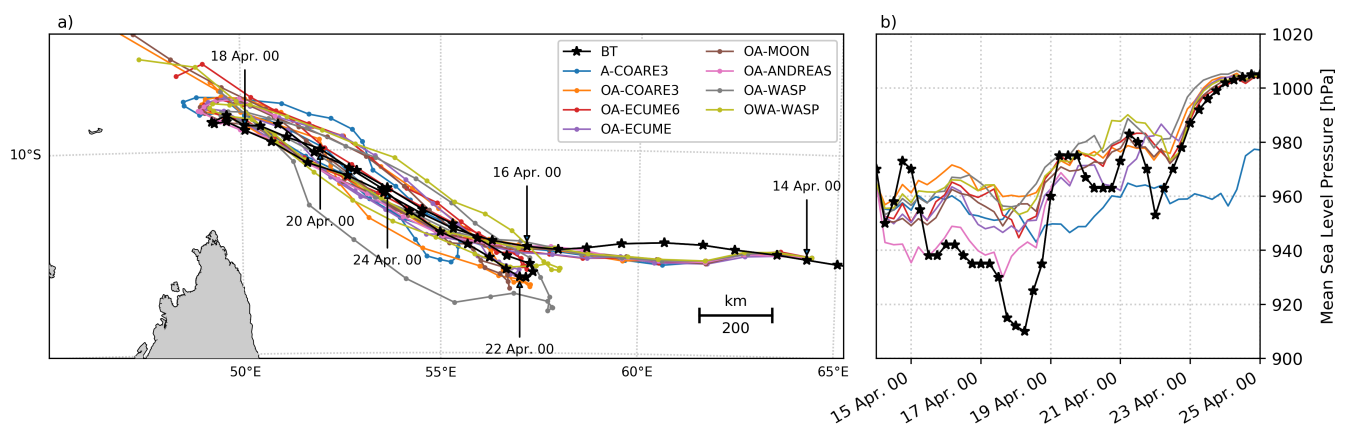


Figure 2. (a) Track and (b) intensity defined by the minimum sea level pressure (MSLP, hPa) of TC Fantala between 14 March 2016 00 UTC and 25 March 2016 00 UTC. The best-track is plotted with black lines and stars. The colored lines correspond to the different simulations summarized in Table 2.

The simulation of TC Fantala was performed with Meso-NH/SurfEx, WW3, and CROCO on a single domain located between 44.54° E and 67.64° E and between 17.66° S and 4.18° S (Table 1). The simulation starts on 14 April 2016 00 UTC and lasts 240 h encompassing the two U-turns of Fantala. The simulation matches the basic configuration described in Section 3.1, but several additional simulations have been performed to investigate the impact of air–sea flux on the evolution of this system. These simulations differ by the degree of OWA coupling and the air–sea flux parameterization (Table 2).

Table 2. Summary of the simulations of TC Fantala. A, OA, and OWA stand for Atmosphere, Ocean–Atmosphere, and Ocean–Wave–Atmosphere simulations, respectively.

Simulation	Meso-NH/SurfEx	WW3	CROCO	Air–Sea Flux Param.
A-COARE3	X	-	-	COARE3 [47]
OA-COARE3	X	-	X	COARE3 [47]
OA-ECUME	X	-	X	ECUME [48]
OA-ECUME6	X	-	X	ECUME6 [48]
OA-MOON	X	-	X	MOON [74]
OA-ANDREAS	X	-	X	ANDREAS [75]
OA-WASP	X	-	X	WASP [64]
OWA-WASP	X	X	X	WASP [64]

Six different air–sea flux parameterizations available in SurfEx have been tested in this study and are basically described hereinafter. The COARE3.0 parameterization [47] is derived from COARE2.6 [85] which was developed from observations of the TOGA-COARE field campaign [86] in the North Pacific. An important update of COARE3.0 is the new formulation of the roughness length that increases when the wind speed exceeds 10 m s^{-1} . However, this parameterization is mainly valid for wind speeds lower than 20 m s^{-1} due to the lack of observations for high wind conditions. The wave effect is considered through the roughness length [87]. The WASP (Wave Age Stress dependant Parameterization) parameterization [64] is based on the COARE3.0 parameterization but the roughness length computation has been modified to consider the sea state. Since different mechanisms are involved at weak ($<5 \text{ m s}^{-1}$), moderate ($5\text{--}20 \text{ m s}^{-1}$), and high ($>20 \text{ m s}^{-1}$) wind speeds, a piecewise continuous description is adopted to describe the Charnock parameter. It enables the representation of the observed decrease of the drag coefficient in strong wind conditions. The ECUME and ECUME6 parameterizations [48] are built upon in-situ air–sea fluxes from different field campaigns. While ECUME is tailored for low to moderate winds, high wind conditions are considered in ECUME6. The turbulent exchange coefficients are computed directly from observations which makes the wave impossible to consider in the roughness length computation. The ANDREAS parameterization [75] is the only parameterization that intends to take into account the effect of sea sprays on sensible and latent heat fluxes through their evaporation in the atmospheric boundary layer. However, this parameterization only uses data up to wind speed of 25 m s^{-1} . Finally, the MOON parameterization [74] is based on wind–wave coupled numerical simulations of ten TCs. A new expression of the roughness length has been derived that limits its increase as soon as the wind speed exceeds 12.5 m s^{-1} .

Whatever the parameterization of air–sea flux used, the simulated tracks are close to the best-track (Figure 2). As soon as the ocean–atmosphere coupling is activated, the position of the U-turns is well simulated, whether in terms of timing (less than 2 h and 6 h deviation from the best-track for the first and second U-turns, respectively) or in terms of position (less than 20 km and 100 km for the first and second U-turns compared to the best-track). The choice of the air–sea flux parameterization has then little impact on the simulated track. This confirms that Fantala’s track is mainly determined by large-scale flow. Nevertheless, after the second U-turn, the coupled ocean–atmosphere simulation with WASP parameterization (OA-WASP, grey line in Figure 2a) differs from the others. The wave field used for this parameterization is a function of the 10-m wind only and is not realistic in this simulation: the coupling with a wave model is necessary if this parameterization is used as shown by the green line in Figure 2 (OWA-WASP). It must also be noted that in case of the atmosphere-only simulation (A-COARE3, blue line in Figure 2a), the position of the first U-turn differs by more than 6 h and 100 km from the timing and position analyzed in the best-track.

Concerning the intensity of the modeled TC (Figure 2b), the choice of the air–sea flux parameterization can have a significant impact. The forced simulation (A-COARE3, blue line) produces a system that remains too intense compared to the best-track despite the two U-turns. It is clear that the A-COARE3 simulation is not able to capture the storm

weakening (between 18 April 06 UTC and 19 April 00 UTC) after the first U-turn unlike the other simulations that use an ocean–atmosphere coupled model. This is explained by the absence of cooling under the cyclone. This simulation is a perfect example of the need for ocean–atmosphere coupling to correctly simulate the evolution of TC intensity. Apart from the forced simulation, the other simulations capture the overall trend of intensity variation even if they are not able to reproduce the maximum intensity on 18 April (910 hPa). The OA-ANDREAS simulation (pink line) produces the most intense system, and the closest to the best-track, during the first five days. The other simulations remain relatively close with differences of up to 30% with the best-track.

To quantify the effect of these parameterizations on turbulent fluxes and indirectly on TC intensity, the momentum fluxes, the drag coefficient (C_d), and the latent and sensible heat fluxes as a function of the 10-m wind speed are shown on Figure 3 when Fantala reaches its maximum intensity (18 April 2016 at 00 UTC), before its first U-turn. The four parameters show variability for a given 10-m wind speed: this is explained by the effect of the stability of the atmosphere and waves on the turbulent fluxes which varies from one grid point to another.

For the momentum flux (Figure 3a) and the drag coefficient (Figure 3b), all simulations show a similar average value up to 10-m wind speed $\sim 30 \text{ m s}^{-1}$, which corresponds to the domain of validity of these parameterizations. From 30 m s^{-1} , the average values of the momentum flux and of the drag coefficient start to diverge depending on which parameterization is used. The COARE3.0 parameterization (blue and orange dots and segments) has a drag coefficient that increases with the 10-m wind speed ($C_d = 2.6$ and 3.0 for 10-m wind speed of 40 and 50 m s^{-1} , respectively) and produces the strongest momentum fluxes ($8.5 \text{ m}^2 \text{ s}^{-2}$ for 10-m wind speed of 50 m s^{-1}). Observations under strong wind conditions show a saturation of the drag coefficient and even a decrease when the wind speed exceeds 40 m s^{-1} [88]. As expected, the COARE3.0 parameterization does not behave realistically in strong wind conditions. It must be noted that the ocean–atmosphere coupling (OA-COARE3) tends to slightly reduce the momentum flux and the drag coefficients for wind speeds above 37.5 m s^{-1} when compared to the atmosphere only simulation (A-COARE3). The five other parameterizations reproduce the saturation of the drag coefficient. WASP shows the lowest momentum flux and drag coefficient for wind speeds above 30 m s^{-1} : the momentum flux does not exceed $4.5 \text{ m}^2 \text{ s}^{-2}$ on average for 10-m wind speed of 50 m s^{-1} , while the drag coefficient reaches a mean minimum of 1.5 for 10-m wind speed of 45 m s^{-1} . The MOON and ANDREAS parameterizations are relatively close in strong wind conditions. For 10-m wind speed of 40 m s^{-1} , the drag coefficient does not exceed 2.35 and 2.1 for ANDREAS (pink dots and segments) and MOON (maroon dots and segments), respectively. The ECUME (purple dots and segments) and ECUME6 (red dots and segments) parameterizations show relatively similar behavior in strong winds, with a decrease of the drag coefficient. For 10-m wind speed of 40 m s^{-1} , the drag coefficient is about 1.65 for these two parameterizations. It thus produces the lowest momentum flux in high wind conditions ($\sim 3.7 \text{ m}^2 \text{ s}^{-2}$ for 10-m wind speed of 50 m s^{-1}), more than half of the momentum flux encountered in the A-COARE3 simulation. However, the ECUME and ECUME6 parameterizations do not allow for the representation of the waves in the drag coefficient, while this coefficient has been shown to vary depending on the wave's age [87].

The sensible and latent heat fluxes simulated with the different parameterizations show very large differences for 10-m wind speeds higher than 20 m s^{-1} (Figure 3c,d). In OA-ANDREAS, both the latent and sensible heat fluxes show large standard deviation (for example, for a 10-m wind speed of 40 m s^{-1} , the latent and sensible heat fluxes are $500 \pm 650 \text{ W m}^{-2}$ and $-100 \pm 270 \text{ W m}^{-2}$, respectively). The latent heat fluxes in OA-ANDREAS are located in the middle of all the latent heat fluxes simulated by the other parameterizations, while the sensible heat fluxes are the lowest with negative mean values for 10-m wind speed higher than 30 m s^{-1} . As for the momentum flux, the A-COARE3 simulation exhibits the largest sensible and latent heat flux with mean values reaching 1000 and 200 W m^{-2} , respectively, for 10-m wind speeds of 40 m s^{-1} . For 10-m wind speeds of

40 m s^{-1} , the coupling with a 3D ocean model reduces dramatically the sensible and latent heat flux (500 and 40 W m^{-2} , respectively, in OA-COARE3). The other simulations exhibit a similar behavior in terms of heat fluxes, except OA-ECUME that diverges from the other simulations (OA-ECUME6, OA-MOON, OA-WASP, OWA-WASP) for wind speeds higher than 45 m s^{-1} and behaves like OA-COARE3.

As already shown (e.g., [89]), the choice of the air–sea flux parameterization affects the intensity of the cyclone. However, in the case of TC Fantala, the effect of 3D coupling with the ocean has more impact on the intensity after the first U-turn while the choice of the air–sea flux parameterization is essential before the first U-turn. A more advanced analysis is going on to fully understand the air–sea interactions in this complex TC.

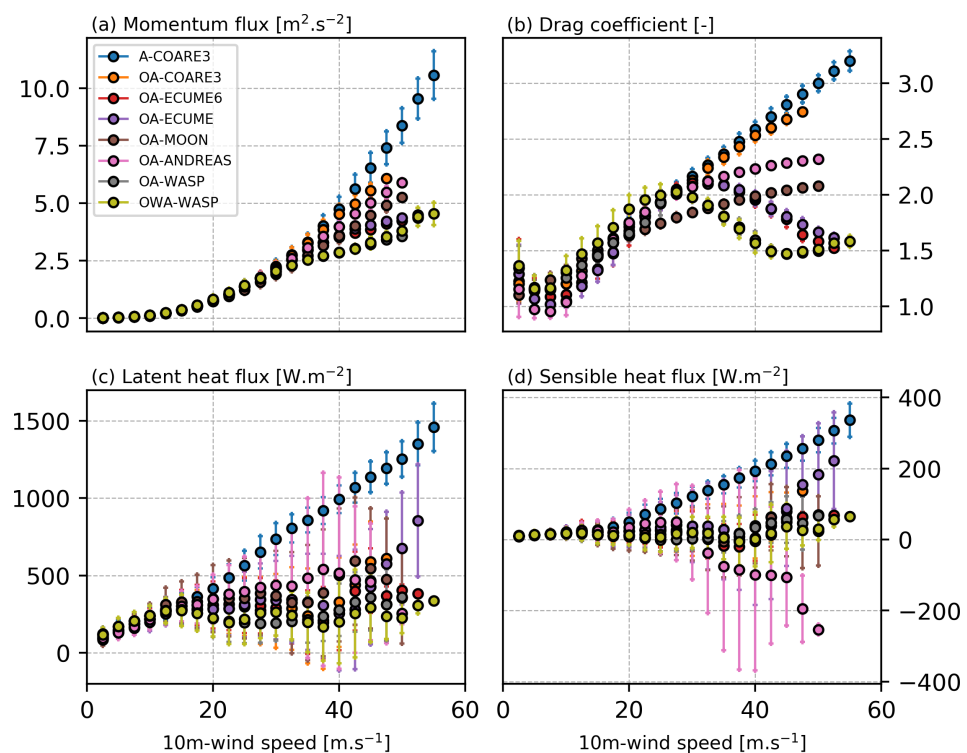


Figure 3. (a) Momentum flux ($\text{m}^2 \text{ s}^{-2}$), (b) drag coefficient, (c) latent heat flux (W m^{-2}), and (d) sensible heat flux (W m^{-2}) vs. 10-m wind speed (m s^{-1}). These pairs of values are extracted at each grid point over the whole domain on 18 April at 00 UTC when TC Fantala is at its maximum intensity. The average (colored dot) and standard deviation (colored segments) of each parameter are plotted for each parameterization every 2.5 m s^{-1} .

3.4. Tropical Cyclone Idai (2019)

In order to demonstrate the importance of consistently considering atmospheric, oceanic, and wave parameters, the OWA coupled system was used to forecast the intense tropical cyclone Idai (2019). TC Idai landed on the region of Beira (Mozambique) on 15 March 2019 (Figure 4a). TC Idai developed during the 2019 regional field campaign and was captured by the Sentinel 1A / 1B acquisitions. The simulation of TC Idai was performed with Meso-NH, WW3, and CROCO on a single domain covering the Mozambique Channel (Table 1). The aerosol–microphysics–radiation interaction described in Section 2.2 is used herein. Aerosol analysis from CAMS (<https://atmosphere.copernicus.eu/> accessed on 27 May 2021) [73] are used as initial and boundary conditions of the aerosol and microphysics schemes in Meso-NH as described in Hoarau et al. [33]. The simulation starts on 11 March 2019 00 UTC and lasts 96 h, until TC Idai makes landfall in the region of Beira.

Figure 4 shows the track and intensity of TC Idai as analyzed in the RSMC La Réunion best-track and simulated by Meso-NH/WW3/CROCO. The modeled track matches very well the best-track during the first 48 h (Figure 4a). On 13 March at 00 UTC, the cyclone in

the model starts to accelerate which causes a landfall occurring 6 h in advance compared to the best-track. Despite a 7 hPa underestimation at the initial state, the model manages to represent the overall intensity tendency during the first 42 h (Figure 4b). Idai experienced an eyewall replacement cycle on 12 and 13 March which is not captured by the model leading to an overestimation of the intensity. On 14 March at 00 UTC, Idai reached a maximum of intensity (940 hPa) rather well reproduced by the model (948 hPa). During the last 12 h of the simulation, the intensity collapses due to the 6-hour delay in landfall.

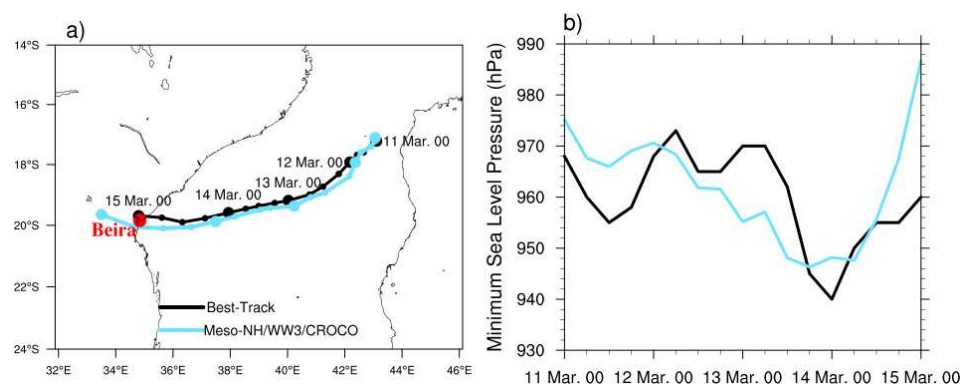


Figure 4. (a) Track and, (b) intensity defined by the MSLP (hPa) of TC Idai between 11 March 00 UTC and 15 March 00 UTC. The best-track and the Meso-NH/WW3/CROCO simulations are shown as black and cyan lines, respectively. The city of Beira is displayed with a red circle.

Figure 5 shows horizontal cross sections of TC Idai on 12 March 2019 at 18 UTC simulated by the OWA system. At this date, Idai moves to the west, and its intensity is analyzed at 966 hPa by RSMC La Réunion vs. 962 hPa for the modeled TC. The 10-m wind speed (Figure 5a) exceeds 40 m s^{-1} all around the eyewall and exhibits two maxima (45 m s^{-1}) at the south-western and at the north-eastern sides of the system. The significant wave height (H_S) exceeds 8 m all over the eyewall. Its maximum (10.5 m) is located in the southeastern region of the cyclone (i.e., in the right-front area relative to the cyclone track). H_S values higher than 6 m extend over more than 300 km from the center of the cyclone, i.e., over the most part of the Mozambique channel. The strong surface winds and the high H_S are the main parameters involved in the emission of sea salts aerosols. Sea salt aerosol mass flux higher than $10 \mu\text{g m}^{-2} \text{ s}^{-1}$ is found in the eyewall at 20 m above sea level (asl) (Figure 5b). Values higher than $12 \mu\text{g m}^{-2} \text{ s}^{-1}$ are located in the southern part of the eyewall where the maximum wind speed and wave height are encountered. The sea salt aerosol mass flux remains significant ($>1 \mu\text{g m}^{-2} \text{ s}^{-1}$) in the region where the 10-m wind speed and H_S exceeds 10 m s^{-1} and 6 m, respectively. These values are probably underestimated since the parameterization of sea salt emission used in SurfEx [58] mainly considers the generation of submicronic sea salt particles. Supermicron particles are also generated but there are large uncertainties concerning their generation function (see Figure 6 in [90]). However, due to their large size, even if their number concentration is low, their contribution to the mass flux is important. In the ORILAM aerosol scheme, sea salt aerosols with dry diameter greater than 80 nm represent the CCN concentration reported in Figure 5. At 3000 m asl, high number concentration (between 30 and 125 cm^{-3}) of available CCN is modeled in the inner core of the system (Figure 5c). These concentrations are strongly inhomogeneous due to the balance between the sea salt aerosol emission, the vertical transport, and the precipitation scavenging that occurs within the convective cells. Maximum values of activated CCN ($\sim 10 \text{ cm}^{-3}$) are found in the eyewall at this altitude. During the 2-month field campaign, the Boreal unmanned airborne system equipped with meteorological, aerosol, sea state, and turbulence instruments, made several flights in a large area around La Réunion [15]. Boreal measurements showed aerosol concentrations (diameter $> 0.3 \mu\text{m}$) in the range $50\text{--}150 \text{ cm}^{-3}$, increasing with wind speed and wave height (see Figure 16 in [15]). This range of aerosol concentrations was sampled for wind

speed between 2.2 and 13.5 m s^{-1} , wave height between 2 and 3.7 m, and below 200 m asl. At 60 m asl, the coupled simulation displays available CCN concentrations between 100 and 150 cm^{-3} in the region with wind speed $\sim 13 \text{ m s}^{-1}$ and wave height $\sim 3.5 \text{ m}$ (not shown) which is comparable to observed values. The total ice thickness is higher than 9 mm in the south-western and north-eastern part of the eyewall (Figure 5d). Instantaneous precipitation higher than 10 mm h^{-1} is found collocated with the high value of total ice thickness in the eyewall, showing ice phase precipitation in this region.

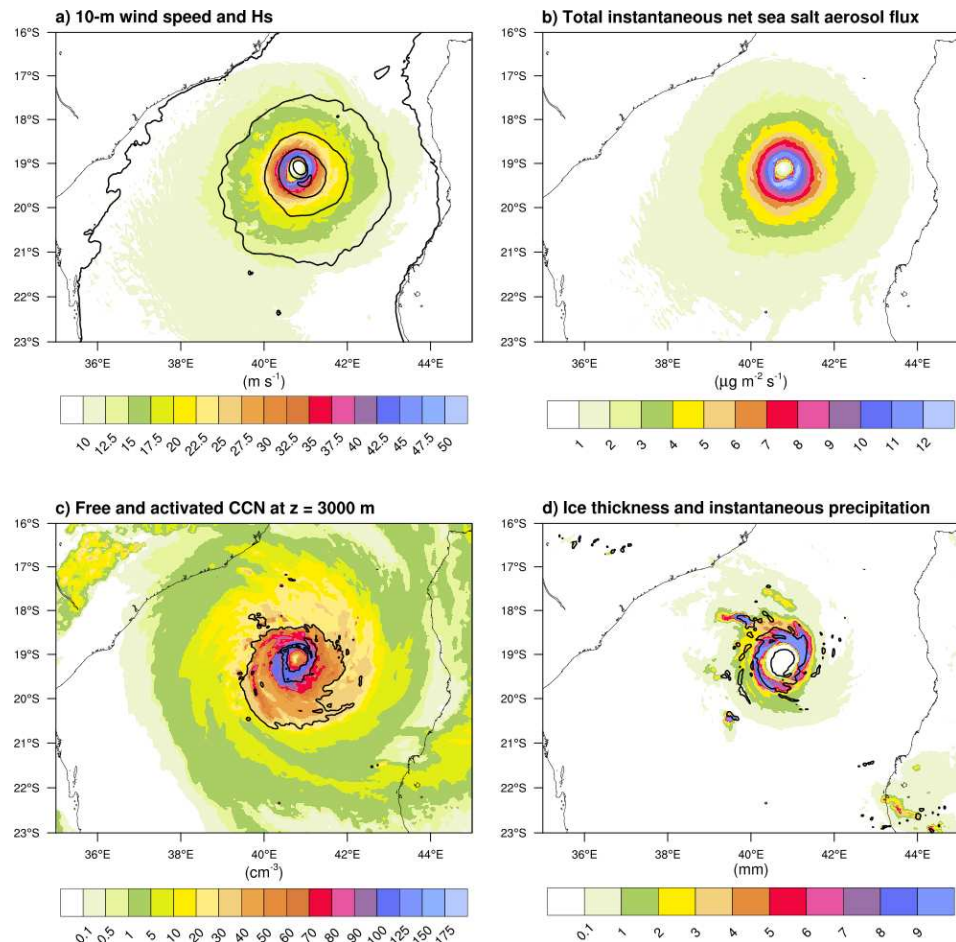


Figure 5. Horizontal cross sections of Idai on 12 March 2019 at 18 UTC, simulated with the Meso-NH/WW3/CROCO OWA coupled system. (a) 10-m wind speed (m s^{-1} ; colors) and significant wave height H_s (2, 4, 6, 8 and 10 m isolines), (b) total instantaneous net sea salt aerosol flux ($\mu\text{g m}^{-2} \text{s}^{-1}$), (c) available (colors) and activated (1 and 10 cm^{-3} isolines) CCN, and (d) total ice thickness (mm; colors) and instantaneous precipitation (10 mm h^{-1} isoline). In c) only the contribution of sea salt particles (with dry diameter higher than 80 nm) to CCN is shown.

As shown in Bousquet et al. [15], one important achievement of RNR-CYC lied in the collection of numerous space-borne synthetic aperture radar (SAR) observations within TC developing in the SWIO. As shown in the following, such data can be particularly useful to evaluate TC simulations made in the frame of the project but also to improve RSMC La Réunion real-time or post-event analyses of TC intensity and improve model forecast from assimilating SAR observations into high-resolution NWP systems [91]. During TC Idai, two exploitable SAR images were collected directly within the core of the storm, including one slightly before its landfall in Beira, on 14 March 2019 at 16:05 UTC. This SAR image (Figure 6a) locates the center of TC Idai 90 km to the east of Beira. The retrieved surface wind field shows wind speed values in the eyewall between 35 and 46 m s^{-1} , with a reduced region with maximum wind speed of 46 m s^{-1} in the northeastern part of the eyewall. On 14 March at 18 UTC, the minimum sea level pressure and the maximum 10-min

sustained wind speed were estimated by the best-track from RSMC La Réunion at 955 hPa and 42 m s^{-1} , respectively. Due to a faster translation speed in the simulation compared to the best-track from 13 March at 00 UTC, the simulated TC is located $\sim 80 \text{ km}$ offshore the Mozambique coast on 4 March around 14 UTC. The modeled system is $\sim 6 \text{ h}$ in advance and lands slightly too south ($\sim 20 \text{ km}$) compared to the observations (Figure 5a). The OWA simulation at 13 UTC produces higher wind speed in the eyewall ($>46 \text{ m s}^{-1}$, with a maximum of 60 m s^{-1} ; Figure 6b) than the SAR retrieval at 16 UTC. However, the 34 m s^{-1} wind extension is similar in the simulation and the SAR retrieval (90–100 km). Despite a landing in Mozambique a few hours in advance and with a slightly overestimated intensity, the OWA system is able to reproduce the overall evolution of TC Idai during this 4 day simulation. However, the model was not able to capture the eyewall replacement cycle. This deficiency will be investigated, in particular the potential impact of the microphysics parameterization on the eyewall replacement cycle development [92,93].

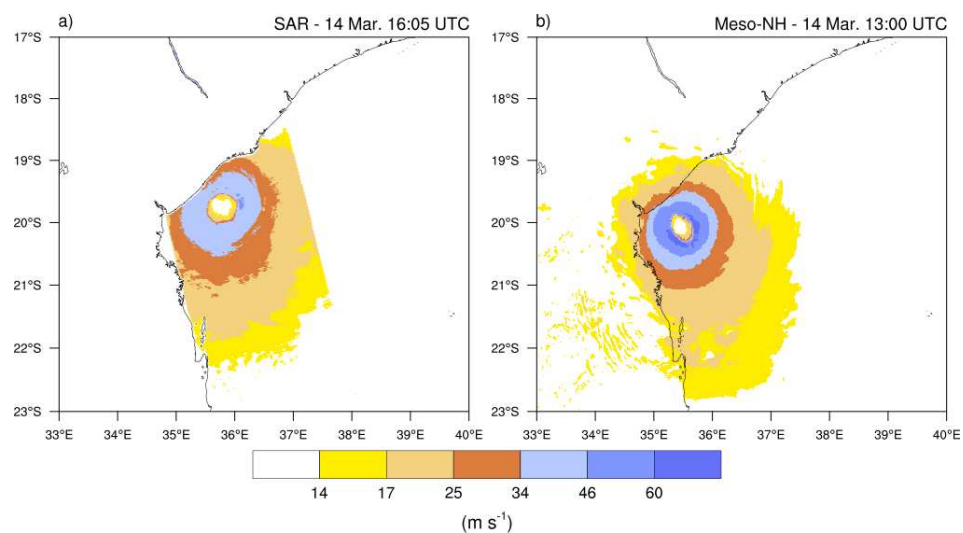


Figure 6. Horizontal cross sections of TC Idai on 14 March 2019: (a) SAR surface wind speed (m s^{-1}) at 16:05 UTC, (b) 10-m wind speed (m s^{-1} ; colors) at 14:00 UTC simulated with the OWA coupled system.

3.5. Tropical Cyclone Herold (2020)

3.5.1. Storm Description and Model Simulations

The intense tropical cyclone Herold (2020) initiated as a tropical depression located north-east of Madagascar on 12–13 March 2020. This system, the second most intense storm of the 2019–2020 TC season in the SWIO basin, initially moved towards Madagascar while slowly intensifying before stopping off-shore the coast on 14 March, where it remained stationary for about 24 h (Figure 7). It then turned around to head south-east and underwent a rapid intensification to reach ITC stage in the morning of 17 March, with 10-min averaged sustained winds of $\sim 46 \text{ m s}^{-1}$ and wind gusts of up to 64 m s^{-1} . The intensification phase of TC Herold was sampled by one of the two space-borne SAR deployed onboard ESA’s Sentinel-1 satellites and two of the sea turtles deployed in RNR-CYC (see Part 1, [15]). Although it did not impact inhabited territories, TC Herold is thus a particularly interesting case to evaluate the potential of the novel observations deployed in this project.

TC Herold was simulated for 126 h with the OA coupled system AROME/NEMO from 13 March 2020 at 12 UTC. This coupled model, which prefigures the future operational NWP system that will soon be used by RSMC La Réunion for TC forecasting in the SWIO, was run for four periods of 48 h, respectively initialized on March 13 (HR1), 14 (HR2), 15 (HR3), and 16 (HR4) at 12 UTC, with ocean cycling every 24 h (i.e., runs HR2/3/4 start from the ocean state of the 24 h forecast of the previous coupled run). For HR1, NEMO was initialized from Mercator-Ocean operational model (also known as Glo12), which also provided lateral boundary conditions every day. AROME was initialized from ECMWF’s

IFS operational NWP system, which also provided lateral boundary conditions every 6 h. In order to reduce the model spin up and be able to already produce small scale features at initiation time T_0 in the model, ECMWF large-scale atmospheric fields (temperature, wind, humidity, and surface pressure) valid at T_0 were combined with a 6-h AROME forecast initialized at $T_0 - 6$ h [94].

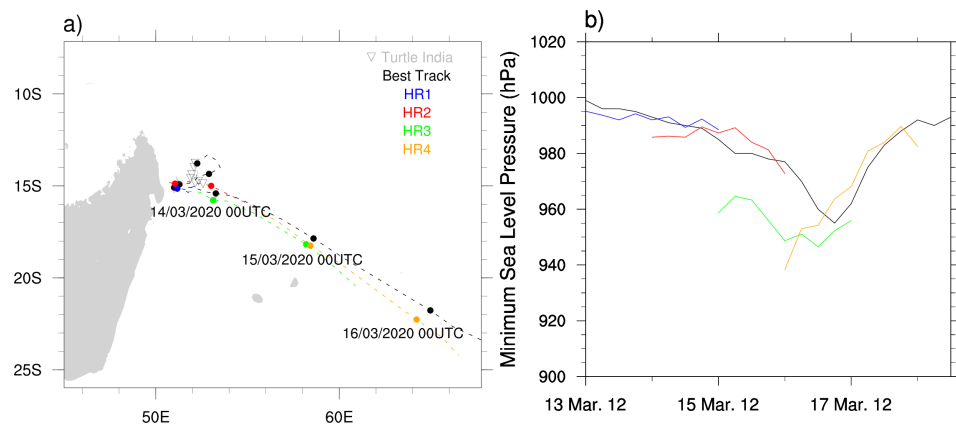


Figure 7. (a) Track and (b) intensity defined by the MSLP (hPa) of TC Herold. The best-track and the AROME/NEMO simulations are shown as black and color lines, respectively. The positions of ST India are displayed as grey triangles.

3.5.2. TC Track and Intensity Forecasts

Figure 7 shows the track and intensity (MSLP) of TC Herold as analyzed in RSMC La Réunion best-track and simulated by AROME/NEMO between 13 and 18 March 2020. Runs HR1 (blue line) and HR2 (red line) show good agreement with best-track data both in terms of trajectory and intensity, meaning that the coupled model was able to correctly reproduce the cyclogenesis of the system. For run HR3 (green line), the storm intensity simulated by AROME/NEMO is however significantly overestimated following an overestimation of the MSLP of ~ 25 hPa at initialization time. The mean rate of intensification over time is nevertheless relatively consistent with that observed in the best-track (~ 25 hPa in 36 h), as is the time when the system reached its maximum intensity (947 hPa on 17 March at 00 UTC vs. 955 hPa on 17 March at 06 UTC). For the last run (HR4, yellow line), the intensity at initialization time is even more erroneous, with an error in initial MSLP of nearly -35 hPa with respect to best-track data. This strong initial bias is nevertheless quickly cancelled, with modeled intensities beginning to precisely match best-track data after 18 h of simulation. The initial positions of the storm in the two latter runs are also slightly shifted southwards (~ 20 km) with respect to best-track data with positioning errors slightly increasing over time to reach ~ 80 km at the end of the simulations. Despite these errors, the simulation of TC Herold by AROME/NEMO can be considered as satisfactory. Hence, the coupled model is shown to simulate the cyclogenesis and the first smooth intensification phase of the TC with little discrepancies (runs HR1 and HR2). Despite a significant overestimation of the initial TC intensity in runs HR3 and HR4, the model is also able to gradually adjust itself to eventually match reference measurements.

As mentioned previously, comparisons to best-track data allow for the evaluation of the performance of the model in a broad sense, but SAR data collected in RNR-CYC represent a rare opportunity to more precisely evaluate intensity and structure forecasts over the open ocean as well as to refine comparisons with RSMC La Réunion analyses. In this regard, a comparison between SAR-derived observations made in TC Herold on 16 March 2020 at 02 UTC, i.e., more or less when the storm reached TC intensity (33 m s^{-1}), and simulated surface winds at the same time are shown in Figure 8.

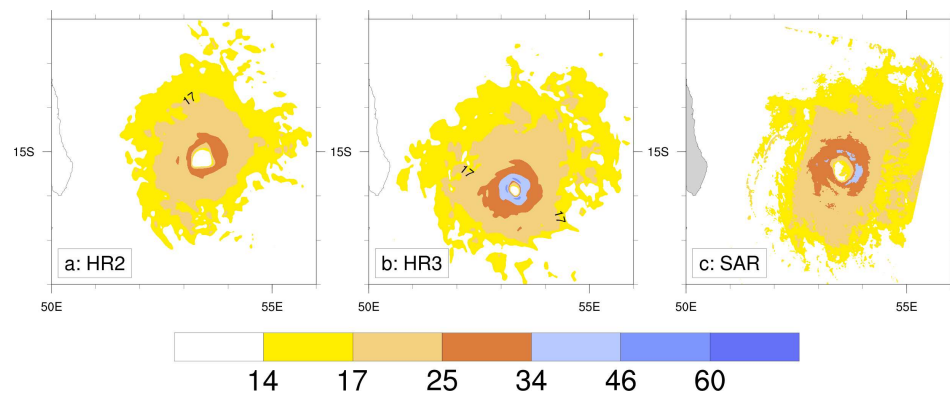


Figure 8. 10-m wind field (m s^{-1}) below TC Herold on 16 March 2020 at 02 UTC, as inferred from AROME/NEMO simulations initialized on (a) 14 March at 12 UTC (HR2), (b) 15 March at 12 UTC (HR3), and (c) surface wind field (m s^{-1}) inferred from SAR-derived data.

According to SAR-derived wind data (Figure 8c), the eye of the system at observation time was more or less circular with a diameter of ~ 40 km, but the eyewall was not yet well structured and was showing a weakness in the southern quadrants. The maximum intensity was observed in the eastern quadrant of the eyewall with surface wind speed of ~ 34 m s^{-1} . Corresponding 10-m surface winds inferred from model simulations HR2 (38-h forecast lead time) and HR3 (14-h forecast lead time) are shown in Figure 8a,b, respectively. In good agreement with pressure data shown in Figure 7, the structure and intensity of the TC simulated in run HR2 show good consistency with satellite data. The simulated TC eye has both proper dimension and position, and maximum simulated surface winds (~ 32 m s^{-1}) are located in the eastern quadrant of the eyewall. While the 34 m s^{-1} wind extension (brown colour, hurricane force) is slightly more compact in the simulation, the 25 m s^{-1} (beige colour, storm force) and 17 m s^{-1} (yellow colour, gale force) wind extensions both match observations very well. As expected from Figure 7, stronger discrepancies can be noticed for run HR3 (Figure 8b). Compared to SAR data, the location of the storm center is then shifted southwards by about 40–50 km and surface wind values are significantly higher, with maximum wind speed of ~ 46 m s^{-1} all the way around the eye (vs. 34 m s^{-1} in SAR data). The TC eye simulated by the model is also significantly smaller than in the SAR observations and appears completely enveloped by the eyewall, which is indicative of a more organized and intense system. Despite significantly stronger winds near the core of the system, hurricane, storm, and gale force wind extensions nevertheless match observations quite well.

Such differences in behavior between successive model runs are not uncommon but do nevertheless pose problems to TC forecasters who need relatively stable forecasts over time to make their predictions. While the comparisons with the best track data might suggest that the model run HR3 is unrealistic, the comparison with SAR-derived observations tempers this impression and shows that the overall structure of the system was actually well simulated by the AROME/NEMO modeling system.

3.5.3. Ocean Temperature Forecasts

Because Earth observing satellites cannot provide SST measurements below TCs due to their associated large cloud cover, a precise validation of ocean model temperature forecasts in cyclonic conditions necessarily requires the availability of in-situ data. As oceanic sensors such as ARGO drifters or moored buoys are sparse in the SWIO, biologging data collected by sea turtles (ST) in the frame of RNR-CYC provide a fantastic possibility to investigate potential changes in surface and subsurface ocean temperature fields under cyclonic conditions. Two of the sea turtles equipped with temperature-depth ARGOS tags released during this program have been able to collect temperature data within or in the immediate vicinity of TC Herold [15]. One animal (ST Tom) has been located a few hundreds km away from the storm for about one week (allowing to sample the overall

oceanic environment away from the TC core), and the second one (ST India) remained trapped for about 4 days (13–16 March) in the immediate vicinity of the TC core. While surface temperature data collected by ST India during this period can be used to investigate the temporal evolution of the SST field in the vicinity of TCs (see Figure 10 in [15]), vertical profiles of ocean temperature reconstructed from sea turtles observations also provide a rare opportunity to investigate the performance of coupled ocean–atmosphere models in cyclonic conditions.

Figure 9 presents comparisons between temperature profiles simulated by the AROME/NEMO coupled system and observed by ST India from 13 to 16 March at 15 UTC. In order to reconstruct ocean temperature profiles from ST-borne observations, temperature–depth measurement pairs collected every 5 min by ST India were aggregated over a period of 3 h centered on 15 UTC. NEMO temperature profiles forecasted from the three model runs encompassing this 4-day period (HR1–3) were extracted at the same time at the grid point closest to the observations. Knowing that sea turtles move at most 2 to 3 km per hour [39], one can thus consider that all sea turtles data used to reconstruct a given vertical profile are collected within the same NEMO column ($1/12^\circ$ horizontal resolution).

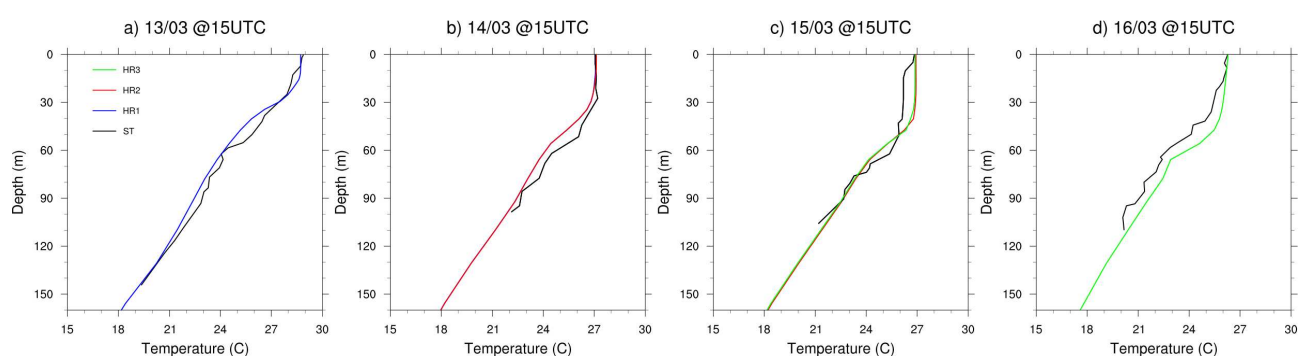


Figure 9. Vertical profiles of ocean temperature ($^\circ\text{C}$) valid at 15 UTC on (a) 13, (b) 14, (c) 15 and (d) 16 March 2020, as deduced from observations collected by ST India (black line) and from simulations HR1 (blue line), HR2 (red line) and HR3 (green line). Sea turtle data are aggregated over a 3-h period centered at 15 UTC.

As expected, the SST in the vicinity of the TC core is found to decrease significantly during the investigated 72-h intensification period of the storm. The evolution of SST, which dropped from 29°C on 13 March (Figure 9a) to 26°C on 16 March (Figure 9d), was well captured in the three model runs. On 13 (Figure 9a, run HR1, blue line) and 14 (Figure 9b, run HR2, red line) March, the observed vertical temperature profiles were also well reproduced by the coupled model, especially in the ocean mixed layer (OML, ~ 0 –50 m depth on average). The next two days, important discrepancies can however be noticed compared to ST observations. On 15 March (Figure 9c), temperatures are overestimated by $\sim 1^\circ\text{C}$ throughout the OML in both runs HR2 and HR3 (green line). As the initialization of ocean fields in simulation HR3 comes from NEMO HR2 outputs valid only 3 h before, observed similar profiles are expected, but these differences are further exacerbated 24 h later (HR3, 27-h forecast lead time). Based on these comparisons, the coupled system is able to properly simulate the surface cooling in the vicinity of the TC but does not seem able to reproduce the temperature drop in the OML during the rapid intensification period of the system. This behavior may be related to an insufficient vertical resolution of the model or to a too strong mixing. Additional simulations of TCs for which ST-borne measurements will be available should be performed to extend the evaluation of the oceanic part of the modeling platform.

4. Climate Projection of Tropical Cyclone Activity in the SWIO

It is commonly accepted that the predicted increase in TC intensity will be related to the increase in atmospheric moisture content resulting from higher SSTs [7,95–98]. However, no real consensus exists yet regarding the evolution of TC frequency and the underlying

physical processes in the context of global warming. Bengtsson et al. [99,100] and Sugi [101] hypothesized that the number of cyclogenesis in the future will mostly depend on changes in large-scale upward mass flux driven by synoptic circulation. Emanuel et al. [102] and Emanuel [103] suggested that the decrease in TC frequency could be rather related to an increase in the saturation deficit in the middle troposphere as well as temperature modulation in the upper troposphere.

Most recent studies that investigate the impact of global warming on frequency, intensity, and precipitation of tropical storms and cyclones are based on the analysis of climate simulations carried out within the framework of the 5th phase of the Coupled Model Interception Project (CMIP5). As the spatial resolution of CMIP5 experiments is generally too coarse (1° at best) to accurately capture the full life cycle of low-pressure tropical systems, such simulations are not suitable for studying the early stages of the development of TCs in a future climate [104,105]. Although the next phase of the CMIP project (also known as CMIP 6), which includes a few model runs at 50 km, will open up new perspectives on this subject, some climate centers have already begun to conduct high-resolution climate experiments (ranging from 6 to 50 km in horizontal grid spacing) to assess the evolution of cyclonic activity on a regional scale as well as to investigate potentially different trends from one cyclonic basin to another, (e.g., [10,12,13,106]). The results of these studies have mostly confirmed those obtained from CMIP5 models and pointed to a general decrease in TC frequency together with a more or less significant increase in TC intensity and, in some cases, TC-related precipitation [10].

Indeed, while regional and global climate models enable identifying the favored regions of cyclogenesis and occurrence of tropical storms and cyclones at the basin scale, a better spatial resolution and more advanced physical schemes are needed to reproduce the intensification mechanisms and the behavior of tropical systems at landfall. One of the goals of the climate component of RNR-CYC was thus to evaluate the future evolution of TC activity in the SWIO. While high-resolution simulations performed with global models are used to anticipate the global evolution of the TC activity [13], a pseudo global warming procedure is implemented in the coupled OWA model described in Section 2 to evaluate the modifications of the TC structure and impacts in a modified oceanic and atmospheric environment [67].

Cattiaux et al. [13] used high-resolution experiments performed with a rotated-stretched configuration of Météo-France Coupled Global Climate Model (CNRM-CM) to estimate projected changes in cyclonic activity over the South Indian Ocean near the end of the century. The model predicted a 20% decrease in TC frequency together with an increase of TC intensity and a slight shift of TC trajectories towards the poles, as already observed in previous studies [107,108]. In the following we use the high-resolution global climate simulations already used in Cattiaux et al. [13], and specifically made for RNR-CYC, to investigate potential changes in the frequency and intensity of TCs in the SWIO over the period 2051–2094.

4.1. Data and Methodology

4.1.1. CNRM-CM Model Data

This study is based on present-day (1971–2014, hereafter referred to as ARP-P) and future (2051–2094, ARP-F) atmosphere-only experiments performed by Cattiaux et al. [13] using the CNRM-CM climate model in its rotated-stretched configuration [6,106]. This particular configuration, routinely used by Météo-France for operational forecasting applications in Europe with ARPEGE (the atmospheric component of CNRM-CM), allows increasing horizontal resolution over a given region of interest (the pole) while progressively decreasing it towards the antipode. Here, the pole is placed at (12.5° S, 55° E) and the stretching factor is fixed to 3.5, allowing for a 14-to-30 km effective resolution over the SWIO (see Figure 1 in [13]). The SST used in the ARP-F experiment is prescribed from a member of CNRM-CM5 historical Radiative Concentration Pathway (RCP) 8.5 simulations [109] and is bias-corrected over the reference period using HadISST dataset [110]. The

reader is referred to Cattiaux et al. [13] for more information about the methodology and verification of the numerical experiments used in the following. A detailed description of the physics of the CNRM-CM model can also be found in Voldoire et al. [111].

4.1.2. Tracking Algorithms and Model Calibration

The cornerstone for investigating the evolution of TC activity from climate simulations is the capability to efficiently track low-pressure tropical systems produced by the model. In this study we use the tracker proposed by Chauvin et al. [6], which has been designed to reconstruct the full trajectories (i.e., including during the pre-cyclogenesis stage) of simulated TSs and TCs across consecutive time steps from six main criteria (sea-level pressure, 850 hPa vorticity, 10-m wind speed, mean 700–300 hPa temperature, tangential wind, local temperature anomaly). The reader is referred to Chauvin et al. [6], Daloz et al. [112], and Chauvin et al. [106] for more details about this algorithm and to Cattiaux et al. [13] for the values of the empirical thresholds used to analyze the ARP-P and ARP-F experiments.

The distributions (in frequency or intensity) of TC simulated by climate models are generally not calibrated against real data as the main objective of most studies is usually to compare between present and future climate in a relative way. Such calibration procedure can nevertheless be useful to discuss the evolution of TC activity with respect to “real world” intensity classification. This capability is, for instance, particularly important for decision-makers in order to determine the classes of systems that should be the most severely impacted by climate change (an x percent increase in storm intensity will have a different impact depending on whether it applies to a TS or to a VITC). In the following we apply such calibration to CNRM-CM simulations with the goal to refine the results previously obtained in Cattiaux et al. [13].

The calibration of model data is performed over the 44-year period of reference (1971–2014) using RSMC La Réunion best-track data. This procedure, based on a quantile-to-quantile (QQ) correction, allows one to match simulated distributions of TC frequency (number of days of cyclonic activity) and TC intensity (V_{MAX}) to RSMC La Réunion reference distributions. In order to also apply this QQ correction to ARP-F simulation, all simulated storms with $V_{MAX} > 70 \text{ m s}^{-1}$ are included in the last quantile. Results of this correction for the present-day simulation are shown in Figure 10.

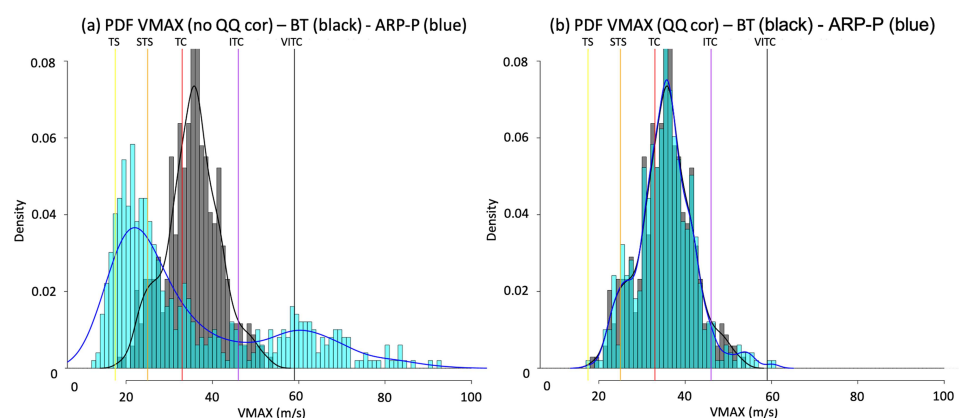


Figure 10. Probability density function (PDF) of the maximum wind speed (V_{MAX} , m s^{-1}) for cyclogenetic storms ($V_{MAX} \geq 17 \text{ m s}^{-1}$) in the SWIO, as derived from best-track (BT) (grey bars and black curve) and ARP-P simulation (cyan bars and blue curve) data (a) prior and (b) after the quantile-to-quantile (QQ) correction. Yellow, orange, red, purple, and black lines indicate TS, STS, TC, ITC, and VITC intensity threshold values, respectively. Note that V_{MAX} values less than 17 m s^{-1} correspond to the intensity of the tracked storms prior to their cyclogenesis.

Based on best-track data, the total number of CS ($V_{MAX} \geq 17 \text{ m s}^{-1}$) that developed in the SWIO over the period 1971–2014 averages ~ 9.8 systems per year (Table 3). Half of these storms will remain at the stage of MTS or STS while the other half will reach TC intensity

($V_{MAX} \geq 33 \text{ m s}^{-1}$) or higher. According to uncorrected ARP-P (present-day) simulation data, the climate model tends to underestimate the overall number of CS (7.8 vs. 9.8 in best-track data) as well as the overall proportion of storms that reach TC (14% vs. 23.5% in best-track data) and ITC (11% vs. 21.5% in best-track data) intensity. The model, however, significantly overestimates the proportion of very intense systems (19% vs. 5% in best-track data). These discrepancies can also be clearly identified in the probability density function (PDF) of the simulated maximum wind speed (Figure 10a). After the application of the QQ correction, both distributions match remarkably well (Figure 10b).

Table 3. Average annual number of CS in the SWIO over the period 1971–2014, as derived from best-track data and ARP-P simulation. Total corresponds to the total number of cyclogenetic storms. TC, ITC, and VITC correspond to the number (percentage) of storms reaching TC, ITC, and VITC intensity, respectively, according to their LMI.

		Total	TC	ITC	VITC
Number (percentage) of storms	Best-track	9.8	2.3 (23.5%)	2.1 (21.5%)	0.5 (5%)
	ARP-P	7.9	1.1 (14%)	0.9 (11%)	1.5 (19%)

4.2. Simulated Frequency and Intensity of Future TC

After applying a QQ correction to both present- and future-day simulations, one can therefore estimate potential changes in cyclonic activity between the two simulated epochs with respect to “real world” TC classifications. Figure 11a shows the PDF of the V_{MAX} for tracked CS simulated in ARP-F (blue) and ARP-P (grey) simulations, classified by storm intensity category. Through considering all intensity classes, one can note an average frequency decrease of nearly 20–25% between ARP-P and ARP-F simulations. This result is consistent with the previous global analysis of Cattiaux et al. [13] that showed a reduction of the cyclonic season length of about 1 month (20%) between the two simulated epochs. Going into the details, one can notice an overall decrease of the storm intensities for TS and TC categories between the two epochs but also a significant increase for higher intensity systems. The changes in storm frequency (days of cyclonic activity) shown in Figure 11b indicate that the largest decrease in frequency occurs for low-to-moderate intensity systems ($V_{MAX} < 42 \text{ m s}^{-1}$). On average, the number of days of cyclonic activity between the two epochs is (i) significantly reduced for TSs (MTS, STS) and lower intensity TCs (TC-, $33 < V_{MAX} < 42 \text{ m s}^{-1}$), which all together represent $\sim 75\%$ of CS developing in the basin, (ii) significantly increased for higher intensity TC (TC+) and lower intensity ITC (ITC-) systems ($42 < V_{MAX} < 50 \text{ m s}^{-1}$), and (iii) globally unchanged for the most intense storms ($V_{MAX} > 50 \text{ m s}^{-1}$).

Figure 12a also suggests that storm intensities should be subject to significant changes in the future (plain red line) with respect to present time (plain black line). Hence, one can note an overall decrease of the intensity for all TS with $V_{MAX} < 25 \text{ m s}^{-1}$, an increase for all storms with V_{MAX} between 25 m s^{-1} and 50 m s^{-1} (i.e., STS, TC, and ITC-), and almost no change for the most intense systems ($V_{MAX} > 50 \text{ m s}^{-1}$, ITC+ and VITC). Due to the small sample size for the latter categories, these numbers should however be taken cautiously. Expressing these differences as percentages for each storm category gives a decrease of up to $\sim 2 \text{ m s}^{-1}$ ($\sim 10\%$) for MTS and increases of up to $\sim 1.8 \text{ m s}^{-1}$ ($\sim 5\%$) for STS, 7.5 m s^{-1} ($\sim 20\%$) for TC, and 6 m s^{-1} ($\sim 14\%$) for ITC- ($42 < V_{MAX} < 50 \text{ m s}^{-1}$). The mean position of the storm LMI, as derived from best-track and model simulations, is also shown in Figure 12b. In the present-time simulation (blue), one can note that the mean latitude of the LMI is shifted southward by $\sim 0.5^\circ$ with respect to best-track data (white) and that the dispersion is also larger in the model. This confirms the slight tendency of CNRM-CM to slightly overestimate TC intensification in the southern part of the basin, which was already noticed by Cattiaux et al. [13]. Though comparing the mean latitudes of the LMI in ARP-P (blue) and ARP-F (grey) simulations, one can notice that the location of this maximum is shifted southwards by $\sim 1.5^\circ$ (i.e., to $\sim 22^\circ \text{ S}$) in the future (in good agreement with the previous study of Kossin et al. [107]).

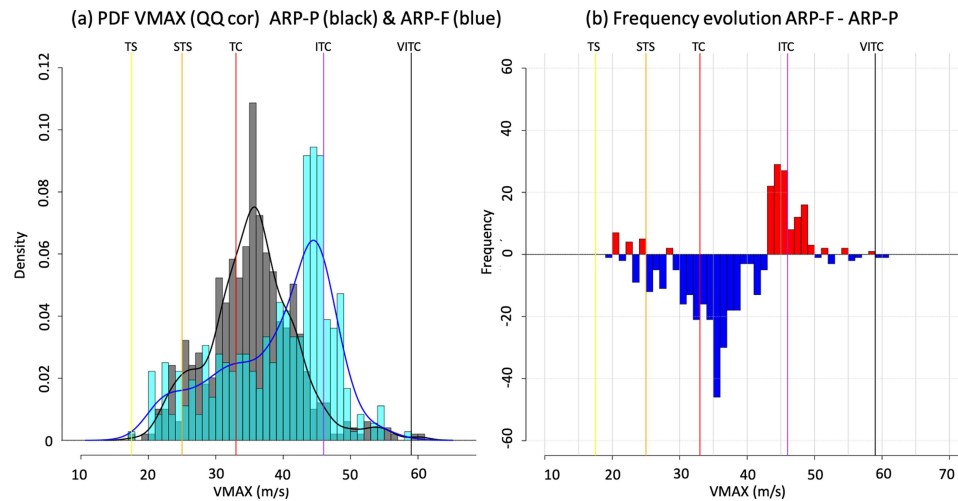


Figure 11. (a) As in Figure 10 but for corrected ARP-P (grey bars and curve) and ARP-F (blue bars and curve) simulations. (b) Evolution of the frequency (days of cyclonic activity) of CS between the two simulated epochs as a function of V_{MAX} . Yellow, orange, red, purple, and black vertical lines indicate TS, STS, TC, ITC, and VITC intensity threshold values, respectively.

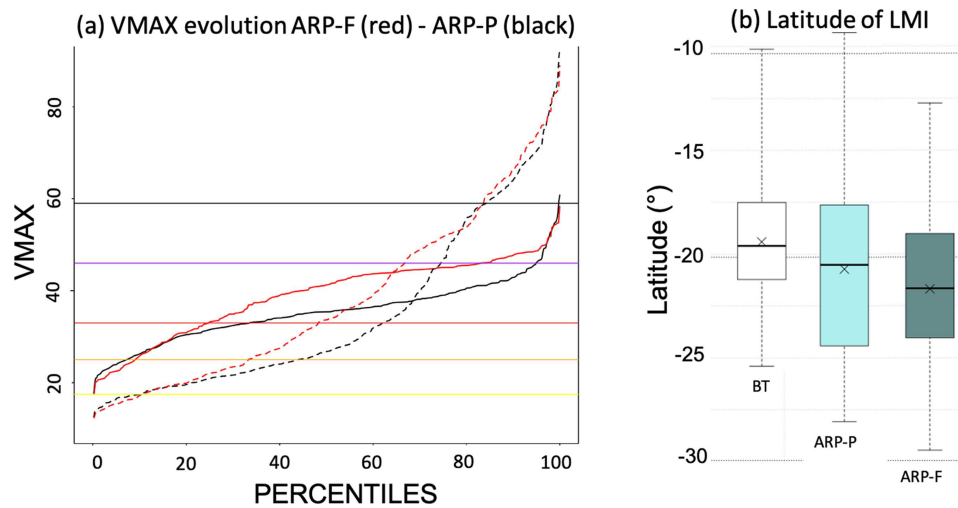


Figure 12. Mean evolution of the LMI of simulated CS ($V_{MAX} > 17 \text{ m s}^{-1}$) between the two epochs. (a) Percentile values as deduced from ARP-P (black) and ARP-F (red) simulations before (dashed) and after (plain) QQ correction. (b) Average latitude of storm LMI, as derived from best-track (white), ARP-P (blue), and ARP-F (grey) data. In (a) yellow, orange, red, purple, and black horizontal lines indicate MTS, STS, TC, ITC, and VITC intensity threshold values, respectively.

All together, these results provide unprecedented detailed projections of TC activity in the SWIO in the second half of the century and suggest that all storm categories should be impacted differently by climate change:

- MTS should be slightly more frequent, but less intense;
- STS should become less frequent, but more intense;
- Low intensity TC (TC-, $33 < V_{MAX} < 42 \text{ m s}^{-1}$) should be less frequent, but significantly more intense;
- High intensity TC and low intensity ITC (TC+ and ITC-, $42 < V_{MAX} < 50 \text{ m s}^{-1}$) should be more frequent and more intense;
- ITC+ and VITC ($V_{MAX} > 50 \text{ m s}^{-1}$) should not experience significant changes.

Because Réunion and Mauritius islands are essentially concerned by STS and TC, these results also suggest that the cyclonic activity during the second half of the century should be significantly enhanced in the Mascarene Archipelago. Thus, despite an overall decrease in frequency of these two storm categories, their increased intensity, which could reach up to 20% for TCs, combined with the migration of the storm LMI near 22° S (which more or less corresponds to the latitude of Réunion and Mauritius islands), could lead to a significant increase of TC-related hazards in these two territories. These results, only based on two simulations, are obviously to be taken with precaution and will have to be confirmed by the analysis of other high-resolution regional or global simulations. In this regard, the use of high-resolution model runs made in the frame of CMIP6 and BRIO (<https://www.commissionoceanindien.org/portfolio-items/brio/>, accessed on 27 May 2021) should allow one to further evaluate the realism of this scenario (work in progress). Future research work will also focus on the analysis of the differences in large scale environments to investigate possible relationships between the evolution of the atmospheric parameters (wind shear, moisture, vorticity...) and observed changes in TC activity.

In addition, in the frame of RNR-CYC, Thompson et al. [67] used a pseudo global warming method to estimate the projected change of a Bejisa-like TC in the second half of the century with a projected SST warming of 1.1–4.2 °C (RCP 8.5 scenario). Such a TC has the potential to be more intense (+6.5% on average), to reach its LMI 2° further poleward, and with a 33.8% increase of the median rainrate. This preliminary study enabled the building of an initialization and modeling approach that can now be used on several systems, with different climate perturbations. Such complementary km-scale resolution simulations [67] performed with the OWA coupled platform described in Section 2 should be conducted to further document the risk evolution on the inhabited islands of the basin.

5. Conclusions

The RNR-CYC programme consisted of two parts: the development of an observation network in the SWIO [15] conducted in close synergy with the implementation of numerical tools to model and analyze tropical cyclones behavior and impacts in the present and in a context of climate change. The modeling part which was the subject of this paper aimed at developing a unique coupled system to simulate TCs in the SWIO. Not only was the OWA coupling addressed but also a coherent coupling between sea state, wind field, aerosol, microphysics, and radiation was considered. Several cases of TCs that developed in the SWIO were modeled with the full scheme or part of it and evaluated against conventional or original observations like sea-turtles borne measurements [15,39]. These TCs simulations aimed at producing high resolution maps of wind, precipitation, and significant wave height to feed the three other subprograms of ReNovRisk [14]. These model outputs will be made available to the community as open access through the Geosur database development [14] (<https://geosur.univ-reunion.fr/web/>, accessed on 27 May 2021). These TCs simulations have also underlined several important results. In addition to the need for a 3D ocean–atmosphere coupling to correctly describe the intensity and the structure of ocean surface cooling in the wake of the TC [66], the significant role of sea salt aerosols (as the main source of CCN in TCs) in representing the track, intensity, and structure of TCs has been underlined [33]. The importance of coupling the ocean–atmosphere system with a wave model has also been highlighted to produce sea state coherent with the atmospheric and oceanic fields, which is crucial for sea salt aerosol emission [23] and for certain air–sea flux parameterizations. While further validation is still needed, the simulation of TC Idai presented herein perfectly illustrates the interconnections between the different models and parameterizations. It is the first attempt to simulate a TC with such a high degree of coupling, i.e., coupling between ocean, atmosphere, and wave models associated with an advanced and comprehensive coupling between aerosol, microphysics, and radiation parameterizations. Finally, the AROME/NEMO simulations of TC Herold allowed for the assessment for the first time of the performance of the future coupled TC model to be

eventually used by RSMC La Réunion in the SWIO, as well as to evaluate the added value of the observations collected during RNR-CYC to assess more precisely the performance of the oceanic and atmospheric components of this coupled system under cyclonic conditions. Sea turtle borne observations, which will soon be extended to the Mozambique Channel and north-western part of the SWIO basin, appear as a very exciting means to complement oceanic satellite observations and rare in-situ measurements available in the SWIO to evaluate ocean model forecasts within and underneath the OML.

The climate component of RNR-CYC also provided unique climate simulations to assess the evolution of TC activity in the SWIO during the second half of the 21st century and helped in implementing new approaches to accurately estimate the evolution, in terms of intensity and frequency, of the different categories of low-pressure tropical systems in this area. At both ends of the spectrum, it appears that TSs should become less frequent and slightly more intense in the future, while the most intense systems ($V_{MAX} > 50 \text{ m s}^{-1}$) should not experience significant changes. Changes, however, appear significantly more important for intermediate intensity systems such as TC and ITC ($33 \text{ m s}^{-1} < V_{MAX} < 50 \text{ m s}^{-1}$), whose intensity increase could reach up to 20% in the future. Overall, these results suggest that the Mascarene Archipelago, and in particular Réunion and Mauritius islands, should experience a significant increase of TC-related hazards in the medium term. The OWA coupled system developed in the frame of RNR-CYC can be used as a complementary tool of climate model analysis. For example, Thompson et al. [67] used this coupled system to simulate how the characteristics of TC Bejisa could change in response to global warming. This initialization and modeling procedure could be used to simulate a large series of systems for different emission scenarios to analyze the projected impact of tropical storms on the SWIO territories.

The validation of the mesoscale modeling platform will continue based on observations from RNR-CYC [15], new research programs such as the extension of the sea-turtle observing program initiated in RNR-CYC that will allow collecting in-situ ocean data throughout the entire Indian Ocean, and satellite observations, with a multiplication of simulations of TCs with different characteristics in terms of track, intensity, development region, structure, translation speed... Systematic comparisons of ocean, wave and atmosphere model outputs with available observations (e.g., analysis of the seismic noise for swell properties retrieval, temperature and salinity profiles in the upper layer of the ocean from gliders, Global Navigation Satellite System measurements for the integrated water vapor, etc.) on a large number of systems would enable one to propose an optimal configuration of the OWA platform for TC forecasting. As shown in Duong et al. [91], SAR data obtained during RNR-CYC have started being implemented in the 3D-Var assimilation scheme of AROME in its research version. Since AROME analysis can be used as initial and lateral boundary conditions for Meso-NH, improved AROME analysis would also be a benefit to the OWA coupled simulations involving Meso-NH through a better position, intensity, and structure of the vortex in the initial state.

Several improvements are already planned concerning ice microphysics and sea sprays. A key issue concerns the role of sea sprays in air–sea flux and in cloud microphysics and more particularly the sea spray emission function in extreme conditions. We will rely on Boreal unmanned airborne system flights in the environment of TC Joaninha (2019) [15]. Measurements of aerosol concentration, wind, wave height and sea state, SST, and meteorological parameters will enable a better evaluation and calibration of the sea salt aerosol flux. Moreover, new observations in ocean–atmosphere interactions in strong winds and high waves conditions will arise from the Marion Dufresne Atmospheric program (MAP-IO; <http://www.mapio.re/>, accessed on 27 May 2021) during which numerous instruments loaded onboard the Marion Dufresne vessel will collect data along its routes in the Indian and Southern oceans.

Author Contributions: Conceptualization, C.B., O.B., S.B. and P.T.; Data curation, O.B., G.B., R.C., S.C., E.C., J.D., R.H., E.L., N.M., A.M. (Alberto Mavume), D.M., A.M. (Alexis Mouche) and G.R.; Formal analysis, C.B., O.B., S.B., P.T., J.P., M.C., C.-L.T., C.T., F.B., J.C. and M.-N.B.; Funding acquisition, O.B. and P.T.; Methodology, C.B., S.B. and P.T.; Project administration, O.B.; Software, C.B., S.B., P.T., J.P., M.C., C.T., F.C., J.C. and M.-N.B.; Supervision, C.B.; Writing—original draft, C.B., O.B., S.B., P.T., J.P. and S.C.; Writing—review & editing, C.B., O.B., S.B., P.T., J.P., M.C., C.-L.T., C.T., F.B., F.C., J.C., M.-N.B., V.A., G.B., R.C., E.C., Q.-P.D., J.D., F.F.-D., R.H., E.L., S.M., N.M., A.M. (Alberto Mavume), D.M., A.M. (Alexis Mouche), N.M.R., B.R., E.R., G.R., M.S., L.Z. and J.Z. All authors have read and agreed to the published version of the manuscript.

Funding: ReNovRisk-Cyclones and Climate Change was funded by the European Union through the 2014–2020 INTERREG5 Indian Ocean program, La Réunion Regional Council, the SGAR-Réunion through the CPER programme, the University of La Réunion, and the CNRS.

Institutional Review Board Statement: All sea turtles equipped in this programme were handled by qualified and officially accredited personnel from Kelonia’s care center. The used tags meet all the requirements of the international conventions for the protection of sea turtles and were directly purchased from manufacturers specializing in marine biology and biologging.

Informed Consent Statement: Not applicable.

Data Availability Statement: The numerical models used can be downloaded at the following websites: <http://mesonh.aero.obs-mip.fr/> (accessed on 27 May 2021) for Meso-NH, <https://www.croco-ocean.org/> (accessed on 27 May 2021) for CROCO, <https://github.com/NOAA-EMC/WW3/> (accessed on 27 May 2021) for WW3, <https://verc.enes.org/oasis/download> (accessed on 27 May 2021) for OASIS3-MCT and <http://www.nemo-ocean.eu/> (accessed on 27 May 2021) for NEMO. AROME is not available in open source. Public data used in this study are available in the following repositories: <https://cyclobs.ifremer.fr/> (accessed on 27 May 2021) (S1 and RS2 SAR data); http://www.meteo.fr/temps/domtom/La_Reunion/webcmrs9.0/anglais/index.htm (accessed on 27 May 2021) (best-track data). Other data presented in this study are not publicly available due to temporary use restriction by data owners (these data, available on request from the corresponding author, will be soon deposited in the project data repository).

Acknowledgments: Numerical modeling was made possible thanks to the computer resources of Météo-France. This study contains modified Copernicus Sentinel-1 (2019-20) data. Sentinel-1 is part of the European space component of the Copernicus European program. L1 Data are free of charge and available on the Copernicus Open Access Hub (<https://scihub.copernicus.eu/>, accessed on 27 May 2021) and their specific planning and processing to tropical cyclone wind products is supported by the ESA Sentinel-1 mission ground segment team and the ESA-funded CYMS project (Contract No. 4000129822/19/I-DT).

Conflicts of Interest: The authors declare no conflict of interest.

References

1. Neumann, C. *Global Guide to Tropical Cyclone Forecasting*, WMO Trop. Cyclone Program Rep. TCP-31; World Meteorological Organization: Geneva, Switzerland, 1993; p. 43.
2. WMO. *Global Guide to Tropical Cyclone Forecasting*; WMO: Geneva, Switzerland, 2017.
3. Leroux, M.D.; Meister, J.; Mékiès, D.; Dorla, A.L.; Caroff, P. A Climatology of Southwest Indian Ocean Tropical Systems: Their Number, Tracks, Impacts, Sizes, Empirical Maximum Potential Intensity, and Intensity Changes. *J. Appl. Meteorol. Climatol.* **2018**, *57*, 1021–1041. [[CrossRef](#)]
4. Quetelard, H.; Bessemoulin, P.; Cervený, R.S.; Peterson, T.C.; Burton, A.; Boodhoo, Y. Extreme Weather: World-Record Rainfalls During Tropical Cyclone Gamede. *Bull. Am. Meteorol. Soc.* **2009**, *90*, 603–608. [[CrossRef](#)]
5. Leroux, M.D.; Wood, K.; Elsberry, R.L.; Cayan, E.O.; Hendricks, E.; Kucas, M.; Otto, P.; Rogers, R.; Sampson, B.; Yu, Z. Recent Advances in Research and Forecasting of Tropical Cyclone Track, Intensity, and Structure at Landfall. *Trop. Cyclone Res. Rev.* **2018**, *7*, 85–105. [[CrossRef](#)]
6. Chauvin, F.; Royer, J.F.; Déqué, M. Response of hurricane-type vortices to global warming as simulated by ARPEGE-Climat at high resolution. *Clim. Dyn.* **2006**, *27*, 377–399. [[CrossRef](#)]
7. Knutson, T.R.; McBride, J.L.; Chan, J.; Emanuel, K.; Holland, G.; Landsea, C.; Held, I.; Kossin, J.P.; Srivastava, A.K.; Sugi, M. Tropical cyclones and climate change. *Nat. Geosci.* **2010**, *3*, 157–163. [[CrossRef](#)]
8. Sugi, M.; Murakami, H.; Yoshimura, J. On the Mechanism of Tropical Cyclone Frequency Changes Due to Global Warming. *J. Meteorol. Soc. Jpn. Ser. II* **2012**, *90A*, 397–408. [[CrossRef](#)]

9. Christensen, J.; Krishna Kumar, K.; Aldrian, E.; An, S.I.; Cavalcanti, I.; de Castro, M.; Dong, W.; Goswami, P.; Hall, A.; Kanyanga, J.; et al. *Climate Phenomena and their Relevance for Future Regional Climate Change*; Technical Report; Cambridge University Press: Cambridge, UK, 2014. [[CrossRef](#)]
10. Knutson, T.R.; Sirutis, J.J.; Zhao, M.; Tuleya, R.E.; Bender, M.; Vecchi, G.A.; Villarini, G.; Chavas, D. Global Projections of Intense Tropical Cyclone Activity for the Late Twenty-First Century from Dynamical Downscaling of CMIP5/RCP4.5 Scenarios. *J. Clim.* **2015**, *28*, 7203–7224. [[CrossRef](#)]
11. Knutson, T.; Camargo, S.J.; Chan, J.C.L.; Emanuel, K.; Ho, C.H.; Kossin, J.; Mohapatra, M.; Satoh, M.; Sugi, M.; Walsh, K.; et al. Tropical Cyclones and Climate Change Assessment: Part II: Projected Response to Anthropogenic Warming. *Bull. Am. Meteorol. Soc.* **2020**, *101*, E303–E322. [[CrossRef](#)]
12. Walsh, K.J.E.; McBride, J.L.; Klotzbach, P.J.; Balachandran, S.; Camargo, S.J.; Holland, G.; Knutson, T.R.; Kossin, J.P.; Lee, T.C.; Sobel, A.; et al. Tropical cyclones and climate change. *WIREs Clim. Chang.* **2016**, *7*, 65–89. [[CrossRef](#)]
13. Cattiaux, J.; Chauvin, F.; Bousquet, O.; Malardel, S.; Tsai, C.L. Projected Changes in the Southern Indian Ocean Cyclone Activity Assessed from High-Resolution Experiments and CMIP5 Models. *J. Clim.* **2020**, *33*, 4975–4991. [[CrossRef](#)]
14. Tulet, P.; Aunay, B.; Barruol, G.; Barthe, C.; Belon, R.; Bielli, S.; Bonnardot, F.; Bousquet, O.; Cammas, J.P.; Cattiaux, J.; et al. ReNovRisk: A multidisciplinary programme to study the cyclonic risks in the South-West Indian Ocean. *Nat. Hazards* **2021**, *107*, 1191–1223. [[CrossRef](#)]
15. Bousquet, O.; Barruol, G.; Cordier, E.; Barthe, C.; Bielli, S.; Tulet, P.; Amelie, V.; Fletcher-Dogley, F.; Mavume, A.; Zucule, J.; et al. Impact of tropical cyclones on inhabited areas of the SWIO basin at present and future horizons. Part 1: Overview and observing component of the research program RENOVRIK-CYCLONE. *Atmosphere* **2021**, *12*, 544. [[CrossRef](#)]
16. Bender, M.A.; Ginis, I. Real-Case Simulations of Hurricane–Ocean Interaction Using A High-Resolution Coupled Model: Effects on Hurricane Intensity. *Mon. Weather Rev.* **2000**, *128*, 917–946. [[CrossRef](#)]
17. Sandery, P.A.; Brassington, G.B.; Craig, A.; Pugh, T. Impacts of Ocean–Atmosphere Coupling on Tropical Cyclone Intensity Change and Ocean Prediction in the Australian Region. *Mon. Weather Rev.* **2010**, *138*, 2074–2091. [[CrossRef](#)]
18. Lee, C.Y.; Chen, S.S. Stable Boundary Layer and Its Impact on Tropical Cyclone Structure in a Coupled Atmosphere–Ocean Model. *Mon. Weather Rev.* **2014**, *142*, 1927–1944. [[CrossRef](#)]
19. Mogensen, K.S.; Magnusson, L.; Bidlot, J.R. Tropical cyclone sensitivity to ocean coupling in the ECMWF coupled model. *J. Geophys. Res. Ocean.* **2017**, *122*, 4392–4412. [[CrossRef](#)]
20. Warner, J.C.; Armstrong, B.; He, R.; Zambon, J.B. Development of a Coupled Ocean–Atmosphere–Wave–Sediment Transport (COAWST) Modeling System. *Ocean Model.* **2010**, *35*, 230–244. [[CrossRef](#)]
21. Liu, B.; Liu, H.; Xie, L.; Guan, C.; Zhao, D. A Coupled Atmosphere–Wave–Ocean Modeling System: Simulation of the Intensity of an Idealized Tropical Cyclone. *Mon. Weather Rev.* **2011**, *139*, 132–152. [[CrossRef](#)]
22. Chen, S.S.; Zhao, W.; Donelan, M.A.; Tolman, H.L. Directional Wind–Wave Coupling in Fully Coupled Atmosphere–Wave–Ocean Models: Results from CBLAST-Hurricane. *J. Atmos. Sci.* **2013**, *70*, 3198–3215. [[CrossRef](#)]
23. Pianezze, J.; Barthe, C.; Bielli, S.; Tulet, P.; Jullien, S.; Cambon, G.; Bousquet, O.; Claeys, M.; Cordier, E. A New Coupled Ocean–Waves–Atmosphere Model Designed for Tropical Storm Studies: Example of Tropical Cyclone Bejisa (2013–2014) in the South-West Indian Ocean. *J. Adv. Model. Earth Syst.* **2018**, *10*, 801–825. [[CrossRef](#)]
24. Aijaz, S.; Ghantous, M.; Babanin, A.V.; Ginis, I.; Thomas, B.; Wake, G. Nonbreaking wave-induced mixing in upper ocean during tropical cyclones using coupled hurricane–ocean–wave modeling. *J. Geophys. Res. Ocean.* **2017**, *122*, 3939–3963. [[CrossRef](#)]
25. Andreas, E.L. The Temperature of Evaporating Sea Spray Droplets. *J. Atmos. Sci.* **1995**, *52*, 852–862. [[CrossRef](#)]
26. Andreas, E.L. Sea spray and the turbulent air–sea heat fluxes. *J. Geophys. Res. Ocean.* **1992**, *97*, 11429–11441. [[CrossRef](#)]
27. Wang, Y.; Kepert, J.D.; Holland, G.J. The Effect of Sea Spray Evaporation on Tropical Cyclone Boundary Layer Structure and Intensity. *Mon. Weather Rev.* **2001**, *129*, 2481–2500. [[CrossRef](#)]
28. Bao, J.W.; Fairall, C.W.; Michelson, S.A.; Bianco, L. Parameterizations of Sea-Spray Impact on the Air–Sea Momentum and Heat Fluxes. *Mon. Weather Rev.* **2011**, *139*, 3781–3797. [[CrossRef](#)]
29. Emanuel, K. 100 Years of Progress in Tropical Cyclone Research. *Meteorol. Monogr.* **2018**, *59*, 15.1–15.68. [[CrossRef](#)]
30. Andreae, M.; Rosenfeld, D. Aerosol–cloud–precipitation interactions. Part 1. The nature and sources of cloud-active aerosols. *Earth-Sci. Rev.* **2008**, *89*, 13–41. [[CrossRef](#)]
31. Rosenfeld, D.; Woodley, W.L.; Khain, A.; Cotton, W.R.; Carrió, G.; Ginis, I.; Golden, J.H. Aerosol Effects on Microstructure and Intensity of Tropical Cyclones. *Bull. Am. Meteorol. Soc.* **2012**, *93*, 987–1001. [[CrossRef](#)]
32. Shpund, J.; Khain, A.; Rosenfeld, D. Effects of Sea Spray on Microphysics and Intensity of Deep Convective Clouds Under Strong Winds. *J. Geophys. Res. Atmos.* **2019**, *124*, 9484–9509. [[CrossRef](#)]
33. Hoarau, T.; Barthe, C.; Tulet, P.; Claeys, M.; Pinty, J.P.; Bousquet, O.; Delanoë, J.; Vié, B. Impact of the Generation and Activation of Sea Salt Aerosols on the Evolution of Tropical Cyclone Dumile. *J. Geophys. Res. Atmos.* **2018**, *123*, 8813–8831. [[CrossRef](#)]
34. Trabling, B.C.; Bell, M.M.; Brown, B.R. Impacts of Radiation and Upper-Tropospheric Temperatures on Tropical Cyclone Structure and Intensity. *J. Atmos. Sci.* **2019**, *76*, 135–153. [[CrossRef](#)]
35. Ruppert, J.H.; Wing, A.A.; Tang, X.; Duran, E.L. The critical role of cloud-infrared radiation feedback in tropical cyclone development. *Proc. Natl. Acad. Sci. USA* **2020**, *117*, 27884–27892. [[CrossRef](#)]

36. Zadra, A.; Williams, K.; Frassoni, A.; Rixen, M.; Adames, A.F.; Berner, J.; Bouyssel, F.; Casati, B.; Christensen, H.; Ek, M.B.; et al. Systematic Errors in Weather and Climate Models: Nature, Origins, and Ways Forward. *Bull. Am. Meteorol. Soc.* **2018**, *99*, ES67–ES70. [[CrossRef](#)]
37. Lac, C.; Chaboureaud, J.P.; Masson, V.; Pinty, J.P.; Tulet, P.; Escobar, J.; Leriche, M.; Barthe, C.; Aouizerats, B.; Augros, C.; et al. Overview of the Meso-NH model version 5.4 and its applications. *Geosci. Model Dev.* **2018**, *11*, 1929–1969. [[CrossRef](#)]
38. Seity, Y.; Brousseau, P.; Malardel, S.; Hello, G.; Bénard, P.; Bouttier, F.; Lac, C.; Masson, V. The AROME-France Convective-Scale Operational Model. *Mon. Weather Rev.* **2011**, *139*, 976–991. [[CrossRef](#)]
39. Bousquet, O.; Dalleau, M.; Bocquet, M.; Gaspar, P.; Bielli, S.; Ciccione, S.; Remy, E.; Vidard, A. Sea Turtles for Ocean Research and Monitoring: Overview and Initial Results of the STORM Project in the Southwest Indian Ocean. *Front. Mar. Sci.* **2020**, *7*, 859. [[CrossRef](#)]
40. Radnoti, G.; Ajjaji, R.; Bubnova, R.; Caian, M.; Cordoneanu, E.; Emde, K.; Grill, J.D.; Hoffman, J.; Horanyi, A.; Issara, S.; et al. The spectral limited area model ARPEGE/ALADIN. *PWRP Rep. Ser.* **1995**, *7*, 111–117.
41. Lebeaupin Brossier, C.; Ducrocq, V.; Giordani, H. Two-way one-dimensional high-resolution air–sea coupled modelling applied to Mediterranean heavy rain events. *Q. J. R. Meteorol. Soc.* **2009**, *135*, 187–204. [[CrossRef](#)]
42. Bloom, S.C.; Takacs, L.L.; da Silva, A.M.; Ledvina, D. Data Assimilation Using Incremental Analysis Updates. *Mon. Weather Rev.* **1996**, *124*, 1256–1271. [[CrossRef](#)]
43. Masson, V.; Le Moigne, P.; Martin, E.; Faroux, S.; Alias, A.; Alkama, R.; Belamari, S.; Barbu, A.; Boone, A.; Bouyssel, F.; et al. The SURFEXv7.2 land and ocean surface platform for coupled or offline simulation of earth surface variables and fluxes. *Geosci. Model Dev.* **2013**, *6*, 929–960. [[CrossRef](#)]
44. Noilhan, J.; Planton, S. A Simple Parameterization of Land Surface Processes for Meteorological Models. *Mon. Wea. Rev.* **1989**, *117*, 536–549. [[CrossRef](#)]
45. Masson, V. A Physically-Based Scheme For The Urban Energy Budget in Atmospheric Models. *Bound.-Layer Meteorol.* **2000**, *94*, 357–397. [[CrossRef](#)]
46. Mironov, D.; Heise, E.; Kourzeneva, E.; Ritter, B.; Schneider, N.; Terzhevik, A. Implementation of the lake parameterisation scheme FLake into the numerical weather prediction model COSMO. *Boreal Environ. Res.* **2010**, *15*, 218–230.
47. Fairall, C.W.; Bradley, E.F.; Hare, J.E.; Grachev, A.A.; Edson, J.B. Bulk Parameterization of Air–Sea Fluxes: Updates and Verification for the COARE Algorithm. *J. Clim.* **2003**, *16*, 571–591. [[CrossRef](#)]
48. Belamari, S. Report on uncertainty estimates of an optimal bulk formulation for surface turbulent fluxes. *Marine Environment and Security for the European Area—Integrated Project (MERSEA IP) Deliverable D.4.1.2*; 2005.
49. Gaspar, P.; Grégoris, Y.; Lefevre, J.M. A simple eddy kinetic energy model for simulations of the oceanic vertical mixing: Tests at station Papa and long-term upper ocean study site. *J. Geophys. Res. Ocean.* **1990**, *95*, 16179–16193. [[CrossRef](#)]
50. Voldoire, A.; Decharme, B.; Pianezze, J.; Lebeaupin Brossier, C.; Sevaut, F.; Seyfried, L.; Garnier, V.; Bielli, S.; Valcke, S.; Alias, A.; et al. SURFEX v8.0 interface with OASIS3-MCT to couple atmosphere with hydrology, ocean, waves and sea-ice models, from coastal to global scales. *Geosci. Model Dev.* **2017**, *10*, 4207–4227. [[CrossRef](#)]
51. Madec, G.; Bourdallé-Badie, R.; Chanut, J.; Emanuela Clementi, E.; Coward, A.; Ethé, C.; Iovino, D.; Lea, D.; Lévy, C.; Lovato, T.; et al. NEMO Ocean Engine. 2019. Available online: <https://zenodo.org/record/3878122#.YLBaZaERWUk> (accessed on 27 May 2021). [[CrossRef](#)]
52. Shchepetkin, A.F.; McWilliams, J.C. The regional oceanic modeling system (ROMS): A split-explicit, free-surface, topography-following-coordinate oceanic model. *Ocean Model.* **2005**, *9*, 347–404. [[CrossRef](#)]
53. Debreu, L.; Marchesiello, P.; Penven, P.; Cambon, G. Two-way nesting in split-explicit ocean models: Algorithms, implementation and validation. *Ocean Model.* **2012**, *49–50*, 1–21. [[CrossRef](#)]
54. Klein, P.; Hua, B.L.; Lapeyre, G.; Capet, X.; Gentil, S.L.; Sasaki, H. Upper Ocean Turbulence from High-Resolution 3D Simulations. *J. Phys. Oceanogr.* **2008**, *38*, 1748–1763. [[CrossRef](#)]
55. Tolman, H.L.; Chalikov, D. Source Terms in a Third-Generation Wind Wave Model. *J. Phys. Oceanogr.* **1996**, *26*, 2497–2518. [[CrossRef](#)]
56. Craig, A.; Valcke, S.; Coquart, L. Development and performance of a new version of the OASIS coupler, OASIS3-MCT_3.0. *Geosci. Model Dev.* **2017**, *10*, 3297–3308. [[CrossRef](#)]
57. Couvelard, X.; Lemarié, F.; Samson, G.; Redelsperger, J.L.; Ardhuin, F.; Benshila, R.; Madec, G. Development of a two-way-coupled ocean–wave model: Assessment on a global NEMO(v3.6)–WW3(v6.02) coupled configuration. *Geosci. Model Dev.* **2020**, *13*, 3067–3090. [[CrossRef](#)]
58. Ovadnevaite, J.; Manders, A.; de Leeuw, G.; Ceburnis, D.; Monahan, C.; Partanen, A.I.; Korhonen, H.; O’Dowd, C.D. A sea spray aerosol flux parameterization encapsulating wave state. *Atmos. Chem. Phys.* **2014**, *14*, 1837–1852. [[CrossRef](#)]
59. Tulet, P.; Crassier, V.; Cousin, F.; Suhre, K.; Rosset, R. ORILAM, a three-moment lognormal aerosol scheme for mesoscale atmospheric model: Online coupling into the Meso-NH-C model and validation on the Escompte campaign. *J. Geophys. Res. Atmos.* **2005**, *110*. [[CrossRef](#)]
60. Tulet, P.; Crahan-Kaku, K.; Leriche, M.; Aouizerats, B.; Crumeyrolle, S. Mixing of dust aerosols into a mesoscale convective system: Generation, filtering and possible feedbacks on ice anvils. *Atmos. Res.* **2010**, *96*, 302–314. [[CrossRef](#)]
61. Vié, B.; Pinty, J.P.; Berthet, S.; Leriche, M. LIMA (v1.0): A quasi two-moment microphysical scheme driven by a multimodal population of cloud condensation and break ice freezing nuclei. *Geosci. Model Dev.* **2016**, *9*, 567–586. [[CrossRef](#)]

62. Chen, J.P.; Lamb, D. The Theoretical Basis for the Parameterization of Ice Crystal Habits: Growth by Vapor Deposition. *J. Atmos. Sci.* **1994**, *51*, 1206–1222. [[CrossRef](#)]
63. Bailey, M.P.; Hallett, J. A Comprehensive Habit Diagram for Atmospheric Ice Crystals: Confirmation from the Laboratory, AIRS II, and Other Field Studies. *J. Atmos. Sci.* **2009**, *66*, 2888–2899. [[CrossRef](#)]
64. Sauvage, C.; Lebeaupin Brossier, C.; Bouin, M.N.; Ducrocq, V. Characterization of the air–sea exchange mechanisms during a Mediterranean heavy precipitation event using realistic sea state modelling. *Atmos. Chem. Phys.* **2020**, *20*, 1675–1699. [[CrossRef](#)]
65. Pinty, J.P.; Jabouille, P. A mixed-phase cloud parameterization for use in mesoscale non hydrostatic model: Simulations of a squall line and of orographic precipitations. In Proceedings of the the Conference on Cloud Physics, Everett, WA, USA, 17–21 August 1998; pp. 217–220.
66. Bielli, S.; Barthe, C.; Bousquet, O.; Tulet, P.; Pianezze, J. The effect of atmosphere–ocean coupling on the structure and intensity of tropical cyclone Bejisa observed in the southwest Indian ocean. *Atmosphere* **2021**, submitted.
67. Thompson, C.; Barthe, C.; Bielli, S.; Tulet, P.; Pianezze, J. Projected Characteristic Changes of a Typical Tropical Cyclone under Climate Change in the South West Indian Ocean. *Atmosphere* **2021**, *12*, 232. [[CrossRef](#)]
68. Cuxart, J.; Bougeault, P.; Redelsperger, J.L. A turbulence scheme allowing for mesoscale and large-eddy simulations. *Q. J. R. Meteorol. Soc.* **2000**, *126*, 1–30. [[CrossRef](#)]
69. Bougeault, P.; Lacarrere, P. Parameterization of Orography-Induced Turbulence in a Mesobeta–Scale Model. *Mon. Weather Rev.* **1989**, *117*, 1872–1890. [[CrossRef](#)]
70. Bechtold, P.; Bazile, E.; Guichard, F.; Mascart, P.; Richard, E. A mass-flux convection scheme for regional and global models. *Q. J. R. Meteorol. Soc.* **2001**, *127*, 869–886. [[CrossRef](#)]
71. Gregory, D.; Morcrette, J.J.; Jakob, C.; Beljaars, A.C.M.; Stockdale, T. Revision of convection, radiation and cloud schemes in the ECMWF integrated forecasting system. *Q. J. R. Meteorol. Soc.* **2000**, *126*, 1685–1710. [[CrossRef](#)]
72. Mlawer, E.J.; Taubman, S.J.; Brown, P.D.; Iacono, M.J.; Clough, S.A. Radiative transfer for inhomogeneous atmospheres: RRTM, a validated correlated-k model for the longwave. *J. Geophys. Res. Atmos.* **1997**, *102*, 16663–16682. [[CrossRef](#)]
73. Inness, A.; Ades, M.; Agustí-Panareda, A.; Barré, J.; Benedictow, A.; Blechschmidt, A.M.; Dominguez, J.J.; Engelen, R.; Eskes, H.; Flemming, J.; et al. The CAMS reanalysis of atmospheric composition. *Atmos. Chem. Phys.* **2019**, *19*, 3515–3556. [[CrossRef](#)]
74. Moon, I.J.; Ginis, I.; Hara, T.; Thomas, B. A Physics-Based Parameterization of Air–Sea Momentum Flux at High Wind Speeds and Its Impact on Hurricane Intensity Predictions. *Mon. Weather Rev.* **2007**, *135*, 2869–2878. [[CrossRef](#)]
75. Andreas, E.L.; Mahrt, L.; Vickers, D. An improved bulk air–sea surface flux algorithm, including spray-mediated transfer. *Q. J. R. Meteorol. Soc.* **2015**, *141*, 642–654. [[CrossRef](#)]
76. Tolman, H.L. Alleviating the Garden Sprinkler Effect in wind wave models. *Ocean Model.* **2002**, *4*, 269–289. [[CrossRef](#)]
77. Ardhuin, F.; Rogers, E.; Babanin, A.V.; Filipot, J.F.; Magne, R.; Roland, A.; van der Westhuysen, A.; Queffelec, P.; Lefevre, J.M.; Aouf, L.; et al. Semiempirical Dissipation Source Functions for Ocean Waves. Part I: Definition, Calibration, and Validation. *J. Phys. Oceanogr.* **2010**, *40*, 1917–1941. [[CrossRef](#)]
78. Hasselmann, S.; Hasselmann, K.; Allender, J.H.; Barnett, T.P. Computations and Parameterizations of the Nonlinear Energy Transfer in a Gravity-Wave Spectrum. Part II: Parameterizations of the Nonlinear Energy Transfer for Application in Wave Models. *J. Phys. Oceanogr.* **1985**, *15*, 1378–1391. [[CrossRef](#)]
79. Battjes, J.A.; Janssen, J.P.F.M. Energy Loss and Set-Up Due to Breaking of Random Waves. *Coast. Eng.* **1978**, 569–587. [[CrossRef](#)]
80. Ardhuin, F.; O’Reilly, W.C.; Herbers, T.H.C.; Jessen, P.F. Swell Transformation across the Continental Shelf. Part I: Attenuation and Directional Broadening. *J. Phys. Oceanogr.* **2003**, *33*, 1921–1939. [[CrossRef](#)]
81. Shchepetkin, A.F.; McWilliams, J.C. Quasi-Monotone Advection Schemes Based on Explicit Locally Adaptive Dissipation. *Mon. Weather Rev.* **1998**, *126*, 1541–1580. [[CrossRef](#)]
82. Large, W.G.; McWilliams, J.C.; Doney, S.C. Oceanic vertical mixing: A review and a model with a nonlocal boundary layer parameterization. *Rev. Geophys.* **1994**, *32*, 363–403. [[CrossRef](#)]
83. Madec, G.; Delécluse, P.; Imbard, M.; Lévy, C. OPA 8.1 Ocean General Circulation Model reference manual. *Note Pole Modélisation* **1998**, *11*, 91.
84. Lellouche, J.M.; Greiner, E.; Le Galloudec, O.; Garric, G.; Regnier, C.; Drevillon, M.; Benkiran, M.; Testut, C.E.; Bourdalle-Badie, R.; Gasparin, F.; et al. Recent updates to the Copernicus Marine Service global ocean monitoring and forecasting real-time 1/12°F high-resolution system. *Ocean Sci.* **2018**, *14*, 1093–1126. [[CrossRef](#)]
85. Fairall, C.W.; Bradley, E.F.; Rogers, D.P.; Edson, J.B.; Young, G.S. Bulk parameterization of air–sea fluxes for Tropical Ocean–Global Atmosphere Coupled–Ocean Atmosphere Response Experiment. *J. Geophys. Res. Ocean.* **1996**, *101*, 3747–3764. [[CrossRef](#)]
86. Webster, P.J.; Lukas, R. TOGA COARE: The Coupled Ocean–Atmosphere Response Experiment. *Bull. Am. Meteorol. Soc.* **1992**, *73*, 1377–1416. [[CrossRef](#)]
87. Oost, W.; Komen, G.; Jacobs, C.; Van Oort, C. New evidence for a relation between wind stress and wave age from measurements during ASGAMAGE. *Bound.-Layer Meteorol.* **2002**, *103*, 409–438. [[CrossRef](#)]
88. Powell, M.D.; Vickery, P.J.; Reinhold, T.A. Reduced drag coefficient for high wind speeds in tropical cyclones. *Nature* **2003**, *422*, 279–283. [[CrossRef](#)]
89. Green, B.W.; Zhang, F. Impacts of Air–Sea Flux Parameterizations on the Intensity and Structure of Tropical Cyclones. *Mon. Weather Rev.* **2013**, *141*, 2308–2324. [[CrossRef](#)]
90. Veron, F. Ocean Spray. *Annu. Rev. Fluid Mech.* **2015**, *47*, 507–538. [[CrossRef](#)]

91. Duong, Q.P.; Langlade, S.; Payan, C.; Husson, R.; Mouche, A.; Malardel, S. C-band SAR Winds for Tropical Cyclone monitoring and forecast in the South-West Indian Ocean. *Atmosphere* **2021**, *12*, 576. [[CrossRef](#)]
92. Willoughby, H.E.; Jin, H.L.; Lord, S.J.; Piotrowicz, J.M. Hurricane Structure and Evolution as Simulated by an Axisymmetric, Nonhydrostatic Numerical Model. *J. Atmos. Sci.* **1984**, *41*, 1169–1186. [[CrossRef](#)]
93. Zhu, S.; Guo, X.; Lu, G.; Guo, L. Ice Crystal Habits and Growth Processes in Stratiform Clouds with Embedded Convection Examined through Aircraft Observation in Northern China. *J. Atmos. Sci.* **2015**, *72*, 2011–2032. [[CrossRef](#)]
94. Bousquet, O.; Barbary, D.; Bielli, S.; Kebir, S.; Raynaud, L.; Malardel, S.; Faure, G. An evaluation of tropical cyclone forecast in the Southwest Indian Ocean basin with AROME-Indian Ocean convection-permitting numerical weather predicting system. *Atmos. Sci. Lett.* **2020**, *21*, e950. [[CrossRef](#)]
95. Trenberth, K.E.; Fasullo, J.; Smith, L. Trends and variability in column-integrated atmospheric water vapor. *Clim. Dyn.* **2005**, *24*, 741–758. [[CrossRef](#)]
96. Trenberth, K.E.; Smith, L.; Qian, T.; Dai, A.; Fasullo, J. Estimates of the Global Water Budget and Its Annual Cycle Using Observational and Model Data. *J. Hydrometeorol.* **2007**, *8*, 758–769. [[CrossRef](#)]
97. Allan, R.P.; Soden, B.J. Atmospheric Warming and the Amplification of Precipitation Extremes. *Science* **2008**, *321*, 1481–1484. [[CrossRef](#)]
98. Chou, C.; Neelin, J.D.; Chen, C.A.; Tu, J.Y. Evaluating the “Rich-Get-Richer” Mechanism in Tropical Precipitation Change under Global Warming. *J. Clim.* **2009**, *22*, 1982–2005. [[CrossRef](#)]
99. Bengtsson, L.; Botzet, M.; Esch, M. Will greenhouse gas-induced warming over the next 50 years lead to higher frequency and greater intensity of hurricanes? *Tellus A* **1996**, *48*, 57–73. [[CrossRef](#)]
100. Bengtsson, L.; Hodges, K.I.; Esch, M.; Keenlyside, N.; Kornblueh, L.; Luo, J.J.; Yamagata, T. How may tropical cyclones change in a warmer climate? *Tellus A* **2007**, *59*, 539–561. [[CrossRef](#)]
101. Sugi, M. Toward Improved Projection of the Future Tropical Cyclone Changes. In *Indian Ocean Tropical Cyclones and Climate Change*; Charabi, Y., Ed.; Springer: Dordrecht, The Netherlands, 2010; pp. 29–35. [[CrossRef](#)]
102. Emanuel, K.; Sundararajan, R.; Williams, J. Hurricanes and Global Warming: Results from Downscaling IPCC AR4 Simulations. *Bull. Am. Meteorol. Soc.* **2008**, *89*, 347–368. [[CrossRef](#)]
103. Emanuel, K. Tropical Cyclone Activity Downscaled from NOAA-CIRES Reanalysis, 1908–1958. *J. Adv. Model. Earth Syst.* **2010**, *2*. [[CrossRef](#)]
104. Taylor, K.E.; Stouffer, R.J.; Meehl, G.A. An Overview of CMIP5 and the Experiment Design. *Bull. Am. Meteorol. Soc.* **2012**, *93*, 485–498. [[CrossRef](#)]
105. Camargo, S.J.; Tippett, M.K.; Sobel, A.H.; Vecchi, G.A.; Zhao, M. Testing the Performance of Tropical Cyclone Genesis Indices in Future Climates Using the HiRAM Model. *J. Clim.* **2014**, *27*, 9171–9196. [[CrossRef](#)]
106. Chauvin, F.; Pilon, R.; Palany, P.; Belmadani, A. Future changes in Atlantic hurricanes with the rotated-stretched ARPEGE-Climat at very high resolution. *Clim. Dyn.* **2020**, *54*, 947–972. [[CrossRef](#)]
107. Kossin, J.P.; Emanuel, K.A.; Vecchi, G.A. The poleward migration of the location of tropical cyclone maximum intensity. *Nature* **2014**, *509*, 349–352. [[CrossRef](#)]
108. Holland, G.; Bruyère, C.L. Recent intense hurricane response to global climate change. *Clim. Dyn.* **2014**, *42*, 617–627. [[CrossRef](#)]
109. Voldoire, A.; Sanchez-Gomez, E.; Salas y Méliá, D.; Decharme, B.; Cassou, C.; Sénési, S.; Valcke, S.; Beau, I.; Alias, A.; Chevallier, M.; et al. The CNRM-CM5.1 global climate model: Description and basic evaluation. *Clim. Dyn.* **2013**, *40*, 2091–2121. [[CrossRef](#)]
110. Rayner, N.A.; Parker, D.E.; Horton, E.B.; Folland, C.K.; Alexander, L.V.; Rowell, D.P.; Kent, E.C.; Kaplan, A. Global analyses of sea surface temperature, sea ice, and night marine air temperature since the late nineteenth century. *J. Geophys. Res. Atmos.* **2003**, *108*. [[CrossRef](#)]
111. Voldoire, A.; Saint-Martin, D.; Sénési, S.; Decharme, B.; Alias, A.; Chevallier, M.; Colin, J.; Guérémy, J.F.; Michou, M.; Moine, M.P.; et al. Evaluation of CMIP6 DECK Experiments With CNRM-CM6-1. *J. Adv. Model. Earth Syst.* **2019**, *11*, 2177–2213. [[CrossRef](#)]
112. Daloz, A.S.; Chauvin, F.; Walsh, K.; Lavender, S.; Abbs, D.; Roux, F. The ability of general circulation models to simulate tropical cyclones and their precursors over the North Atlantic main development region. *Clim. Dyn.* **2012**, *39*, 1559–1576. [[CrossRef](#)]